ISSN 1810-648X

ACADEMY OF SCIENCES
OF MOLDOVA

PHYSICAL SOCIETY OF MOLDOVA

STATE UNIVERSITY OF MOLDOVA

Moldavian Journal of the Physical Sciences

Chisinau
2016

Volume 15
No. 1-2

Scientific journal **Moldavian Journal of the Physical Sciences** includes original scientific articles, communications and reviews concerning various problems of modern physics. The journal is published in English, its periodicity is 4 numbers a year, with circulation of 200 copies.

web: http://sfm.asm.md/moldphys/

GUIDELINES FOR AUTHORS

The "Moldavian Journal of Physical Sciences" appears quarterly and publishes in English papers referring to original scientific research in physics and related fields, including applications in electronics and technology, material engineering and device physics. A review paper for every issue is planned and short communications with hot news are encouraged.

Papers must be prefaced by a brief abstract in English up to 100 words. Single space of the rows in the manuscript is required.

Authors are invited to send two printed copies of their papers, as well as an electronic record on a $3^{1/4}$ inches diskette, or by e-mail, in English. The articles will be edited by using WORD for Windows. Chapters must be numbered by using Arabic figures, as follows:

3. Experimental results.
3.1. Results analysis.
3.2. Methods of calculus.

Formulae must be written very clearly and easy-to-read. Do not use non-explained abbreviations. Illustrations and diagrams must be realized on computer drafts (on images). All graphic and text objects must be of very good quality and easy to read. Figures included in the text are preferable.

Reference citations will be presented as follows: author's forename initial and last name, journal name, volume, page number, year (in parentheses), for example: F.A. Moldovan, S.P. Russu, Phys. Rev. Let. 85, 357, (2000). Complete title, publisher, city and year will be written for book's author's name and forename initial, for example: M. Teodorescu, Cooperation in science and technology with Eastern and European countries, Editura Tehnica, Bucuresti, vol. 1, 1992. References into the text will be made within square brackets, for example [7]; reference citation numbers must be made successively, as they appear into the text.

Manuscripts of regular papers should be limited up to 10 pages and will be signed by authors; they also must be marked "Ready to print". Reviews are limited up to 20 pages. Maximum 4 pages are admitted for short communications. One full page of the journal (size A4) contains 54 rows with 95 characters/row; font size - 12. Page set up: top, left, right – 2,5; bottom – 3,5 cm. The very manuscript which is marked "Ready to print" will be published within 6 months from sending.

The submitted papers must be reviewed, if possible, by two independent reviewers. The papers must contain original work and have not submitted for publication to any other journal. The papers which have been published previously, as well those accepted to be published in other reviews, will be not be admitted by Editorial Board; the authors have to mention this situation.

Proofs will be sent to authors for checking. Corrections must be restricted to errors since modifications to the text may be charged to the author. The publishers reserve the right to adapt the presentation of an article to conform to our style. After their publishing in our journal, the manuscripts and corresponding illustrations become the property of Editorial Board and will not be returned to the authors. The same for the papers, which have not been admitted for publication. The publishing in our journal is made free of charge.

The papers sent for publishing are considered not secret. The authors only are responsible for this in front of their own institutes or employers. Authors have to mention their complete address and telephone, fax number and e-mail.

Papers from around the world can be sent to be published to the following address:

Department of Mathematical, Physical and Technical Sciences, 5 Academy St., MD 2028 Kishinev, the Republic of Moldova, tel. (+37322) 72-71-57, 73-81-66; E-mail: vcantser@phys.asm.md, E-mail of responsible secretary: sofiadonu@yahoo.com

LUMINESCENT PROPERTIES OF ZnO POWDERS SYNTHESIZED BY THE ISOVALENT SUBSTITUTION METHOD

T. I. Goglidze, I. V. Dementiev, A. V. Coval, N. D. Nedeoglo, and D. D. Nedeoglo

Department of Physics, Moldova State University,
Mateevich str. 60, Chisinau, MD-2009 Republic of Moldova
Tel: +373 22 577586; Fax: +373 22 244248; E-mail: nedeoglo_d@yahoo.com

(Received July, 29)

Abstract

Zinc oxide powders have been prepared by the isovalent substitution method by means of high-temperature annealing of a zinc sulfide powder synthesized by a chemical method. Investigation of photoluminescence (PL) spectra in dependence on annealing temperature varied from 870 to 1050°C has made it possible to find the temperature range of 920–950°C for the most active isovalent substitution of oxygen atoms for sulfur atoms and the formation of a ZnO·S phase. X-ray diffraction analysis has revealed that the powder with crystal lattice parameters a_o = 0.3249 nm and c_o = 0.5206 nm and the ratio of c_o/a_o = 1.60, which are characteristic of zinc oxide crystals, is synthesized at the maximum annealing temperature. It has been found that the maximum of a structureless PL band in the spectrum for the ZnO powder at room temperature is localized at 500 nm. It has been supposed that the band is caused by "free electron–acceptor" radiative transitions, where the acceptor level is 0.95 eV above the valence band edge.

1. Introduction

Zinc oxide is an important functional material used in many fields of technology. It is a direct-band-gap semiconductor with a wide band gap of 3.3–3.4 eV at room temperature and solely hexagonal crystal lattice (wurtzite structure) with parameters a_o = 0.325 nm and c_o = 0.521 nm [1]. Being an optically-transparent wide-band-gap semiconductor, zinc oxide is used for the construction of highly efficient light-emitting devices operating in blue and ultraviolet (UV) spectral ranges, solar elements, transparent conducting electrodes, thin-film transistors, sensor devices, UV-filters, etc. [2–5].

One of the promising techniques for synthesizing zinc oxide is the isovalent substitution method [6,7] that allows producing the materials with new properties. Investigation of the luminescent properties of powdered zinc oxide synthesized by the isovalent substitution method from zinc sulfide is discussed in the present paper.

2. Samples and experimental technique

A zinc sulfide powder obtained by chemical deposition from a water solution of zinc salt and thiourea [8] was used as a source material. Zinc oxide was synthesized by isothermal

annealing of the zinc sulfide powder at temperatures between 850°C and 1100°C in air for 2 h. During annealing, oxygen atoms substitute for sulfur atoms to form zinc oxide [9].

The samples used for investigation of luminescent properties were 5-mm-thick powdered zinc oxide layers deposited on glass substrates. PL spectra registered at room temperature in a range of 350–700 nm were excited by laser radiation at a wavelength of 337 nm and analyzed using an MDR-23 monochromator and a FEU-51 photomultiplier. The spectra were registered using a standard system based on synchronized detection.

3. Experimental results and discussion

PL spectra for the samples synthesized at various annealing temperatures of the ZnS powder are shown in Fig. 1. For the annealing temperature of 870°C, the main maximum of the PL band is localized at 445 nm ($h\nu$ = 2.79 eV). The less-intensive PL band is localized at 465 nm ($h\nu$ = 2.67 eV). As the annealing temperature increases to 920°C, the PL spectrum is slightly shifted to long wavelengths. The band at 465 nm has the highest intensity; a new band appears in the long-wave decay of the main PL band at 540 nm ($h\nu$ = 2.30 eV). The band full width at half maximum (FWHM) decreases. A gradual increase in the annealing temperature of the initial ZnS powder to 1050°C causes a shift of the main PL band towards long wavelengths (Fig. 1, inset, Table 1).

Table 1. The PL band maximum position at various annealing temperatures of initial ZnS sample

T_{anneal}, °C	λ_{max}, nm	$h\nu_{max}$, eV
870	445	2.79
920	465	2.67
950	485	2.56
1050	500	2.48

The intensity of the PL band at 540 nm increases with increasing annealing temperature of the powder and manifests itself as an inflection in the long-wave decay of the main PL band at annealing temperatures of 950°C and 1050°C. As a result, the FWHM increases (Fig. 1); this fact is apparently attributed to increasing portion of zinc oxide in ZnS powders annealed at these temperatures.

The shift of the main PL band for the studied ZnS powders towards long

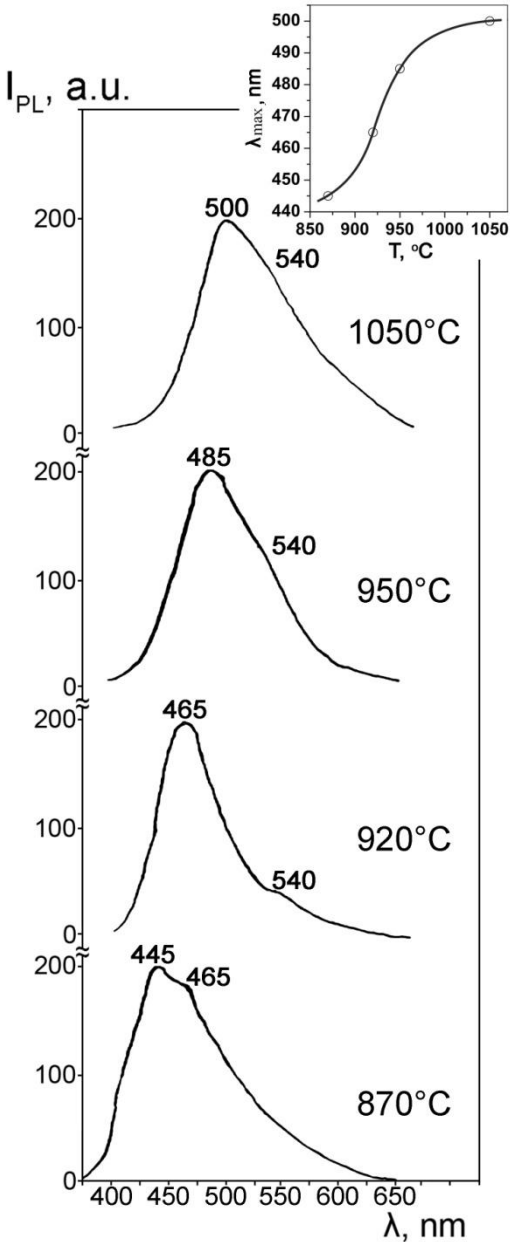

Fig.1. PL spectra of zinc sulfide powders air-annealed at various temperatures. T = 300 K, λ_{exc} = 337 nm. Inset: the PL band maximum position versus annealing temperature of the ZnS powder.

wavelengths with increasing annealing temperature is non-uniform (Fig. 1, inset, Table 2). The maximum rate of the PL band shift—0.67 nm/°C—is found for an annealing temperature range of 920–950°C. It can be assumed that the most intensive process of isovalent substitution of oxygen for sulfur atoms takes place in this temperature range. The subsequent increase in the annealing temperature from 950 to 1050°C leads to a rapid decrease in the PL band shift rate (Fig. 1, inset).

According to the authors of [10], the introduction of oxygen into ZnS leads to the formation of a ZnS·O substitutional solid solution; oxygen is present in zinc sulfide mainly as a ZnS·O solid solution and ZnO·S phase inclusions. It can be assumed that, for an annealing temperature of 1050°C, the ZnO·S phase portion almost completely determines the composition of the annealed powder, although a portion of the ZnS·O solid solution is still present. It is known that distribution of ZnO over the ZnS matrix leads to a decrease in the $ZnS{\cdot}O_S$ crystal lattice parameters because the ionic radius for oxygen (1.28 Å) is lower than that for sulfur (1.78 Å) [11]. Taking into account the parameters of the hexagonal ZnS structure a_o = 0.3826 nm and c_o = 0.6262 nm [11], a decrease in the lattice parameters of the ZnS powder air-annealed at 1050°C to a_o = 0.3249 nm and c_o = 0.5206 nm (c_o/a_o = 1.602), which were obtained from X-ray diffraction analysis using a DRON-3 diffractometer (Fig. 2), indicates the preferential formation of the ZnO·S phase in the ZnS matrix. The closeness of the obtained lattice parameters to the respective values for ZnO suggests that the synthesized powder largely represents zinc oxide, which is characterized, as it is known, by the ratio of c_o/a_o = 1.60 [11].

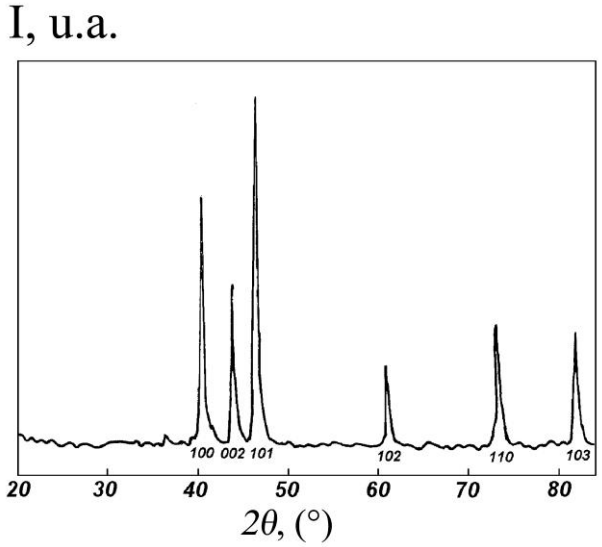

Fig. 2. X-ray diffraction pattern for the ZnS powder annealed at T_{anneal} = 1050 °C.

Table 2. The rate of temperature shift of the main PL band, $\frac{\Delta\lambda_{\max}}{\Delta T_{\text{anneal}}}$, for various annealing temperature ranges for the initial ZnS powder

Temperature range, °C	ΔT_{anneal}, °C	$\Delta\lambda_{\max}$, nm	$\frac{\Delta\lambda_{\max}}{\Delta T_{\text{anneal}}}, \frac{nm}{°C}$
870–920	50	20	0.40
920–950	30	20	0.67
950–1050	100	15	0.15

Further, during the high-temperature (1050°C) annealing of the ZnS powder in air, the PL maximum is localized at 500 nm (Fig. 1, inset), i.e., in the green spectral range, which is specific

for zinc oxide [2]. Thus, the results of X-ray diffraction analysis are in agreement with the PL data.

Despite the extensive discussions in the literature (see, for instance [2]), the nature of the green PL band localized at 500 nm in the spectra of ZnO samples is not clearly defined. In earlier papers [12, 13], the PL band in the green spectral range was attributed to copper impurity in ZnO. The specific feature of this band is the presence of a fine phonon structure. In later papers [14, 15], it was argued that V_O oxygen vacancies are responsible for the green PL band at 500 nm. However, similar to the band in Fig. 1, this band had no fine phonon structure. The authors of [16, 17] attributed the structureless green PL band in the spectra of ZnO samples to V_{Zn} zinc vacancies.

To explain the nature of the structureless band of green PL in ZnO, the following electron transitions were proposed: (1) "V_O donor–valence band" transition, where the V_O donor level was placed ~0.7 eV below the conduction band [18]; (2) "V_O donor–V_{Zn} acceptor" transition within the donor–acceptor pair model [17]; and (3) "conduction band–V_{Zn} acceptor" transition [16]. The authors of [2] note that the first two types of electron transitions are hardly probable. Taking into account the third "free-to-bond" recombination mechanism, acceptor level energy E_A can be estimated as follows:

$$E_A = E_g - h\nu_{\max} + kT,$$

where E_g is the band gap energy, k is the Boltzmann constant. E_g = 3.4 eV for ZnO at room temperature, $h\nu_{\max}$ = 2.48 eV, and $k = 8.6 \cdot 10^{-5}$ eV/K; consequently, E_A = 0.95 eV.

Evolution of PL spectra of ZnS·O with increasing annealing temperature (Fig. 1) demonstrates the formation of a ZnO·S phase in the ZnS matrix. At minimum annealing temperature (870°C), the concentration of oxygen substituting sulfur atoms is rather low and the PL maximum is localized at 445 nm (Fig. 1); this position agrees well with the position of the PL maximum for ZnS samples with a low oxygen concentration (0.3–0.4 mol %) [11]. As the annealing temperature increases, the PL spectrum of the investigated powders is shifted towards long wavelengths; this finding can be reasonably attributed to increasing oxygen concentration in the powders and the formation of a ZnO·S phase. Finally, at the maximum annealing temperature (1050°C), the PL maximum is localized at 500 nm; this finding is in good agreement with the data for ZnS samples grown from the melt with an addition of more than 0.5 mol % of zinc oxide [11]. Simultaneously, as noted in [11], the number of defects in ZnS samples considerably increases and a zinc oxide phase is formed.

4. Conclusions

The isovalent substitution method for synthesizing a ZnO powder from powdered zinc sulfide obtained by chemical deposition from a water solution of zinc salt and thiourea has been discussed. Isovalent substitution of oxygen for sulfur was achieved during the isothermal annealing of a ZnS powder in air.

Examination of the PL spectra of ZnS powders annealed at various temperatures has shown that the local O_S defects and the ZnS·O substitutional solid solution are formed at relatively low annealing temperatures (about 870–920°C). At higher annealing temperatures (about 920–950°C), the ZnO·S phase is actively formed. At the annealing temperature of 1050°C, the structureless PL band in the spectra of the studied powder is localized at 500 nm; this position is characteristic of PL spectra of ZnO samples. The X-ray diffraction analysis of this powder

gives the ratio between the crystal lattice parameters c_o/a_o = 1.60, which is also characteristic of the ZnO hexagonal crystal lattice.

References

[1] D. P. Norton, Y. W. Yeo, M. P. Ivill, K. Ip., S. J. Pearton, M. F. Chisholm., and T. Steiner,. Materials Today. 7, 34, (2004).

[2] Ü. Özgür, Y. I. Alilov, C. Liu, A. Teke, M.A. Reshchikov, S. Doğan, V. Avrutin, S.-J. Cho, and H. Morkoç, J. Apl. Phys. 98, 041301, (2005).

[3] Z. L. Wang, Materials Today. 7, 26, (2004).

[4] D. Lincot, Thin Solid Films. 487, 40, (2005).

[5] H. Ohta, and H. Hosono, Materials Today. 7, 42, (2004).

[6] V. P. Magniy, M. M. Sletov, and S. V. Khusnutdinov, Izv. Akad. Nauk SSSR, Neorg. Mater. 43, 1449, (2007).

[7] V. P. Makhniy, M. M. Sletov, and S. V. Khusnutdinov, Mekhanizmy lyuminestsentsii sloev oksida tsinka, poluchennykh metodom izovalentnogo zameshcheniya, Chernovitskiy natsional'nyy universitet, Chernovtsy, 2009.

[8] T. I. Goglidze, I. V. Dement'yev, A. P. Zadorozhnyy, and R. L. Sobolevskaya, Studia Universitatis, USM. 107, (2011).

[9] D. I. Dimova-Ayakova, and V. A. Nikitenko, Trudy Mosk. Energ. Inst. 192, 86, (1974).

[10] Ye. A. Chechotkin et al., Izv. Akad. Nauk SSSR, Neorg. Mater. 14, 1393, (1978).

[11] N. K. Morozova, and V. A. Kuznetsov, Sul'fid tsinka. Poluchenie i opticheskie svoistva, Nauka, Moscow, 1987.

[12] R. Dingle, Phys. Rev. Lett. 23, 579, (1969).

[13] P. Dahan, V. Fleurov, P. Thurian, R. Heitz, A. Hoffmann, and I. Brozer, J. Phys. Condens. Matter. 10, 2007, (1988).

[14] S. A. Studenkin, N. Golego, and M. Cocivera, J. Appl. Phys. 84, 2287, (1998).

[15] F. M. Leiter, H. R. Alves, A. Hofstaetter, D.M. Hoffmann, and B.K. Meyer, Phys. Stat. Solidi B. 226, R4, (2001).

[16] A. F. Kohan, G. Ceder, D. Morgan, and C. G. Van de Walle, Phys. Rev. B. 61, 15019, (2000).

[17] H. -J Egelhaaf, and D. Oelkrug, J. Cryst. Growth. 161, 190, (1996).

[18] K. Vanheusden, C. H. Seager, W. L. Warren, D. R. Tallant, and A. Voigt, J. Appl. Phys. Lett. 68, 403, (1996). K. Vanheusden, W. L. Warren, C. H. Seager, D. R. Tallant, J. A. Voigt, and B. E. Gnade, J. Appl. Phys. 79, 7983, (1996). K. Vanheusden, C. H. Seager, W.L. Warren, D.R. Tallant, J. Caruso, M. J. Hampden-Smith, and T. T. Kodas, J. Lumin. 75, 11, (1997).

CATHODOLUMINESCENCE AND MATERIAL CHARACTERIZATION

M. Nazarov

Institute of Applied Physics, Academy of Sciences of Moldova, Academiei str. 5, Chisinau, MD-2028, Republic of Moldova
E-mail: mvnazarov@mail.ru

(Received April 20, 2016)

Abstract

Some new and nonconventional methods of materials investigation, such as color cathodoluminescence and composite cathodoluminescent and back-scattering electron contrast in SEM, are presented and explained. Advantages of these methods are demonstrated in studying the $SrAl_2O_4:Eu^{2+}$, Dy^{3+} luminescent phosphor and artificial diamonds.

1. Introduction

The emission of ultraviolet, visible, or infrared light stimulated by electron bombardment is known as cathodoluminescence (CL; from cathode rays as J. J. Thompson described electrons in 1897). CL was first studied by William Crookes in 1879. He discovered that $CaWO_4$ scheelite placed opposite the cathode in a vacuum discharge tube yielded spectacular fluorescence. He concluded that some particles traveled from the cathode to the target causing the fluorescence well before Thomson discovered the electron. Crookes also studied luminescence from many other minerals (diamond, ruby, sapphire, zircon, etc.). However, systematic observations and discussion of CL did not take place until 1965, when Smith and Stenstrom studied CL with a microprobe [1]. The pioneering CL studies were carried out with a CL microscope, which fundamentally is a petrographic microscope to which a cathode gun is attached. Subsequently, an electron-probe microanalyzer and, especially, a scanning electron microscope were utilized to generate high-resolution high-magnification CL images.

It should be noted that CL-modes being incorporated into a SEM instrument (CL-SEM) give both the spectral and spatial information with high resolution. In geology, mineralogy, and materials science, a scanning electron microscope with specialized optical detectors, or an optical CL microscope, is used to examine internal structures of luminescent materials in order to get information on the composition, growth, and quality of the material. CL in semiconductors occurs because the impingement of a high energy electron beam onto a semiconductor will result in the promotion of electrons from the valence band into the conduction band, leaving behind a hole. Recombination of an electron and a hole provide the emission of a photon. The energy (color) of the photon, as well as the probability of emission of a photon rather than a phonon, depends on the type, purity, and defect state of the material. In this case, the semiconductor examined can, in fact, be almost any non-metallic material. In terms of the band structure, classical semiconductors, insulators, ceramics, gemstones, minerals, glasses, and powders can be treated in the same way.

The luminescence of most phosphors comes from a few sites (activator centers) occupied

by selected chemical impurities incorporated into the matrix or host solid. Direct excitation of the activator is only possible with ultraviolet and/or visible radiation. High-energy electron beam excitation always excites the host lattice. Because of the complex mode of interaction of cathode rays with phosphors, the energy efficiency of light production by CL is lower than the best efficiencies provided by photoluminescence (PL). The main advantage of CL spectroscopy in comparison with PL is the possibility of local measurements with geometrical resolution less than 1 μm, while PL is an integrated mode.

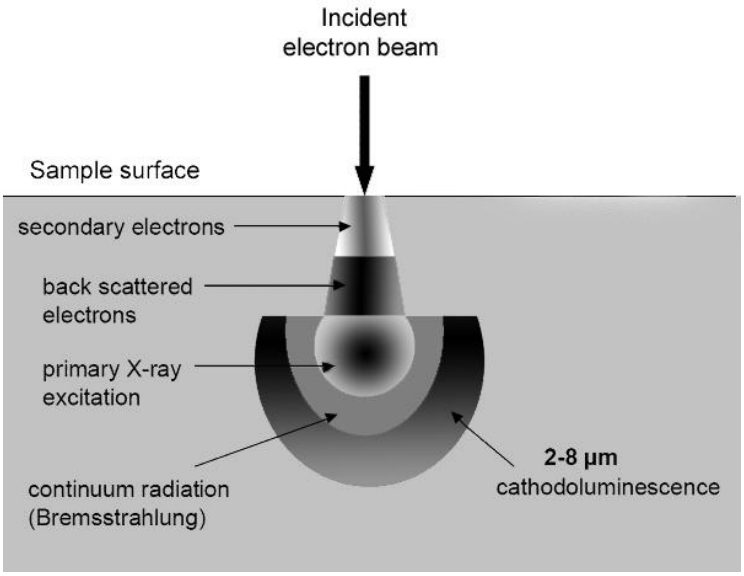

Fig. 1. Schematic shapes of electron interaction volumes.

The penetration depth of the incident beam and, therefore, the excited volume in the sample depend on the energy of the incident electrons and the atomic number of the studied material. If secondary and back-scattered electrons are formed from the subsurface layer, CL is typically generated from depths down to 2–8 μm; it is a volume effect. Thus, the geometrical resolution in CL depends not only on electron beam diameter, but also on the CL interaction volume. In fact, it can be about 1 μm. A 3D image of the sample can be obtained if the scanning mode and electron energy variation are combined. Usually, a CL mode is applied in phosphor investigations in combination with other modes in SEM, such as SE or BSE (see the next paragraph).

2. Investigation methods

2.1 Monochromatic CL

An example of CL application to a ZnO–Zn powder sample is shown in Fig. 2. The dominant CL emission peak for ZnO–Zn is located at 495 nm.

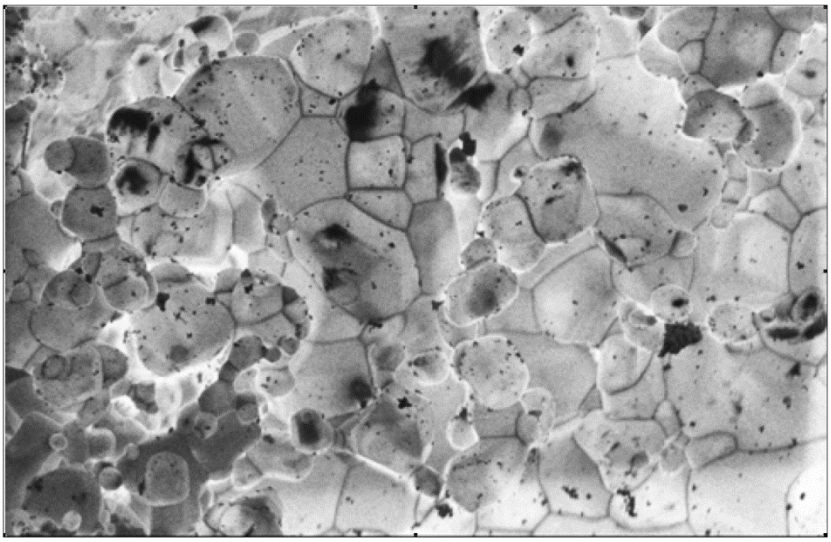

Fig. 2. CL image of ZnO–Zn at 495 nm and 1 kV. Horizontal Width of Field (HWF) of 58 μm.

This work has demonstrated the capabilities of low-voltage scanning CL microscopy for high-resolution spatially resolved characterization of the luminescence properties of CL phosphors.

2.2 Panchromatic or color CL

Among the different CL-SEM modes, the most informative is color CL (CCL). The use of color contrast was shown to increase the information content of color images in comparison with the black-and-white counterpart by about two orders of magnitude [2]. Previously, the CCL-SEM mode was used for a complex characterization of different organic, dielectric, and semiconductor luminescent materials [2–5]. Here, we show one of the examples of CCL application to phosphors in a powder form.

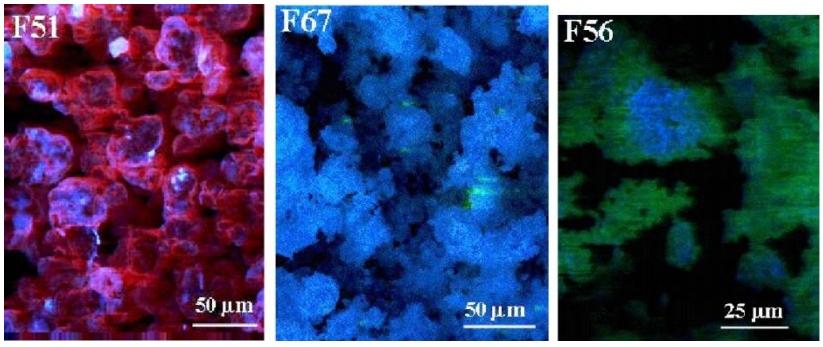

Fig. 3. Panchromatic images of nonactivated $CaWO_4$ (F67) and the sample activated with Eu^{3+} (F51) and Tb^{3+} (F56) (original blue color for host lattice emission, red color for Eu incorporations and green for Tb).

Mechanisms leading to the emission of light from phosphors are rather similar for all forms of excitation. In all cases, luminescence arises owing to stimulation of the substance to an

excited state. This excitation involves an input of energy from a source of suitable radiation, e.g., from an electron beam at CL. Solids centers of luminescence contain atoms, ions, or groups of ions located near the lattice imperfections. An imperfection in the host lattice may be produced by introducing an activator or by producing a vacancy. The radiative transition of an excited center to the ground state is accompanied by the emission of light.

A special attachment for CCL-SEM examinations of topography and morphology of powder samples and a CL spectrometer for local CL measurements are shown in Fig. 4.

2.3 Composite CL and back-scattering electron contrast in SEM

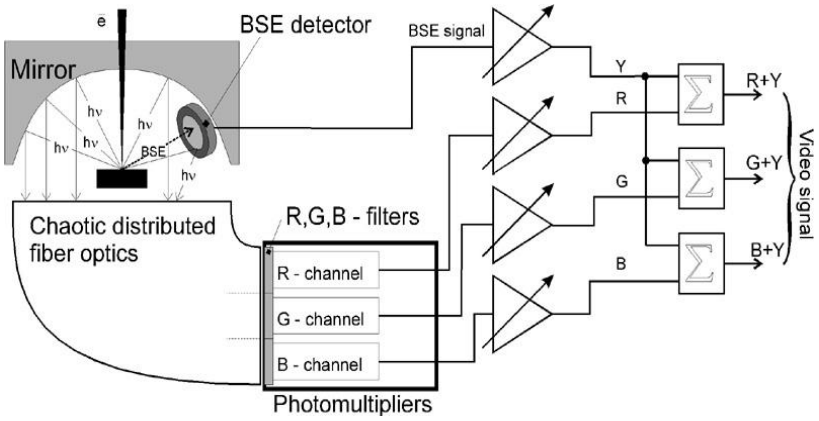

Fig. 4. CCL- SEM attachment for CCL.

A schematic diagram of the (CCL+BSE) detector unit in SEM is presented in Fig. 4. The basic equipment comprises a Stereoscan MK-IIA SEM instrument integrated with a CCL light collector and a solid state barrier counter for the measurement of BSE current. The BSE detector is located near the specimens under a parabolic mirror. Undistorted CCL and BSE signals are detected simultaneously during electron beam scanning.

CL is transmitted by optical fibers from the specimen chamber. Later, using three R-, G-, and B-filters, the CL signal is transformed into electric video signals by photomultipliers. These signals are multiplied by preamplifiers which set the amplification ratio and zero value (black level). The BSE detector is integrated with the amplifier and operates at negative bias that increases the electrical and noise stability. The electric potential of the detector body is chosen to be identical with that of the microscope column potential to eliminate its action on the electron beam. The amplifier of the BSE signal also allows varying the amplification factor and the black level of the video signal. After pre-amplification, the R-, G-, B- and BSE (Y)-signals are summed, as shown in Fig. 4. As a result, we have three video signals: R+Y, G+Y, and B+Y, which are transformed into digital form and are displayed on the computer screen. The above-described technique of signal detection measures the final color of the image, as the true color of luminescence on the specimen, and the gray level of the image is tuned by the BSE-signal value

which reflects the specimen topography. The dynamic interval of the final signal is limited by the capability of the human eye to perceive and balance between CCL and BSE contrast that is fixed by amplification coefficients in the R-, G-, B-, and Y channels. Using others SEM modes, we can apply the above principle to different signals, for example, the induced current signal (Y-channel) + (CCL mode for RGB-channels), and so forth.

Composite CCL+BSE contrast in scanning microscopy is a new type of SEM mode that is a fairly promising tool for the investigation of luminescence materials. The (CCL + BSE) – SEM images with both fine structure and color information may be able to simplify the observation, interpretation, and analysis of different nature specimens, since the human eye is essentially an organ for observing color and can distinguish thousands of color hues and intensities.

The following literature can be used for further CL reading [6–8].

3. Results and discussion

3.1. Structure, morphology, and luminescence of $SrAl_2O_4:Eu^{2+}$, Dy^{3+}

Figure 5 shows the main XRD patterns of $SrAl_2O_4:Eu^{2+}$, Dy^{3+} annealed in an active carbon atmosphere at 1250°C for 2 h.

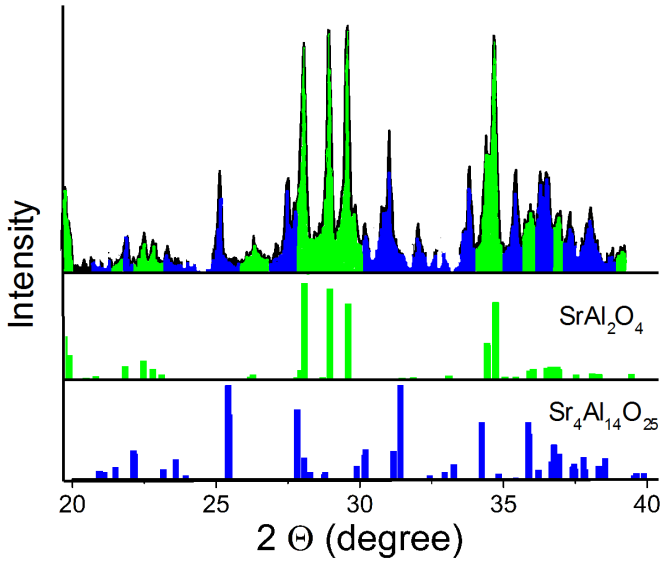

Fig. 5. XRD patterns of the synthesized phosphor.

It is evident from Fig. 5 that the XRD patterns include two phases—$SrAl_2O_4$ and $Sr_4Al_{14}O_{25}$—indicating the formation of mixed oxide phases. With an increase in the firing temperature to 1250°C, the XRD peaks becomes sharper and stable phases of $SrAl_2O_4$ and $Sr_4Al_{14}O_{25}$ with higher crystallinity can be obtained.

PL spectroscopy indirectly confirms the presence of two phases. The detailed results of

these experiments are given in our previous papers [9–11]. Here, in Fig. 6, we show the emission spectra of the synthesized phosphor.

The asymmetry of PL emission intensity allows us to decompose this spectrum into blue and green bands peaking around 490 and 520 nm. These bands correspond to $Sr_4Al_{14}O_{25}$ (490 nm) and $SrAl_2O_4$ (520 nm) phases doped with Eu^{2+}.

The direct confirmation of this hypothesis follows from CL measurements. The results of experimental investigations of the prepared phosphors by secondary electrons, CCL, and a combined signal are presented in Fig. 7. In all the experiments, the accelerating voltage in SEM was 20 kV and the beam current was 100 nA. The diameter of the electron beam did not exceed 0.1 μm. We used a recording system consisting of three multipliers with different light filters (R, G, B) and a multichannel device connected to photomultipliers. It allows simultaneous transmission of video signals on all channels in any pre-determined range of the spectrum. Images of the surface under study and the respective CL emission from the surface were displayed on video monitors.

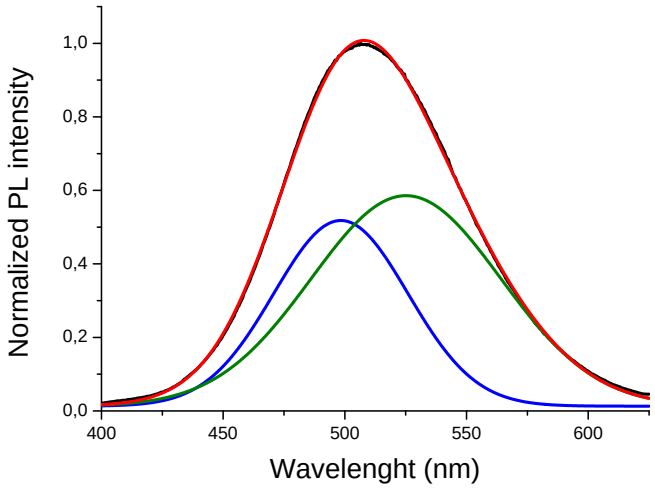

Fig. 6. Decomposition of total PL intensity into blue and green bands.

In secondary electrons (Fig. 7a) we can see only the topography of agglomerated powder. CCL (Fig. 7b) shows the spatial distributions of different CL spectral bands (green 520 nm and blue 490 nm) corresponding to $SrAl_2O_4$:Eu^{2+}, Dy^{3+} and $Sr_4Al_{14}O_{25}$:Eu^{2+}, Dy^{3+}, respectively. This direct experiment really confirms the existence of two different phases with different colors. Moreover, the absence of red color centers proves that the entire Eu^{3+} was reduced to Eu^{2+} during synthesis. The combination of CCL with the secondary electron image (Fig. 7c) provides comparison of the analytical CL image with the surface topography of the sample.

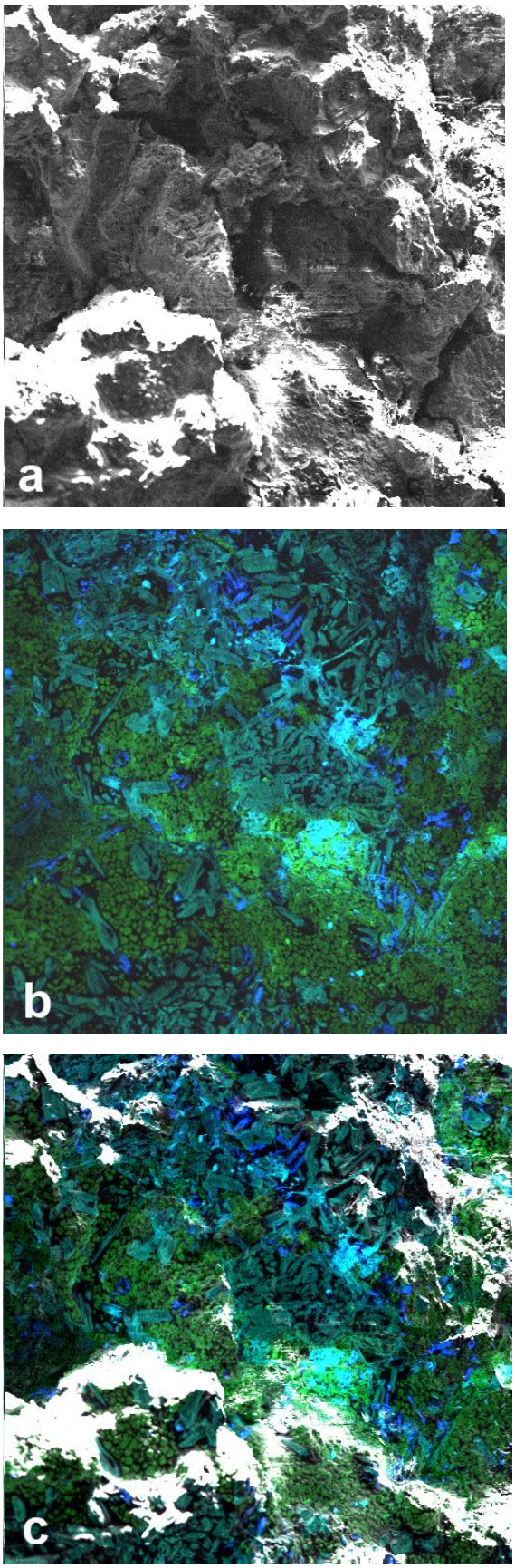

Fig. 7. CCL-SEM images of $SrAl_2O_4:Eu^{2+}$, Dy^{3+} in different modes: (a) secondary electrons (SE), (b) CCL, and (c) SE + CCL. Horizontal field width = 1000 μm.

3.2. CCL of artificial diamonds

To demonstrate the advantages of the CCL method in comparison with the black/white contrast, we present some examples of different types of materials that we examined: II–VI and III–V compounds, I–V group semiconductors, ceramics, phosphors, minerals, biomedical specimens, etc. For example, Fig. 8 shows the CCL images of some artificial diamonds.

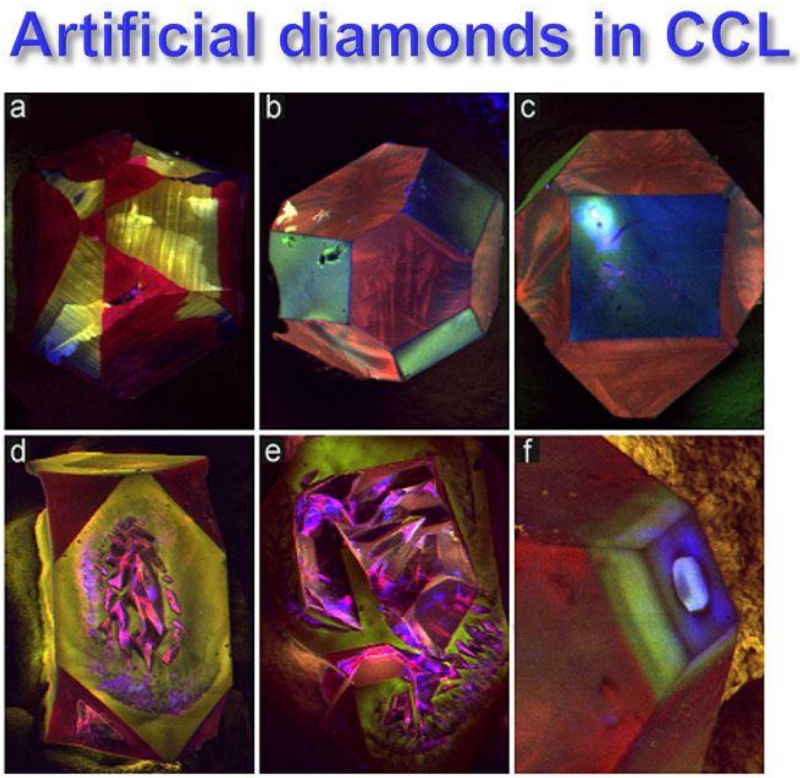

Fig. 8. CCL images of some artificial diamonds.

The information capacity of a real CCL image is more than two orders of magnitude higher than that of a black-and-white image used in commercial SEM machines. The detection limit of dopant concentration can be 10 at/cm, which is four orders of magnitude lower than that of the X-ray analyzer and SIMS technique. The sensitivity to the B/C ratio (for diamonds) is 1 ppm; a color contrast image for contrast intervals of $0 < K < 5\%$ is able as black/white contrast image for $K > 5\%$ only; time express analysis: 6 s (frame time); spatial resolution is 0.2 + 0.5 mm for bulk materials and better than the optical resolution for fine materials; the unique CCL-unit design allows interfacing with most SEM instruments. The CCL-system consists of the following components: (1) a SEM specific specimen 12-position stage including an optical mirror, fiber optics, a light detector, and preamplifiers; (2) microprocessor based control and readout electronics; and (3) a video display with a keyboard input.

The main available applications are as follows.

—Microanalysis of materials, mapping of defects, measurement of their densities, impurity segregation studies.

—Acquisition of information on the electronic energy band structure, analysis of luminescence centers and composition.
—Measurement of dopant concentration, minority carrier diffusion length, minority carrier life-time and carrier life-time mapping.
—Analysis of semiconductor devices, analysis of degradation of optoelectronics devices (laser target, light emitting diodes, solid detectors, solar cells, etc.).
—Depth resolved (3D) analysis of defects in ion-implanted samples and epitaxial multilayers.
—Evaluation of various types of diamonds (natural and synthesized diamonds, CVD-diamond films and related materials, such as SiC, etc.) because it distinguishes the type, size and distribution of defects within a crystal on a color monitor.
—Characterization of diamond films; the CCL–SEM technique is available to investigate the B/C ratio, local concentration of dopants, and spatial distribution of the dopant in diamonds. The impurity concentration and structural imperfection should be strictly controlled to obtain the required thermal, optical, or electrical properties, i.e., diamonds with new characteristics.
—Certification (finger print) of gem-quality and tool-quality diamonds.

4. Conclusions

A number of advantages of real color contrast application in the SEM in comparison with the black/white contrast for local CL-microanalysis of materials have been shown.

Strong and bright green luminescence has been observed and registered from $SrAl_2O_4:Eu^{2+}$ Dy^{3+} in different modes.

PL and CCL-SEM have been used for the complex examination of $SrAl_2O_4:Eu^{2+}$ Dy^{3+} powder luminescent materials.

CL images obtained in SEM in real colors can be used for a rapid examination of spatial and spectral characteristics of powder and bulk materials produced by different technologies. This method can be recommended as a useful tool in electron microscopy for the complex investigation of luminescent materials.

References

[1] J. V. Smith and R. C. Stenstrom, J. Geol. 13, 627, (1965).
[2] G. V. Saparin and S. K. Obyden, Eur. Microsc. Anal. **7**(3), 7, (1993).
[3] T. A. Nazarova, G. V. Saparin, S. K. Obyden, and P. I. Ivannikov, Scanning 19(1), 48 (1997).
[4] M. V. Nazarov, T. A. Nazarova, G. V. Saparin, and S. Obyden, Eur. Microsc. Anal. 12(4), 21, (1998).
[5] S. K. Obyden, P. V. Ivannikov, and G. V. Saparin, Scanning 19, 533, (1997).
[6] B. G. Yacobi. and D. B. Holt, Cathodoluminescence Microscopy of Inorganic Solids, Plenum, New York, 1990.
[7] L. Ozawa, Cathodoluminescence: Theory and Applications, VCH, Basel, 1991.
[8] L. Ozawa, Cathodoluminescence and Photoluminescence: Theories and Practical Applications, CRC Press, Boca Raton, 2007.

[9] Nor Nazida, M.N. Ahmad-Fauzi, M. Nazarov, A. Azizan, and K. Shah, Mold. J.Phys. Sci. 11, 1–2, 78, (2012).
[10] S. C. M. Calyn, M. Nazarov, A. Nor Nazida, and M.N. Ahmad-Fauzi, Mold. J. Phys. Sci. 11,1–2, 112, (2012).
[11] M. Nazarov, A. Nor Nazida, A. Azizan, K. Shah Rizal1, S. C. M. Calyn, and M.N. Ahmad-Fauzi, Mold. J. Phys. Sci. 11, 1–2, 67, (2012).

PHONON DISPERSION ABOVE THE PEIERLS STRUCTURAL TRANSITION IN TTF-TCNQ ORGANIC CRYSTALS

Silvia Andronic and Anatolie Casian

Technical University of Moldova, Stefan cel Mare Avenue 168, Chisinau, MD-2004 Republic of Moldova
E-mail: andronic_silvia@yahoo.com

(Received May 12, 2016)

Abstract

The softening of acoustic phonons above the Peierls structural transition in quasi-one-dimensional (Q1D) TTF-TCNQ organic crystals is studied. Unlike other papers, a more complete physical model is applied to consider simultaneously two the most important electron−phonon interactions. The first is similar to that of deformation potential, and the second one is of polaron type. Analytic expressions for the phonon Green function and for the phonon polarization operator are obtained in the random phase approximation. The effects of interchain interaction on the phonon dispersion and Peierls critical temperature are analyzed.

Introduction

In recent years, investigation of quasi-one-dimensional (Q1D) organic crystals has excited special interest. These materials exhibit unusual properties [1–3]. In addition, low dimensionality of these structures, which can be considered almost one dimensional, makes them an ideal bench for testing theoretical models. Organic nanomaterials have large potential applications in electronics, sensing, energy-harnessing, and quantum-scale systems [4]. It has been also demonstrated that the highly conducting Q1D organic crystals may have very promising thermoelectric applications [5–7]. The most studied Q1D organic crystals are those of the tetrathiofulvalinium tetracyanoquinodimethane (TTF-TCNQ) type. However, not all parameters of this material are well determined. In this paper, we propose to use the Peierls structural transition to provide a more accurate determination of some parameters of this crystal.

This phenomenon has been theoretically predicted by Rudolf Peierls. According to Peierls, at some lowered temperatures, a one-dimensional metallic crystal with a half filled conduction band has to pass in a dielectric state with a dimerized crystal lattice. This temperature is referred to as the Peierls critical temperature. The Peierls transition has been studied by many authors (see [8–12] and references therein).

Recently, the physical model of Q1D organic crystals has been completed by an additional electron-phonon interaction mechanism. It takes into account the fluctuations due to acoustic longitudinal phonons of the polarization energy of molecules surrounding the conduction electron [13–15].

In [16], the Peierls structural transition in Q1D crystals of TTF-TCNQ type was investigated in a 1D approximation. Renormalized acoustic phonon frequencies $\Omega(q)$ as functions

of wave number q were calculated (i) provided that the conduction band is half filled and the dimensionless Fermi momentum $k_F = \pi/2$ and (ii) provided that the concentration of conduction electrons is reduced and the band is filled up to a quarter of the Brillouin zone, $k_F = \pi/4$. The Peierls critical temperature was established in both cases.

A 2D physical model for real TTF-TCNQ crystals was investigated in [17]. The effects of interchain interaction on the dispersion of renormalized phonons and on Peierls critical temperature were analyzed. The Peierls critical temperature was determined.

In [18], a 3D physical model of the crystal was studied. The Peierls transition was investigated for the case where the dimensionless Fermi momentum is $k_F = 0.59\pi/2$ for different values of parameters d_1 and d_2 which represents the ratio of the transfer energy in the transversal y and z directions to the transfer energy along the x direction of conductive chains. In addition, the polarization operator as a function of temperature was calculated for different values of increase or decrease δ in Fermi momentum k_F, which is determined by an increase or decrease in the carrier concentration. In this paper, the numerical modellings were performed for the sound velocity values at low temperatures taken from [19]: $v_{s1} = 3.4\cdot10^5$ cm/s along chains, $v_{s2} = 5.25\cdot10^5$ cm/s in the a direction and $v_{s3} = 5.25\cdot10^5$ cm/s in the c direction. However, more exact calculations showed that the sound velocity in the transversal direction cannot be higher the sound velocity along the chains.

The aim of this study is to present a detailed modeling of the Peierls transition in TTF-TCNQ crystals in a 3D approximation. The phonon Green function is calculated in the random phase approximation. The effects of interchain interaction on the dispersion of renormalized phonons and on Peierls critical temperature are analyzed. The results obtained in the 3D physical model are commented in detail.

1. Physical model in a 3D approximation

The structure and proprieties of TTF-TCNQ crystals are described in many papers (see [1] and references therein). A quasi-one-dimensional organic crystal of TTF-TCNQ is composed of TCNQ and TTF linear segregated chains. The TCNQ molecules are strong acceptors, and the TTF molecules are donors. Because the conductivity of TTF chains is much lower than that of TCNQ chains, we can neglect them in the first approximation. Thus, in this approximation, the crystal is composed of strictly one-dimensional chains of TCNQ that are packed in a three-dimensional crystal structure. The crystal lattice constants are a = 12.30 Å, b = 3.82 Å, and c = 18.47 Å, where b is in the chain directions.

The Hamiltonian of the 3D crystal in the tight-binding and nearest neighbor approximations has the form

$$H = \sum_{\boldsymbol{k}} \varepsilon(\boldsymbol{k}) a_{\boldsymbol{k}}^{+} a_{\boldsymbol{k}} + \sum_{\boldsymbol{q}} \hbar\omega_{\boldsymbol{q}} b_{\boldsymbol{q}}^{+} b_{q} + \sum_{\boldsymbol{k},\boldsymbol{q}} A(\boldsymbol{k},\boldsymbol{q}) a_{\boldsymbol{k}}^{+} a_{\boldsymbol{k}+\boldsymbol{q}} (b_{\boldsymbol{q}} + b_{-\boldsymbol{q}}^{+}), \tag{1}$$

In expression (1), $\varepsilon(\boldsymbol{k})$ represents the energy of a conduction electron with 3D quasi-wave vector $\boldsymbol{k}$ and projections (k_x, k_y, k_z), $a_{\boldsymbol{k}}^{+}$, $a_{\boldsymbol{k}}$ are the creation and annihilation operators of this electron. Carrier energy $\varepsilon(\boldsymbol{k})$ is measured from the conduction band bottom:

$$\varepsilon(\boldsymbol{k}) = 2w_1(1-\cos k_x b) - 2w_2(1-\cos k_y a) - 2w_3(1-\cos k_z c), \tag{2}$$

where w_1, w_2, and w_3 are the transfer energies of a carrier from one molecule to another along the

chain, *x* direction, and in perpendicular—*y* and *z*—directions. In (1), $b_{\boldsymbol{q}}^{+}$, $b_{\boldsymbol{q}}$ are the creation and annihilation operators of an acoustic phonon with three-dimensional wave vector $\boldsymbol{q}$ and frequency $\omega_{\boldsymbol{q}}$. The second term in Eq. (1) is the energy of longitudinal acoustic phonons

$$\omega_q^2 = \omega_1^2 \sin^2(q_x b/2) + \omega_2^2 \sin^2(q_y a/2) + \omega_3^2 \sin^2(q_z c/2), \tag{3}$$

where ω_1, ω_2, and ω_3 are the limit frequencies in the *x*, *y*, and *z* directions:

$$\omega_1 = \frac{2v_{s1}}{b},\ \omega_2 = \frac{2v_{s2}}{a},\ \omega_3 = \frac{2v_{s3}}{c}, \tag{4}$$

where v_{s1}, v_{s2}, and v_{s3} represent the values of the sound velocity at low temperatures along the chains (in *b* direction) and in perpendicular directions (in *a* and *c* directions).

The third term in Eq. (1) represents the electron–phonon interaction. It contains two important mechanisms. The first one is of the deformation potential type; it is determined by the fluctuations of energy transfer w_1, w_2, and w_3 due to the intermolecular vibrations (acoustic phonons). The coupling constants are proportional to derivatives w_1', w_2', and w_3' of w_1, w_2, and w_3 with respect to intermolecular distances, $w_1' > 0$, $w_2' > 0$, $w_3' > 0$. The second mechanism is similar to that of polaron. This interaction is conditioned by the fluctuations of the polarization energy of the molecules surrounding the conduction electron. The coupling constant of this interaction is proportional to the average polarizability of the molecule α_0. Because α_0 is roughly proportional to the volume of molecule, this interaction is important for crystals composed of large molecules, such as TCNQ.

The square module of the matrix element of electron–phonon interaction is represented in the following form:

$$\left|A(\boldsymbol{k},\boldsymbol{q})\right|^2 = 2\hbar w_1'^2/(NM\omega_{\boldsymbol{q}}) \times \{[\sin(k_x b) - \sin(k_x - q_x, b) + \gamma_1 \sin(q_x b)]^2 + \tag{5}$$

$$+ d_1^2[\sin(k_y a) - \sin(k_y - q_y, a) + \gamma_2 \sin(q_y a)]^2 + d_2^2[\sin(k_z c) - \sin(k_z - q_z, c) + \gamma_3 \sin(q_z c)]^2\},$$

In Eq. (5), M is the mass of the molecule, N is the number of molecules in the basic region of the crystal, $d_1 = w_2/w_1 = w_2'/w_1'$, $d_2 = w_3/w_1 = w_3'/w_1'$, parameters γ_1, γ_2, and γ_3 describe the ratio of amplitudes of the polaron-type interaction to the deformation potential one in the *x*, *y*, and *z* directions:

$$\gamma_1 = 2e^2\alpha_0/b^5 w_1',\ \gamma_2 = 2e^2\alpha_0/a^5 w_2',\ \gamma_3 = 2e^2\alpha_0/c^5 w_3', \tag{6}$$

To deduce an expression for a renormalized phonon Green function, we apply a random phase approximation. From exact series of the perturbation theory for the phonon Green function, we sum up the diagrams containing 0, 1, 2 …∞ closed loops of two electron Green functions that make the most important contribution. For the Fourier component of the phonon Green function $D(\boldsymbol{q}, \Omega)$, we obtain

$$D(\boldsymbol{q},\Omega) = D_0(\boldsymbol{q},\Omega) - D_0(\boldsymbol{q},\Omega)\Pi(\boldsymbol{q},\Omega)D(\boldsymbol{q},\Omega) \tag{7}$$

where $\Pi(\boldsymbol{q},\Omega)$ is the phonon polarization operator, $D_0(\boldsymbol{q},\Omega)$ is the free phonon Green function, $\boldsymbol{q}$ is the wave vector of longitudinal acoustic phonons, and $\Omega(\boldsymbol{q})$ is the renormalized phonon frequency. The real part of the polarization operator is presented in the form:

$$\mathrm{Re}\,\overline{\Pi}(\boldsymbol{q},\Omega) = -\frac{\overline{N}}{2\pi^3\hbar\omega_{\boldsymbol{q}}}\int_{-\pi}^{\pi}dk_x\int_{-\pi}^{\pi}dk_y\int_{-\pi}^{\pi}dk_z\left|A(\boldsymbol{k},-\boldsymbol{q})\right|^2\times\frac{n_{\boldsymbol{k}}-n_{\boldsymbol{k}+\boldsymbol{q}}}{\varepsilon(\boldsymbol{k})-\varepsilon(\boldsymbol{k}+\boldsymbol{q})+\hbar\Omega} \tag{8}$$

Hereinafter, $\boldsymbol{k}$ and $\boldsymbol{q}$ are dimensionless vectors, $\overline{N}$ represents the number of elementary cells in the basic region of the crystal, $N = r\overline{N}$, where r is the number of molecules in the elementary cell, $r = 2$. In (8), $A(\boldsymbol{k},-\boldsymbol{q})$ is the matrix element of electron–phonon interaction presented in Eq. (2), $\varepsilon(\boldsymbol{k})$ is the carrier energy, $\hbar$ is the Planck constant, $n_{\boldsymbol{k}}$ is the Fermi distribution function. $\Omega(\boldsymbol{q})$ is determined by the pole of function $D(\boldsymbol{q},\Omega)$ and is obtained from the transcendent dispersion equation

$$\Omega(\boldsymbol{q}) = \omega_{\boldsymbol{q}}[1-\overline{\Pi}(\boldsymbol{q},\Omega)]^{1/2} \tag{9}$$

This equation can be solved only numerically.

2. Results and discussion

Numerical modeling was performed for the following parameters of TCNQ chains: $M = 3.7\cdot10^5\ m_e$ (m_e is the electron rest mass), $w_1 = 0.125$ eV, $w_1' = 0.2$ eVÅ^{-1}, $a = 12.30$ Å, $b = 3.82$ Å, and $c = 18.47$ Å. The sound velocity $v_{s1} = 3.42\cdot10^5$ cm/s along chains, $v_{s2} = 1.7\cdot10^5$ cm/s in the a direction and $v_{s3} = 1\cdot10^5$ cm/s in the c direction, $d_1 = 0.015$, $d_2 = 0.013$, $r = 2$ (two molecules in a unit cell), $\gamma_1 = 1.37$. The γ_2 and γ_3 parameters are determined from the relationships: $\gamma_2 = \gamma_1 2^5 b^5/(a^5 d_1)$ and $\gamma_3 = \gamma_1 2^5 b^5/(c^5 d_2)$. The dimensionless Fermi momentum is $k_F = 0.59\,\pi/2$.

$$\mathrm{Re}\,\overline{\Pi}(\boldsymbol{q},\Omega) = \frac{w_1'^2}{8\pi^3 M w_1 r\omega_q^2}\int_{-\pi}^{\pi}dx\int_{-\pi}^{\pi}dy\int_{-\pi}^{\pi}dz\times$$

$$\times\Big[\frac{(\sin(x+q_x)-\sin(x)+\gamma_1\sin(q_x))^2+d_1^2(\sin(y+q_y)-\sin(y)+\gamma_2\sin(q_y))^2+}{\cos(x)-\cos(x+q_x)+d_1\cos(y)-d_1\cos(y+q_y)+} \tag{10}$$

$$\frac{+d_2^2(\sin(z+q_z)-\sin(z)+\gamma_3\sin(q_z))^2}{+d_2\cos(z)+d_2\cos(z+q_z)-\dfrac{\hbar\Omega}{2w_1}}\Big]\times(n_{\boldsymbol{k}}-n_{\boldsymbol{k}+\boldsymbol{q}}),$$

$$n_{\boldsymbol{k}} = [\exp(\frac{-2w_1\cos(x)-2w_2\cos(y)-2w_3\cos(z)+(2w_1+2w_2+2w_3)\cos(k_F)}{k_0T}+1)]^{-1}. \tag{11}$$

The polarization operator was calculated according to expression (10).

The dependences of renormalized phonon frequencies $\Omega(q_x)$ on q_x at different temperatures and different values of q_y and q_z are shown in Figs. 1–4. The same graphs show the same dependences for initial phonon frequency $\omega(q_x)$.

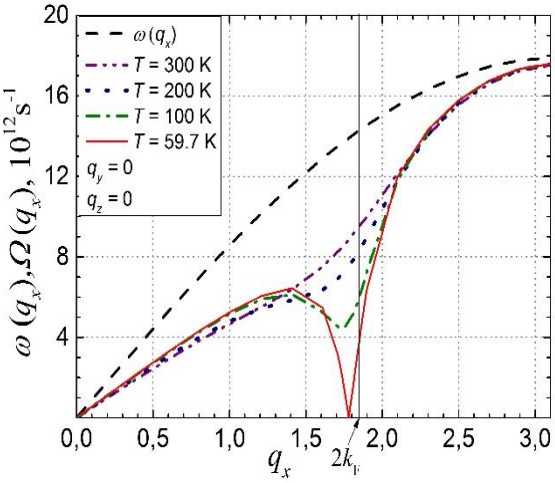

Fig.1. Renormalized phonon spectrum $\Omega(q_x)$ for $\gamma_1 = 1.37$ and different temperatures. The dashed line is for the spectrum of free phonons. $q_y = 0$ and $q_z = 0$.

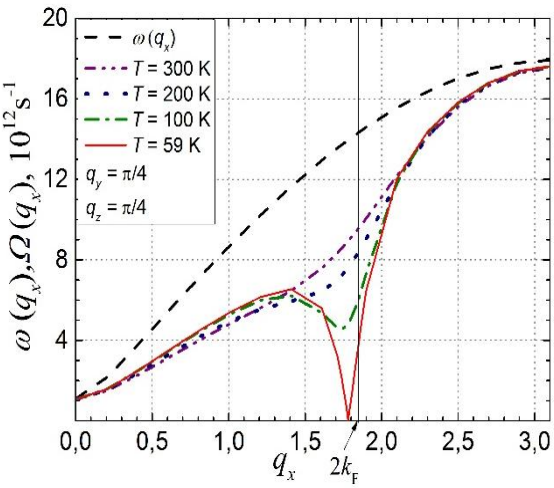

Fig.2. Renormalized phonon spectrum $\Omega(q_x)$ for $\gamma_1 = 1.37$ and different temperatures. The dashed line is for the spectrum of free phonons. $q_y = \pi/4$, $q_z = \pi/4$.

All figures show that the values of $\Omega(q_x)$ are diminished in comparison with those of frequency $\omega(q_x)$ in the absence of an electron–phonon interaction. This means that the electron–phonon interaction diminishes the values of lattice elastic constants. In addition, it is evident that, with a decrease in temperature T, the curves change their form. In dependences $\Omega(q_x)$, a minimum appears and becomes more pronounced at lower temperatures. It was expected that, at a certain temperature, $\Omega(q_x)$ will attain zero value for $q_x = 2k_F$. At this temperature, the structural Peierls transition should takes place. However, our calculations show that renormalized phonon frequencies $\Omega(q_x)$ attain zero value for $q_x = 0.58\pi$. This deviation from $q_x = 2k_F$ is caused by the deviation of k_F from $\pi/2$.

Figure 1 shows the phonon spectrum at $q_y = 0$ and $q_z = 0$. In this case, the last two terms in (5) become zero. This means that the interaction between TCNQ chains is not taken into account. The Peierls structural transition occurs in TCNQ chains alone at $T = 59.7$ K. The crystal lattice along TCNQ chains undergoes changes. A new crystalline state appears with lattice constant $4b$, which is four times larger. At this temperature, a metal–dielectric phase transition takes place, so as a gap in the carrier spectrum is fully open just above the Fermi energy. In addition, it is evident that the slope of $\Omega(q_x)$ at small q_x is diminished in comparison with that of $\omega(q_x)$. This means that the elasticity force of interaction between two nearest molecules as a consequence of electron–phonon interaction decreases. As a result, the sound velocity along the chains is diminished in a large temperature interval.

Figures 2–4 correspond to $q_y \neq 0$ and $q_z \neq 0$. It is observed that, if the interaction between TCNQ chains is taken into account ($q_y \neq 0$, $q_z \neq 0$), the Peierls critical temperature is diminished.

Figure 2 shows the $\Omega(q_x)$ dependences for $q_y = \pi/4$ and $q_z = \pi/4$ and different temperatures. One can observe that $\Omega(q_x)$ attains zero value at $T \sim 59$ K; that is, the Peierls transition takes place at this T.

Figure 3 shows the phonon spectrum at $q_y = 2k_F$ and $q_z = 2k_F$. It is evident from the graph that the Peierls critical temperature decreases further and has a value of $T \sim 56$ K. Figure 4 shows the dependences of $\Omega(q_x)$ on q_x for $q_y = \pi$, $q_z = \pi$ and different temperatures. It is observed that the transition temperature decreases even more significantly and has a value of $T \sim 54$ K. Note that this value corresponds to the experimental data.

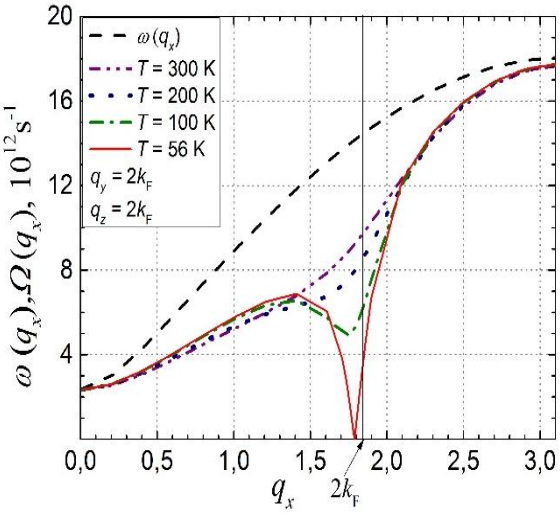

Fig.3. Renormalized phonon spectrum $\Omega(q_x)$ for $\gamma_1 = 1.37$ and different temperatures. The dashed line is for the spectrum of free phonons. $q_y = 2k_F$, $q_z = 2k_F$.

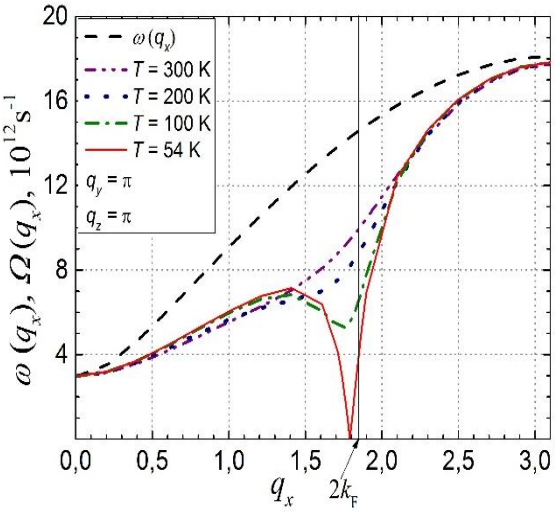

Fig.4. Renormalized phonon spectrum $\Omega(q_x)$ for $\gamma_1 = 1.37$ and different temperatures. The dashed line is for the spectrum of free phonons. $q_y = \pi$, $q_z = \pi$.

3. Conclusions

We have studied the effect of the Peierls transition on the phonon spectrum in quasi-one-dimensional organic crystals of TTF-TCNQ in a 3D approximation. A more complete crystal model has been applied to take into account two the most important electron–phonon interactions. One of them is of the deformation potential type. The other interaction is similar to that of a polaron. The ratio of amplitudes of the second electron–phonon interaction to the first one along the chains and in the transversal direction is denoted by γ_1, γ_2, and γ_3, respectively. Analytical expressions for the polarization operator and for the renormalized phonon Green function have been derived in a random phase approximation. Numerical calculations for renormalized phonon spectrum $\Omega(q_x)$ at different temperatures have been presented. It has been found that, at $q_y = 0$ and $q_z = 0$, if the interaction between TCNQ chains is neglected, the Peierls transition begins at $T \sim 59.7$ K (as confirmed experimentally) in TCNQ chains alone and reduces considerably the electric conductivity. Due to interchain interaction, the transition is completed at $T \sim 54$ K. It has been shown that the electron–phonon interaction diminishes $\Omega(q_x)$ and reduces the sound velocity in a large temperature interval. The frequency $\Omega(q_x)$ is about zero for $q_x = 0.58\pi$. The crystal

lattice changes from the initial state with lattice constant *b* to a new crystalline state with constant 4*b*.

Acknowledgments. The authors acknowledge the support of the scientific program of the Academy of Sciences of Moldova under project no. 14.02.116F.

References

[1] D. Jerome, J. Supercond. Novel Magn. 25, 633, (2012).
[2] J. P. Pouget, Physica B 407, 1762, (2012).
[3] X. Sun , L. Zhang , C. a. Di , Y. Wen , Y. Guo , Y. Zhao , G. Yu , and Y. Liu , Adv. Mater., 23 , 3128, (2011).
[4] Organic Nanomaterials: Synthesis, Characterization, and Device Applications (ed. by T. Torres, G. Bottari), John Wiley & Sons, Inc., Hoboken, NJ, USA, 2013.
[5] A. Casian., Thermoelectric Handbook, Macro to Nano, Ed. by D. M. Rowe, CRC Press, Chapter 36, 2006.
[6] A.I Casian., J. Pflaum, and I. I. Sanduleac, J. Thermoel. 1, 16, (2015).
[7] K. Harada, M. Sumino, C. Adachi, S. Tanaka, and K. Miyazaki, Appl. Phys. Lett. 96, 253304, (2010).
[8] L. N. Bulaevskii, Usp. Fiz. Nauk 115, 263, (1975).
[9] M. Hohenadler, H. Fehske, and F.F. Assaad, Phys. Rev. B, 83, 115105, (2011).
[10] V. Solovyeva et al., J. Phys. D: Appl. Phys. 44, 385301, (2011).
[11] U. Bernstein, P. Chaikin, and P. Pincus , Phys. Rev. Lett. 34, 271, (1975).
[12] A. Chernenkaya, K. Medjanik, P. Nagel, M. Merz, S. Schuppler, E. Canadell, J. P. Pouget, and G. SchËonhense, Eur. Phys. J. B. 88: 13, (2015).
[13] A. Casian, V. Dusciac, and Iu. Coropceanu, Phys. Rev. B 66, 165404, (2002).
[14] A. Casian, Phys. Rev. B 81, 155415, (2010).
[15] I. Sanduleac, A. Casian, and J. Pflaum, J. Nanoelectron. Optoelectron., 9, 247, (2014).
[16] S. Andronic and A. Casian, Mold. J. Phys. Sci. 12, 3–4, 192, (2013).
[17] S. Andronic and A. Casian, Adv. Mater. Phys. Chem. 6, 4, 98, (2016).
[18] S. Andronic, Mold. J. Phys. Sci. 14, 1–2, 96, (2015).
[19] T. Tiedje and R. R. Haering, Solid State Commun., 23, 713, (1977).

DISPERSION LAWS AND INTERACTIONS OF THE TWO-DIMENSIONAL CAVITY MAGNETOEXCITON-POLARITONS

S. A. Moskalenko[1], E. V. Dumanov[1], Ig. V. Podlesny[1], and M. A. Liberman[2]

[1]*Institute of Applied Physics of the Academy of Sciences of Moldova, Academic str. 5, Chisinau, MD2028 Republic of Moldova*
[2]*Nordic Institute for Theoretical Physics (NORDITA) KTH and Stockholm University, Roslagstullsbacken 23, Stockholm, SE-106 91 Sweden*

(Received October 7, 2016)

Abstract

In our review, the dispersion laws of two-dimensional (2D) cavity magnetoexciton-polaritons and the interaction of 2D magnetoexcitons with wave vectors $k_{\|} = 0$ are discussed. Magnetoexcitons do appear in a system of coplanar electron–hole pairs subjected to the action of strong magnetic and electric fields both being oriented along the axis of the microcavity and perpendicular to the surface of the quantum well embedded in it. Cavity polaritons are formed as a result of the interaction between 2D magnetoexcitons and cavity photons that arbitrary propagate inside the microcavity relative to the plain of the quantum well.

Our review begins with the description of the Landau quantization (LQ) of conduction electrons and heavy holes (hhs) taking into account the Rashba spin-orbit coupling (RSOC), the Zeeman splitting (ZS) and the nonparabolicity (NP) of the dispersion law of the hhs induced by an external electric field as well as the third order chirality terms.

Two lowest Landau levels (LLLs) for the conduction electrons and three LLLs for the hhs were taken into account giving rise to six magnetoexciton states; two of them are dipole-active, two are quadrupole-active, and two are forbidden in the quantum transitions from the ground state of the crystal to the selected states.

Four optical active magnetoexciton states interact with the cavity photons leading to the formation of five cavity magnetoexciton-polariton branches. The effective masses of the lower polariton branches in the presence and absence of the RSOC were determined. Their Hopfield coefficients were determined analytically only at point $k_{\|} = 0$.

The interaction between two-dimensional (2D) spinless magnetoexcitons both with wave vectors $k_{\|} = 0$, composed of electrons and holes lying on the LLLs, can appear taking into account the virtual Coulomb scattering processes of the charged particles between the LLLs and excited Landau levels (ELLs) and their return back. The influence of the ELLs leads to the overall attraction in the Hartree approximation and to repulsion between the spinless magnetoexcitons with $k = 0$ in the Fock approximation, leading to their Bose–Einstein condensation stable against collapse. The interactions of the six spinor-type magnetoexcitons with wave vectors $k_{\|} = 0$ essentially depend on their affinities and homogeneities. Two homogeneous magnetoexcitons formed by electrons and holes in their similar spinor states do attract each other. Two heterogeneous magnetoexcitons with $k_{\|} = 0$ can form symmetric and

asymmetric states with opposite signs of interactions whatever the affinities of the partners are. Interaction constants $g(0)$ depend on magnetic field strength B as $1/B$ in the case of spinless magnetoexcitons and as $1/\sqrt{B}$ in the case of spinor-type states.

Below, a review of our recent published papers [1–7] based on predecessor investigations [7–12] is presented.

We consider a 2D coplanar electron–hole (e–h) system injected by an electric current or excited by a nonresonant laser radiation inside a quantum well (QW) embedded into a microcavity and subjected to the action of external strong magnetic and electric fields oriented along the axis of the microcavity and perpendicular to the surface to the QW. It is represented in Fig. 1.

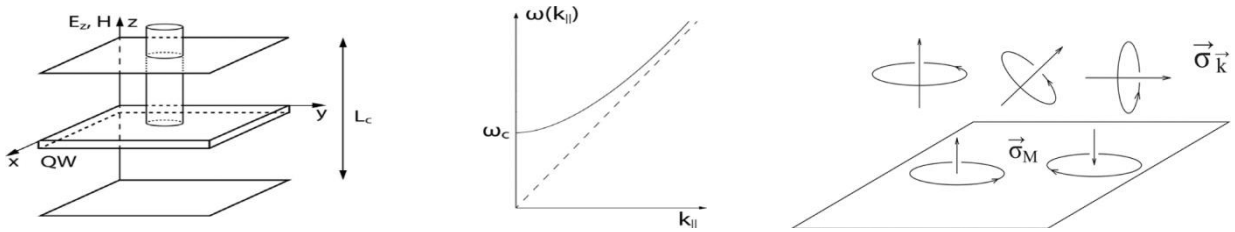

Fig. 1. 2D e–h system embedded in a microcavity and subjected to the action of external magnetic and electric fields.

The energy spectrum of the 2D cavity magnetoexciton-polaritons and their interactions are investigated in a broad range of the matter and field parameters.

The starting phenomena that determine the main properties of the system are associated with the LQ of the 2D electrons and hhs accompanied by the RSOC and ZS effects. In the case of the hhs in the GaAs-type QW_s it is necessary to take into account the supplementary NP of their dispersion law induced by an external electric field simultaneously with the third order chirality terms. Exact solutions of the LQ task under these conditions were obtained in our previous studies using the Rashba method. The dependences of the hh energy levels of the LQ on magnetic field strength *B* are shown in Fig. 2.

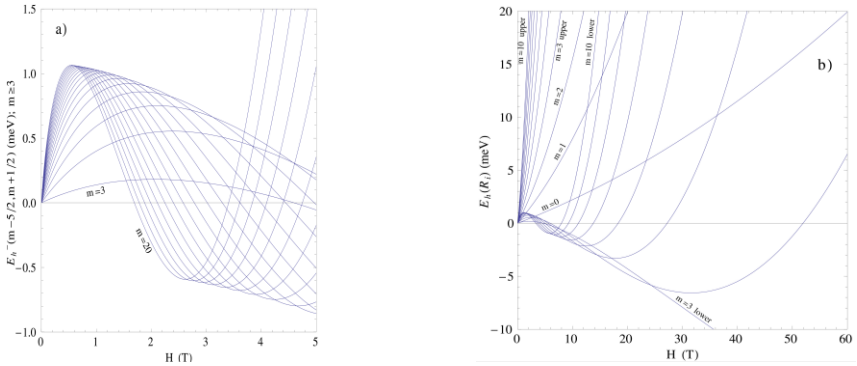

Fig. 2. Dependences of the hh LQ levels on magnetic field strength *B*.

Two LLs for conduction electron and three LLLs for hhs were taken into account. The exact solutions were used to calculate the Coulomb interactions of electrons and holes forming the magnetoexcitons, which are characterized by the binding energy, center-of-mass 2D in-plane

wave vector $\vec{k}_{\|}$, and dipole arm $\left|k_{\|}\right| l_0^2 = d$, where l_0 is the magnetic length. The structure of the 2D magnetoexciton is represented in Fig. 3.

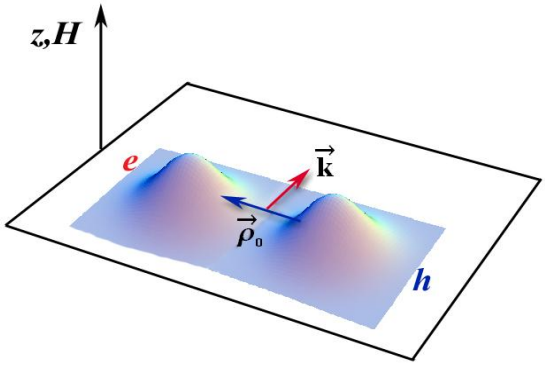

Fig. 3. Electron structure of a 2D magnetoexciton.

Combinations of the two conduction electron LLLs with three LLLs of the hh gives rise to six magnetoexciton states $F_u = (\mathrm{e}, \mathrm{R}_i; \mathrm{h}, \mathrm{R}_j),\ i = 1,2;\ j = 1,2,3;\ n = 1,2..6.$ Their energy levels as a function of magnetic field strength B are represented in Fig. 4 in the case of electric field strength $E_z = 30\,\mathrm{kV/cm}$, NP parameter $C = 20$, and different values of electron and hole g-factors g_e and g_h.

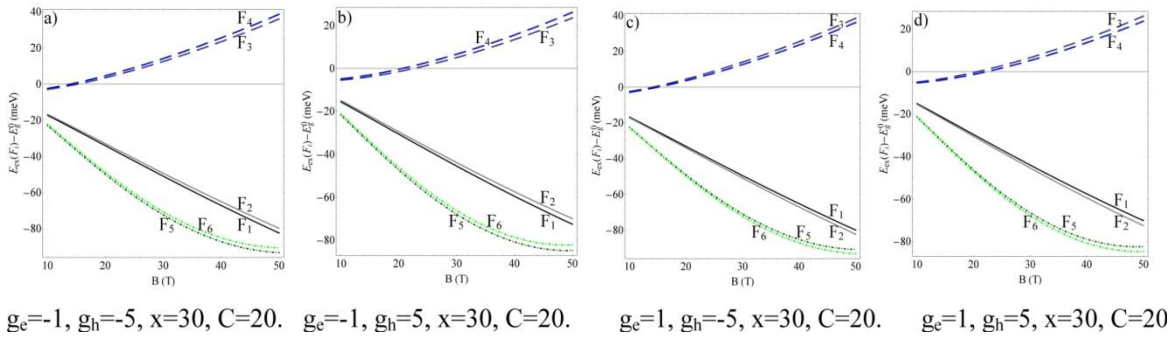

Fig. 4. Six magnetoexciton energy levels as a function of magnetic field strength.

They do exist only at the B values greater than $10T$, where the cyclotron energies of the electrons and holes are greater than the binding energies of the 2D Wannier–Mott exciton. Among six lowest-energy magnetoexciton states, two are dipole-active, two are quadrupole-active, and two are forbidden in the quantum transitions from the ground state of the crystal to the selected states. The cavity photons are propagating inside the microcavity with wave vectors $\vec{k} = \vec{a}_3 k_z + \vec{k}_{\|}$ arbitrarily oriented relative to the surface of the QW, where $\vec{a}_3$ is the unit vector along the cavity axis, $\vec{k}_{\|}$ is the in-plane wave vector, and longitudinal projection k_z has two size-quantized values $\pm \pi / L_C$, where L_C is the length of the cavity. The photons in the microcavity

are characterized by wave vectors $\vec{k}_{\uparrow,\downarrow} = \pm \frac{\pi}{L_C}\vec{a}_3 + \vec{k}_{\parallel}$, circular polarizations $\vec{\sigma}^{\pm}_{k_\uparrow}, \vec{\sigma}^{\pm}_{k_\downarrow}$, the energy spectrum with cut-off energy $E_C = \hbar\omega_C$ at point $\vec{k}_{\parallel} = 0$, and the effective mass in its vicinity equal to $m_C = \frac{\hbar \pi n_C}{cL_C}$, where n_C is the refractive index inside the cavity. Along with the circular polarization of the photons, it is possible to introduce the circular polarization of the hhs in the p-type valence band of the GaAs QW$_s$ with the definition $\vec{\sigma}_M = \frac{1}{\sqrt{2}}(\vec{a}_1 \pm i\vec{a}_2)$, $M = \pm 1$. Circular polarization $\vec{\sigma}_M$ is equivalent to the projections on the magnetic field direction of orbital magnetic momentum $M = \pm 1$. Here $\vec{a}_1$ and $\vec{a}_2$ are the unit vectors oriented in the plane of the QW. They also determine in-plane wave vectors $\vec{k}_{\parallel} = k_x\vec{a}_1 + k_y\vec{a}_2$. The magnetoexcitons with in-plane wave vectors $\vec{k}_{\parallel}$ interact only with the cavity photons with the same in-plane wave vectors $\vec{k}_{\parallel}$. Their interaction constants are governed by the geometrical selection rules expressed by the square scalar products between two circular polarizations $\vec{\sigma}^{\pm}_k$ and $\vec{\sigma}_M$ in the form $\left|(\vec{\sigma}^{\pm}_k \cdot \vec{\sigma}^{*}_M)\right|^2$. The interaction constants are the same in the cases $\vec{\sigma}^{\pm}_{k_\uparrow}$ and $\vec{\sigma}^{\mp}_{k_\downarrow}$ and different in the cases $\vec{\sigma}^{\pm}_{k_\uparrow}$ and $\vec{\sigma}^{\pm}_{\downarrow}$, giving rise to the gyrotropy effects. The four optical-active magnetoexciton states interacting with the cavity-photon mode give rise to five polariton branches. Their dispersion laws as a function of dimensionless in-plane wave vector $x = \left|\vec{k}_{\parallel}\right| L_C / \pi$ are represented in Fig. 5 reproduced from [4]. Two forbidden magnetoexciton branches noninteracting with the cavity photons are also depicted. The total number of branches is seven.

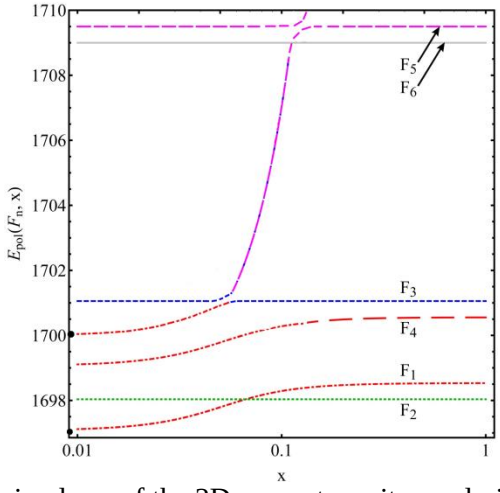

Fig. 5. Dispersion laws of the 2D magnetoexciton-polariton branches.

The Hopfield coefficients determining the amplitudes of the five polariton branches at arbitrary values of wave number x can be calculated only numerically. However, at point $x = 0$, where the cavity photons with energy E_C and with effective mass m_C interact only with one dipole-active magnetoexciton branch, the Hopfield coefficients can be determined analytically. In

addition, they make it possible to determine the effective masses on the lower and upper polariton branches at the points with $x = 0$. These points are marked by black solid circles in Fig. 5. Hopfield coefficients u^2 and v^2, which determine the photon and magnetoexciton portions, respectively, in the structure of the lower polariton branch at point $x = 0$, are plotted as a function of magnetic field strength in Fig. 6 for two different cases, namely, in the absence and presence of the RSOC, as discussed in [6]. At the same time, this figure shows effective masses m_{eff} on the lower polariton branches at point $x = 0$ at different values of external magnetic and electric field strengths. The effective polariton mass was determined by the formula

$$m_{eff}(0) = \frac{m_C}{f^{\parallel}(0)}; \; m_C = \frac{\hbar \pi n_C}{c L_C},$$

where $f^{\parallel}(x)$ is the second derivative of the lower polariton branch.

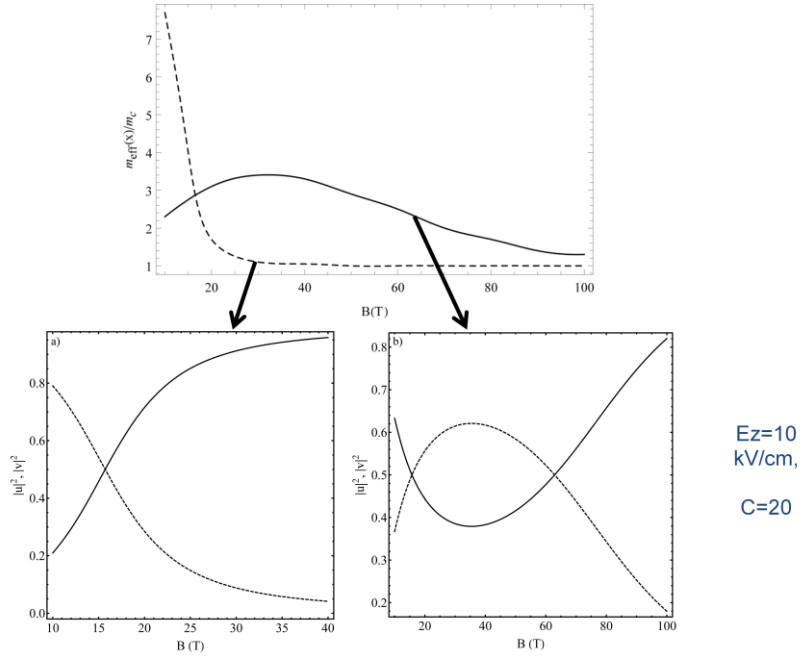

Fig. 6. Hopfield coefficients and effective polariton mass in the lower polariton branch at point $x = 0$ as a function of magnetic and electric field strengths.

In our case, the cavity photon mass is $5 \cdot 10^{-5} m_0$, where m_0 is the free electron mass. It is evident from Fig 6 that, in the absence of external electric field $E_z = 0$ and RSOC, the Hopfield coefficients and the effective polariton mass exhibit monotonic dependences on magnetic field strength *B*. It takes place because, with an increase in magnetic field strength, the detuning between the cavity photon and the magnetoexciton energies increases much greater than the exciton–photon interaction does and their reciprocal influences become nonsignificant. In the presence of an external electric field and RSOC, the changes in the magnetoexciton-cavity photon energy detuning as a function of magnetic field strength are nonmonotonic. The respective dependences of the Hopfield coefficients and the effective polariton mass are also nonmonotonic. This behavior can be seen in Fig. 6.

Now let us discuss the interaction between the magnetoexcitons with wave vectors $k_{\parallel} = 0$.

This case is important because, beginning with the pioneering paper of Lerner and Lozovik [11], it is well known that magnetoexcitons with $k_{\|} = 0$ and electrons and holes lying on the LLLs with $n_C = n_h = 0$ are forming an ideal exciton gas. It is related with the fact that the gyration points of the LQ orbits of the electrons and holes forming the magnetoexciton with $k_{\|} = 0$ do coincide and the radii of their orbits are the same. They do not depend on the electron and hole effective masses and are determined only by the magnetic length. Two of these magnetoexcitons are completely neutral, and their Coulomb interaction vanishes. Only the Coulomb e–h interactions inside the magnetoexcitons remain noncompensated and determine the magnetoexciton binding energies. This case is shown in Fig. 7; it represents the statements of [11]. The interactions between two magnetoexcitons with $k_{\|} = 0$ do appear when the polarizabilities are taken into account. The first example of this type is the effect of the ELLs. In our previous studies, virtual quantum transitions of spinless electrons and holes due to their Coulomb scattering processes were taken into account. In the first order of the perturbation theory, the quantum transmissions of the electrons and holes from their LLLs with $n_e = n_h = 0$ to the ELLs with arbitrary quantum numbers $n_e \neq 0$, $n_h \neq 0$ were engaged. In the second order of the perturbation theory, their return back to the LLLs was predicted. These two-step scattering processes between two charged particles are represented in Fig. 8 reproduced from [6]. These virtual scattering processes give rise to an overall attraction between the electrons, between the holes and between the electrons and the holes in the Hartree approximation. However, in the Fock approximation, repulsion between the spinless magnetoexcitons with $k_{\|} = 0$ does appear to stabilize their Bose–Einstein Condensation (BEC). Our previous results concerning the BEC of the magnetoexcitons with $k_{\|} = 0$ obtained in terms of the Keldysh–Kozlov–Kapaev (KKK) description were confirmed by the present calculations of the magnetoexciton–magnetoexciton interactions arising under the effect of the ELLs. The interaction constant deduced in this variant has an inversely proportional dependence on magnetic field strength. It is represented in Fig. 9 reproduced from [6]. This dependence is understandable because cross section σ of the spinless magnetoexciton–magnetoexciton interaction is proportional to the orbit area $\pi l_0^2 \approx \frac{1}{B}$.

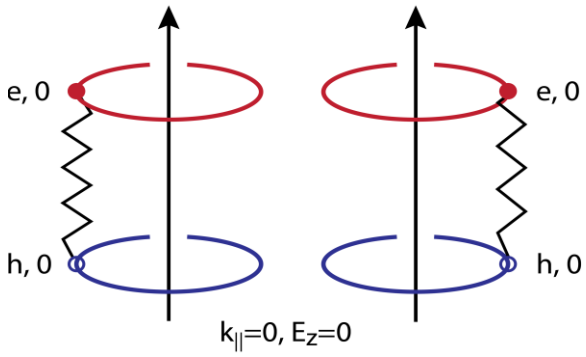

Fig. 7. The absence of interaction between two spinless magnetoexcitons with $k_{\|} = 0$ generated by electrons and holes lying on the LLLs $n_e = n_h = 0$. The case $E_z = 0$.

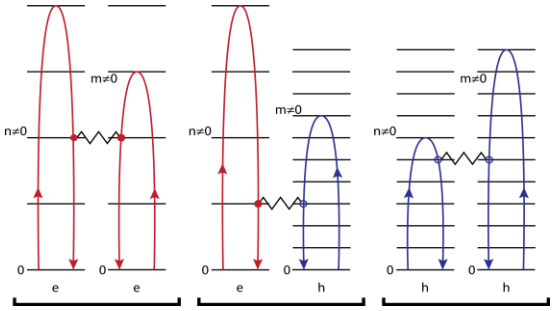

Fig. 8. Electron–electron, electron–hole, and hole–hole attractions appearing in the second order of the perturbation theory taking into account the Coulomb scattering processes between the Landau levels.

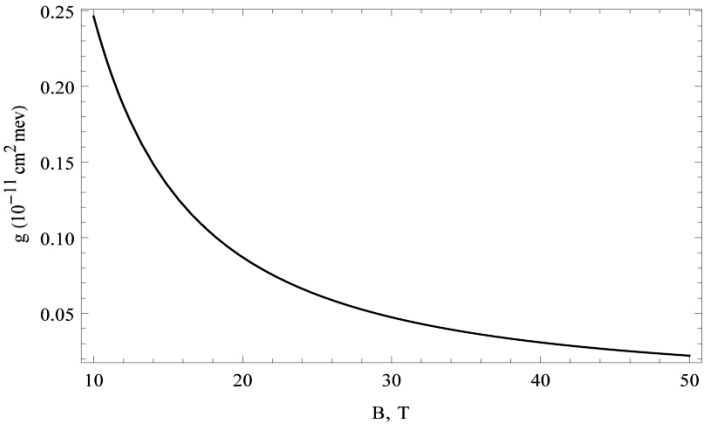

Fig. 9. Coefficient *g* describing the interaction between two spinless magnetoexcitons with $k_{\|} = 0$ taking into account the ELLs in the absence of an external electric field and RSOC.

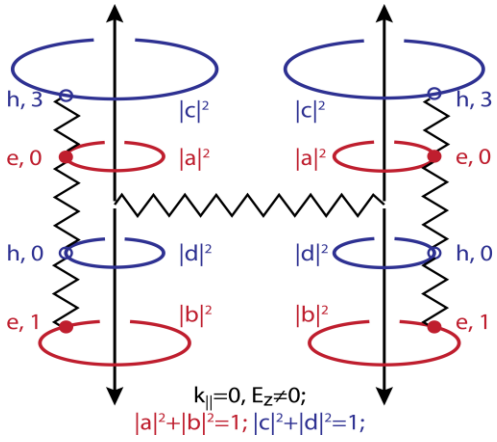

Fig. 10. Interaction between two spinor magnetoexcitons with $k_{\|} = 0$ in the presence of an external electric field $E_z \neq 0$ taking into account the RSOC as follows from [6].

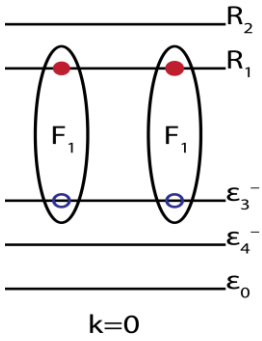

Fig. 11. Homogeneous two-magnetoexciton complex.

The creation operator and the wave function of a single magnetoexciton in state $F_i(e,x;h,y;0)$ at point $\vec{k}_{\|}=0$ are expressed as follows:

$$\hat{\psi}^{\dagger}_{ex}(F_i)=\frac{1}{\sqrt{N}}\sum_t a^{\dagger}_{x,t}b^{\dagger}_{y,-t},$$
$$\left|\hat{\psi}_{ex}(F_i)\right\rangle=\psi^{\dagger}_{ex}(F_i)\left|0\right\rangle=\frac{1}{\sqrt{N}}\sum_t a^{\dagger}_{x,t}b^{\dagger}_{y,-t}\left|0\right\rangle. \quad (1)$$

The wave function of two homogeneous magnetoexcitons with wave vector $\vec{k}_{\|}=0$ has the form

$$\phi_0(F_i,F_i)=\hat{\psi}^{\dagger}_{ex}(F_i)\hat{\psi}^{\dagger}_{ex}(F_i)\left|0\right\rangle=\frac{1}{N}\sum_{s,t}a^{\dagger}_{x,t}a^{\dagger}_{x,s}b^{\dagger}_{y,-s}b^{\dagger}_{y,-t}\left|0\right\rangle,$$
$$\left\langle\phi_0(F_i,F_i)\middle|\phi_0\middle|F_i,F_i\right\rangle=2\left(1-\frac{1}{N}\right). \quad (2)$$

The average of the Coulomb interaction Hamiltonian in the state of two homogeneous magnetoexciton complexes is as follows:

$$\frac{\left\langle\phi_0(F_i,F_i)\middle|\hat{H}_{Coul}\middle|\phi_0(F_i,F_i)\right\rangle}{\left\langle\phi_0(F_i,F_i)\middle|\phi_0(F_i,F_i)\right\rangle}=$$
$$=-2\sum_Q W(\vec{Q})S_e(e,x,Q)S_h(y,Q)-\frac{2}{N}\sum_Q W(\vec{Q})\left[S_e(x,\vec{Q})-S_h(y,\vec{Q})\right]^2= \quad (3)$$
$$=-2I_{ex}(x,y;0)-\frac{2}{N}\sum_Q W(Q)\left[S_e(x,\vec{Q})-S_h(y,\vec{Q})\right]^2.$$

The expression $[S_e(x,\vec{Q})-S_h(y,\vec{Q})]$ determines the affinity of the magnetoexciton in state $F_i=(e,x;h,y;0)$ to interact with another magnetoexciton.

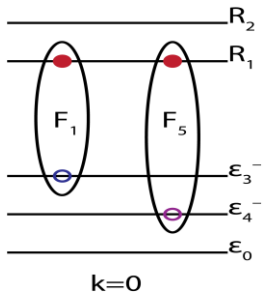

Fig. 12. Semihomogeneous two-magnetoexciton complex.

The wave function of two semihomogeneous magnetoexcitons with wave vectors $\vec{k}_{\parallel} = 0$ has the form

$$\left|\phi_0(F_1,F_5)\right\rangle = \hat{\psi}^{\dagger}_{ex}(F_1,0)\hat{\psi}^{\dagger}_{ex}(F_5,0)\left|0\right\rangle = \frac{1}{N}\sum_{t,s} a^{\dagger}_{R_1,t} a^{\dagger}_{R_1,s} b^{\dagger}_{\varepsilon_4^-,-s} b^{\dagger}_{\varepsilon_3^-,-t}\left|0\right\rangle,$$
$$\left\langle\phi_0(F_1,F_5)\middle|\phi_0(F_1,F_5)\right\rangle = \left(1-\frac{1}{N}\right). \tag{4}$$

The average of the Coulomb interaction Hamiltonian in the state of two semihomogeneous magnetoexciton complexes is as follows:

$$\frac{\left\langle\phi_0(F_1,F_5)\middle|H_{Coul}\middle|\phi_0(F_1,F_5)\right\rangle}{\left\langle\phi_0(F_1,F_5)\middle|\phi_0(F_1,F_5)\right\rangle} = -I_{ex}(F_1,0) - I_{ex}(F_5,0) -$$
$$-\frac{1}{N}\sum_{Q} W(\vec{Q})\left[S_e(R_1,Q) - S_h(\varepsilon_3^-,\vec{Q})\right]\left[S_e(R_1,\vec{Q}) - S_h(\varepsilon_4^-,\vec{Q})\right] \tag{5}$$

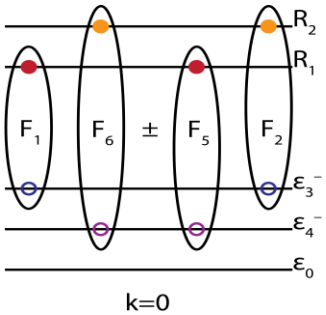

Fig. 13. Heterogeneous symmetric and asymmetric combinations.

The wave function of two heterogeneous magnetoexcitons with wave vectors $\vec{k}_{\parallel} = 0$ is as follows:

$$\left|\phi_0^{het}\right\rangle = \hat{\psi}^{\dagger}_{ex}(x,y;0)\hat{\psi}^{\dagger}_{ex}(\xi,\eta;0)\left|0\right\rangle = \frac{1}{N}\sum_{s,t} a^{\dagger}_{x,t}a^{\dagger}_{\xi,s}b^{\dagger}_{\eta,-s}b^{\dagger}_{y,-t}\left|0\right\rangle,$$

$$\left|\bar{\phi}_0^{het}\right\rangle = \hat{\psi}^{\dagger}_{ex}(x,\eta;0)\hat{\psi}^{\dagger}_{ex}(\xi,y;0)\left|0\right\rangle = \frac{1}{N}\sum_{s,t} a^{\dagger}_{x,t}a^{\dagger}_{\xi,s}b^{\dagger}_{y,-s}b^{\dagger}_{\eta,-t}\left|0\right\rangle, \quad (6)$$

$$\left\langle\phi_0^{het}\middle|\phi_0^{het}\right\rangle = \left\langle\bar{\phi}_0^{het}\middle|\bar{\phi}_0^{het}\right\rangle = 1,$$

$$\left\langle\phi_0^{het}\middle|\bar{\phi}_0^{het}\right\rangle = -\frac{1}{N}.$$

The symmetric and asymmetric states formed by two heterogeneous magnetoexcitons with wave vectors $\vec{k}_{\parallel} = 0$ are characterized by the wave functions

$$\left|\tilde{\phi}_0^{\pm}\right\rangle = \frac{1}{\sqrt{2}}\left(\left|\phi_0^{het}\right\rangle \pm \left|\bar{\phi}_0^{het}\right\rangle\right),$$

$$\left\langle\tilde{\phi}_0^{\pm}\middle|\tilde{\phi}_0^{\pm}\right\rangle = \left(1 \mp \frac{1}{N}\right), \quad \left\langle\tilde{\phi}_0^{\pm}\middle|\tilde{\phi}_0^{\mp}\right\rangle = 0, \quad \left\langle\tilde{\phi}_0^{\pm}\middle|\tilde{\phi}_0^{\pm}\right\rangle^{-1} = \left(1 \pm \frac{1}{N}\right), \quad (7)$$

The averages of the Coulomb interaction Hamiltonian in the symmetric and asymmetric states of two heterogeneous magnetoexciton complexes are as follows:

$$\frac{\left\langle\tilde{\phi}_0^{\pm}\middle|H_{Coul}\middle|\tilde{\phi}_0^{\pm}\right\rangle}{\left\langle\tilde{\phi}_0^{\pm}\middle|\tilde{\phi}_0^{\pm}\right\rangle} = \frac{1}{2}\{-I_{ex}(x,y;0) - I_{ex}(\xi,\eta;0) - I_{ex}(x,\eta;0) - I_{ex}(\xi,y;0) \mp$$

$$\mp \frac{1}{N}\sum_{Q} W(\vec{Q})\left(S(x;\vec{Q}) - S(y;\vec{Q})\right)\left(S(\xi;\vec{Q}) - S(\eta;\vec{Q})\right) \mp \quad (8)$$

$$\mp \frac{1}{N}\sum_{Q} W(\vec{Q})\left(S(x;\vec{Q}) - S(\eta;\vec{Q})\right)\left(S(\xi;\vec{Q}) - S(y;\vec{Q})\right)\}.$$

The last two terms determine the opposite sign interactions of two heterogeneous magnetoexcitons with $\vec{k}_{\parallel} = 0$ in the symmetric and asymmetric states.

Conclusions

The exact solutions of the LQ task for the 2D hhs taking into account the ZS and the RSOC with third order chirality terms and with NP dispersion law both induced by the external electric field have been derived.

Three LLLs for hhs and two LLLs for the conduction electron with first order chirality terms studied by Rashba, along with the ZS terms introduced by us, give rise to six 2D magnetoexciton states; two of them are dipole-active, two are quadrupole-active, and two are forbidden in both approximations.

The five polariton branches formed by four magnetoexciton and by one cavity-photon partners have been studied.

The interaction between 2D magnetoexcitons with wave vectors $\vec{k}_{\parallel} = 0$ has been studied

taking into account the effect of the ELLs and the external electric field applied perpendicular to the surface of the layer in the same way as the strong magnetic field. In the first case, the spinless magnetoexcitons with electrons and holes lying on their LLLs and effectuating the virtual quantum transitions to ELLs and return back due the Coulomb scattering processes have been considered. They lead to electron–electron, hole–hole, and electron–hole attractions in the second order of the perturbation theory in the Hartree approximation and to repulsion between the 2D magnetoexcitons with $k_{\|} = 0$ in the Fock approximation. Interaction constant $g(0)$ decreases in inverse proportion to increasing magnetic field strength B, $g(0) \approx 1/B$. In an external electric field, the LQ task has been effectuated taking into account the RSOC and ZS effects and the NP of the hh dispersion law. In this case, the spinor-type wave functions of the electrons and holes are characterized by the orbits essentially different from the case of the LLL with $n_e = n_h = 0$. These differences lead to the affinity of the magnetoexcitons to interact with each other. These magnetoexcitons can be referred to as spinor-type magnetoexcitons to distinguish them from the spinless case.

The interaction between two spinor-type magnetoexcitons with $k_{\|} = 0$ depends on their homogeneities and affinities. Two magnetoexcitons are referred to as homogeneous if they both are formed by electrons and holes in similar states, respectively.

There are also semihomogeneous and heterogeneous magnetoexcitons. In the first case, the electron states in two magnetoexcitons are similar; however, the hole states are different or vice versa. In the second case, both the electron and hole states in two magnetoexcitons are different. It has been shown that two homogeneous spinor-type magnetoexcitons with wave vectors $k_{\|} = 0$ attract each other if their affinity is different from zero. Two semihomogeneous spinor-type magnetoexcitons with wave vectors $k_{\|} = 0$ attract each other if their affinities have the same signs and repel each other if their affinities are of the different signs.

If the electrons are in two different states x and ξ and the holes are in other two states y and η, the heterogeneous spinor-type magnetoexcitons with $k_{\|} = 0$ can be formed in two ways, namely, in the combinations (x, y) and (ξ, η) or in alternative combinations (x, η) and (ξ, y). The wave functions of these two combinations have been used to obtain symmetric and asymmetric superposition states. It has been shown that the interactions between two heterogeneous spinor-type magnetoexcitons with $k_{\|} = 0$ forming the symmetric and asymmetric states have different signs. It is obvious that their interaction is different from zero only if the affinities of the both partners are different from zero. In these cases, the interaction constants have the dependences $g(0) \approx 1/\sqrt{B}$.

References

[1] S. A. Moskalenko, I. V. Podlesny, P. I. Khadzhi, B. V. Novikov, and A. A. Kiselyov, Solid State Commun. 151, 1690, (2011)
[2] S. A. Moskalenko, I. V. Podlesny, E. V. Dumanov, M. A. Liberman, and B. V. Novikov, Phys. Stat. Sol. B. 252, 730, (2015)
[3] S. A. Moskalenko, I. V. Podlesny, E. V. Dumanov, and M. A. Liberman, Eur. Phys. J. B 88:218, (2015)

[4] S. A. Moskalenko, I. V. Podlesny, E. V. Dumanov, M. A. Liberman, and B. V. Novikov, J. Nanophoton. 10(3), 036006, (2016)
[5] S. A. Moskalenko, I. V. Podlesny, M. A. Lberman, and B. V. Novikov. J. Nanophoton 6, 061806, (2012)
[6] E. V. Dumanov, I. V. Podlesny, S. A. Moskalenko, and M. A. Liberman, Physica E (in press)
[7] S. A. Moskalenko, E. V. Dumanov, I. V. Podlesny, M. A. Liberman, B. V. Novikov, S. S. Rusu, and V. M. Bajireanu, Mold. J. Phys. Sci. 13(1–2), 61, (2014)
[8] E. I. Rashba, Fiz. Tverd. Tela (Leningrad) 2, 1224 (1960) [Sov. Phys. Solid State 2, 1109, (I960)]
[9] J. J. Hopfield, Phys. Rev. 112, 1555 (1958)
[10] R. Winkler, Spin-Orbit Coupling Effects in Two-Dimensional Electron and Hole Systems, in *Tracts in Modern Physics* (Springer, Berlin, 2003) vol. 191.
[11] I. V. Lerner and Yu. E. Lozovik, Zh. Eksp. Teor. Fiz. 80, 1488 (1981); Sov. Phys-JETP 53, 763, (1981)
[12] D. Paquet, T. M. Rice, and K. Ueda, Phys. Rev. B 32, 5208, (1985)

SUPERCONDUCTING TRANSITION TEMPERATURE AND HEAT CAPACITY JUMP IN QUASI-TWO-DIMENSIONAL ANISOTROPIC SYSTEMS DOPED WITH CHARGE CARRIERS

M. E. Palistrant and V. A. Ursu

Institute of Applied Physics, Academy of Science of Moldova
Email: mepalistrant@yandex.ru

(Received August 3, 2016)

Abstract

Phase transitions in quasi-two-dimensional systems doped with atoms with different valences, at various temperatures are investigated. The transitions into the magnetic state of spin density wave which appear due to the nesting on the Fermi surface and the transition into incommensurable state of spin density wave are considered along with the appearnce of superconductivity. The main system of equation is presented, the difference of free energies in different phases, superconducting transition temperature and heat capacity jump are calculated. The behavior of mentioned quantities as a function of temperature and charge carrier density is researched.

1. Introduction

The description of the properties of FeAs based high-Tc superconducting systems (Fe – pnictids and Fe - chalcogenids) requires taking into account the following peculiarities of these systems: the overlapping on the Fermi surface of few energy bands (both electron- and hole-type bands); reduced dimensionality of the system and the anisotropy of dispersion law for the energy of electrons and holes of different bands; the existence of symmetry points where the following relation takes place:

$$\varepsilon_n(\vec{k}) = -\varepsilon_n(\vec{k} + \vec{Q}) \tag{1}$$

(ε_n is the energy of charge in *n-th* band, $\vec{Q}$ is the wave vector of spin density wave); phase transitions into magnetic (SDW) and superconducting (SC) when temperature and charge carrier density vary; the bands filling degree when doping.

An important number of articles, monographs and reviews are dedicated to the theory of many-band superconductors (see the references given in [1] – [4]). These researches have been started long before the discovery of HTSC and are based on the model independently developed by Moscalenco [5] and Suhl et al. [6]. Presently, along with the term "many-band" for modern HTSC compounds the term "many-orbital superconductivity" is used. In our opinion, this fact is determined by presence of several energy bands (both electron– and hole – type) on the Fermi surface. In this case, the two – or many – band model [5, 6] is developed and adjusted to the concrete HTSC compound, according to experimental data. For example, a review of modern researches on FeAs – based modern compounds is given in [7] (see also the references in [4]).

An important problem when the physical properties of above mentioned systems are

researched is the identification of mechanisms leading to the appearance of magnetism (SDW state) and superconductivity (SC) and the coexistence of these states. One of such mechanisms is the transition of the system into gapless magnetic state (phase transition commensurability – incommensurability) when the wave vector of spin density wave is $Q \neq 2\ k_F$. Some partial researches in this direction are performed in [4, 8].

Here, in this paper these researches are developed further: free energy in the phase of coexistence of SDW and SC is calculated, the type of phase transition (first or second kind) is determined when superconductivity appears on the background of SDW, the temperature of superconducting transition T_c and heat capacity jump in the point $T = T_c$ are calculated. Also, the behavior of above mentioned thermodynamic quantities as functions of temperature and charge carrier density is analyzed.

2. The Hamiltonian of the system and basic equations

We think that a quality correlation between superconductivity and magnetism is possible to obtain using the following Hamiltonian:

$$H = \sum_{\vec{k},\sigma}\left(\varepsilon\left(\vec{k}\right)-\mu\right)a^{+}_{\vec{k}\sigma}\,a_{\vec{k}\sigma} - \sum_{\vec{k}\vec{k}'} \mathrm{V}\left(\vec{k}\vec{k}'\right)a^{+}_{\vec{k}\uparrow}a^{+}_{-\vec{k}\downarrow}\;\; a_{-\vec{k}'\downarrow}a_{\vec{k}'\uparrow} + \\ + \sum_{\vec{k}\vec{k}\vec{q}} I\left(\vec{k}\vec{k}'\right)\, a^{+}_{\vec{k}\uparrow}a_{\vec{k}+\vec{q}\uparrow}a^{+}_{\vec{k}'\downarrow}a_{\vec{k}'-\vec{q}\downarrow}. \qquad (2)$$

Here V and I – effective constants of superconducting and magnetic interaction of electrons, $\vec{k}$ – quasi - momentum, $\varepsilon\left(\vec{k}\right)$ – energy of electron, σ – spin of electron, which takes the values $\uparrow$ and $\downarrow$, $a^{+}_{\vec{k}\sigma}, a_{\vec{k}\sigma}$- operators of appearance or annihilation of electrons (with momentum $\vec{k}$ and spin σ), $\vec{q}$ corresponds to those values of electron momentum which lead to the nesting condition (1), μ is chemical potential.

Within such approach the ratio between parameters V and I or the superconducting transition temperature T_c and magnetic transition temperature T_M is important. The second term in this expression contains $V > 0$ and describes the formation of Cooper pairs, the third one describes the appearance of SDW at $I > 0$. We consider a non-phonon mechanism of superconductivity based on direct repulsion of electrons. The non-phonon mechanism which leads to the values $V > 0$ in Hamiltonian (2) isn't clearly determined. According to many researchers, superconductivity in FeAs-based compounds appears due to spin fluctuations, i.e. magnetic mechanism [7]. But strong magnetic fluctuations which are able to lead to the formation of Cooper pairs aren't discovered in all these compounds. In the same time, all of them are many-band systems. Therefore, the appearance of additional electron-electron inter- and intra-band interactions V_{nm} ($n; m = 1, 2$ in the case of two-band system), which contribute to the efficiency of system transition into superconducting state, is inherent for such systems. In particular, when inter-band constants of electron interaction are higher than intra-band ones ($V_{11}V_{22} - V_{21}V_{12} < 0$) within a non-phonon mechanism high values of Tc are possible when two-band system is doped with charge carriers [9, 4]. In our opinion, such an electronic mechanism of superconductivity could be named inter-band mechanism.

Using the Green functions method [10], in middle – field approximation, we obtain from (2) a self-consistent system of equations for determining the order parameter of SC (Δ), order parameter of SDW (M), and chemical potential μ (see, for details [8, 11]):

$$\frac{1}{V} = \frac{1}{4}\int_{-\widetilde{W}}^{\widetilde{W}} d\varepsilon N(\varepsilon)\sum_{\alpha,\beta}\Phi_1\left(\varepsilon,\mu_{\beta}^{\alpha},\mathrm{M},\Delta\right),$$

$$\frac{1}{I} = \frac{1}{4}\int_{-\widetilde{W}}^{\widetilde{W}} d\varepsilon N(\varepsilon)\sum_{\alpha,\beta}\Phi_2\left(\varepsilon,\mu_{\alpha\beta},\mathrm{M},\Delta\right),$$

$$x = \int_{-\widetilde{W}}^{\widetilde{W}} d\varepsilon N(\varepsilon)\sum_{\alpha\beta}\Phi_3(\varepsilon,\mu_{\alpha\beta},M,\Delta), \tag{3}$$

here $N(\varepsilon)$ – electron state density for quasi-two-dimensional anisotropic system with cosines-type dispersion law:

$$\varepsilon\left(\vec{k}\right) = -W_1 cosk_x a - W_2 cosk_y b, \tag{4}$$

$$\Phi_1\left(\varepsilon,\mu_{\alpha\beta},M,\Delta\right) = \frac{M^2+Y}{Y}\cdot\frac{th\frac{\sqrt{X_1}}{2T}}{\sqrt{X_1}} - \frac{M^2-Y}{Y}\cdot\frac{th\frac{\sqrt{X_2}}{2T}}{\sqrt{X_2}},$$

$$\Phi_2\left(\varepsilon,\mu_{\alpha\beta},M,\Delta\right) = \frac{\Delta^2+\left(\mu_{\alpha\beta}\right)^2+Y}{Y}\cdot\frac{\mathrm{th}\frac{\sqrt{\mathrm{X}_1}}{2\mathrm{T}}}{\sqrt{\mathrm{X}_1}} - \frac{\Delta^2+\left(\mu_{\alpha\beta}\right)^2-Y}{Y}\cdot\frac{th\frac{\sqrt{X_2}}{2T}}{\sqrt{X_2}},$$

$$\Phi_3\left(\varepsilon,\mu_{\alpha\beta},M,\Delta\right) = \frac{\Delta^2+\left(\mu_{\alpha\beta}\right)^2+\varepsilon^2+Y}{Y}\cdot\frac{th\frac{\sqrt{X_1}}{2T}}{\sqrt{X_1}} - \frac{\Delta^2+\left(\mu_{\alpha\beta}\right)^2+\varepsilon^2-Y}{Y}\cdot\frac{th\frac{\sqrt{X_2}}{2T}}{\sqrt{X_2}}, \tag{5}$$

$$X_{1,2} = \varepsilon^2 + \left(\mu_{\alpha\beta}\right)^2 + \mathrm{M}^2 + \Delta^2 \pm 2Y, \qquad Y = \sqrt{\left(\mu_{\alpha\beta}\right)^2\left(\varepsilon^2+M^2\right)+M^2\Delta^2},$$

where

$$\mu_{\alpha\beta} = \mu + \alpha\eta_a + \beta\eta_b;\ \eta_a = \frac{W_1 a q_x}{2};\ \eta_b = \frac{W_2 b q_y}{2};\ \alpha,\beta = \pm 1 \tag{6}$$

η_a, η_b are the constants of the incommensurability parameter of SDW, q_x, q_y – components of the deviation of SDW vector from *2 k_F*.

The expressions (4) – (5) are given in final form after series of transformation of main equations. In particular, summation over Matsubara frequency is performed and transition to the integration over energy taking into account the umklapp - processes leading to the relation $Q \neq 2\ k_F$ is made (for details, see [8, 11, 12]).

The properties of the system in SDW state ($\Delta = 0$, $M \neq 0$) are researched in details in our series of works [4, 11, 12]. Here, we will consider the possibility of coexistence of magnetism and superconductivity ($\Delta \neq 0$, $M \neq 0$) in quasi-two-dimensional doped anisotropic system. In order to reveal the efficiency of such coexistence, the difference of free energies $F(\Delta, M) - F\ (0, M)$ has to be researched as a function of temperature and charge carrier density along with self-consistent solution of system of equations (3).

3. Calculation of free energy and heat capacity jump at $T = T_c$

In order to determine the free energy we use the identity:

$$F\ (\Delta, M) - \ F\ (0,0) = \ \int_0^{\Delta} \Delta'^2\ d\Delta' \frac{d}{d\Delta'} \left(\frac{1}{V}\right) + \ \int_0^{M} M'^2 dM' \ \frac{d}{dM'} \left(\frac{1}{I}\right)_{V\ =\ 0}. \tag{7}$$

Integrating by parts, we will bring it to the form:

$$F\ (\Delta, M) - \ F(0,0) = \ \frac{\Delta^2}{V} + \ \frac{M^2}{I} - \ 2 \int_0^{\Delta} \Delta' d\Delta' \ \frac{1}{V} - \ 2 \ \int_0^{M} M' dM' \ \left(\frac{1}{I}\right)_{V=0} \tag{8}$$

Using expressions (3) and integrating over order parameters Δ' and M', we bring the difference of free energies to the form:

$$F(\Delta, M) - \ F\ (0,0) = \ \frac{\Delta^2}{V} + \ \frac{M^2}{I} - \ T \ \int_{-\widetilde{W}}^{\widetilde{W}} N\ (\varepsilon)\ d\varepsilon \ \sum_{\alpha\beta}$$

$$\left\{ \ln ch\ \frac{\sqrt{X_1}}{2T} + \ln ch \frac{\sqrt{X_2}}{2T} - \ \ln ch \frac{\sqrt{X_1^{00}}}{2T} - \ln ch\ \frac{\sqrt{X_2^{00}}}{2T} \right\}, \tag{9}$$

where X_1 and X_2 are determined by formulas (4), and $X_{1,2}^{00} = X_{1,2}\ |_{M=\Delta=0}$. As it follows from the results obtained earlier [8], in this examined system superconducting state appears on the background of magnetic ordering. Thus, it makes sense to consider the difference of free energies in the form:

$$\delta\ F = F\ (\Delta, M) - \ F\ (0, M) = \ \frac{\Delta^2}{V} - \ T \sum_{\alpha\beta} \int_{-\widetilde{W}}^{\widetilde{W}} N\ (\varepsilon) d\varepsilon \ \cdot$$

$$\sum_{\alpha\beta} \left\{ \frac{\ln ch\ \sqrt{X_1}}{2T} + \ln ch \frac{\sqrt{X_2}}{2T} - \ln ch \frac{\sqrt{X_1^o}}{2T} - \ln ch \frac{\sqrt{X_2^o}}{2T} \right\},$$

$$X_1^o = X_1|_{\Delta=0}\ , \quad X_2^o = \ X_2|_{\Delta=0}. \tag{10}$$

Further we examine the temperature range close to superconducting transition temperature ($T \sim T_c$). We expand the difference of free energies (10) over small parameter Δ^2

$$\delta\ F = F\ (\Delta, M) - \ F\ (0, M) = \ \frac{\Delta^4}{4} [-f_1 + \Delta^2 f_2 + \ \ldots], \tag{11}$$

and represent the equation for superconducting transition temperature (3) in the form:

$$\frac{1}{V} = f_o - \ \frac{1}{2}\ f_1\ \Delta^2 + \ \frac{3}{8}\ \Delta^4\ f_2 + \ \ldots, \tag{12}$$

where

$$f_0 = \ \frac{1}{2} \int_0^{\widetilde{W}} d\varepsilon\ N\ (\varepsilon) \ \sum_{\alpha\beta} \Phi_1\ \left(\varepsilon, \mu_\beta^\alpha, M\ \Delta\right)|_{\Delta\ =0}$$

$$= \ \frac{1}{2} \int_0^{\widetilde{W}} d\varepsilon\ N\ (\varepsilon) \ \sum_{\alpha\beta} \left[\frac{M^2 + \ Y}{Y} \cdot \frac{th \frac{\sqrt{X_1}}{2T}}{\sqrt{X_1}} - \frac{M^2 - Y}{Y} \cdot \frac{th \frac{\sqrt{X_2}}{2T}}{\sqrt{X_2}} \right],$$

$$f_1 = \ - \int_0^{\widetilde{W}} d\varepsilon\ N\ (\varepsilon) \ \sum_{\alpha\beta} \frac{\partial}{\partial \Delta^2} \Phi_1\ \left(\varepsilon, \mu_\beta^\alpha, M, \Delta\right)|_{\Delta\ =0} =$$

$$= - \int_0^{\widetilde{W}} d\varepsilon N(\varepsilon) \sum_{\alpha,\beta,j} \left\{ \frac{1}{4T_c ch^2 \left(\frac{1}{2T} \sqrt{z_2 + 2jz_1}\right)} \times \right.$$

$$\times\left(\frac{1}{\sqrt{z_2+2jz_1}}+\frac{jM^2}{\sqrt{{z_1}^2z_2+2j{z_1}^3}}\right)\left(\frac{M^2}{\sqrt{{z_1}^2z_2+2j{z_1}^3}}+\frac{j}{\sqrt{z_2+2jz_1}}\right)-$$
$$-\frac{M^2th\left(\frac{1}{2T}\sqrt{z_2+2jz_1}\right)}{2}\cdot\left[\frac{1}{({z_1}^2b+2j{z_1}^3)^{3/2}}\cdot(3jz_1M^2+{z_1}^2+z_2M^2)+\frac{j}{z_2+2jz_1}\times\right.$$
$$\left.\times\left(\frac{1}{M^2\sqrt{z_2+2jz_1}}+\frac{j}{\sqrt{{z_1}^2z_2+2j{z_1}^3}}\right)\right],$$

Where

$$z_1=\mu_{\alpha\beta}\sqrt{\varepsilon^2+M^2},$$
$$z_2=\varepsilon^2+\left(\mu_{\alpha\beta}\right)^2+M^2,\qquad j=\pm1.$$
$$f_2=\frac{2}{3}\int_0^{\widetilde{W}}d\varepsilon\,N(\varepsilon)\sum_{\alpha\beta}\frac{\partial^2}{\partial\Delta^4}\Phi_1\left(\varepsilon,\mu_\beta^\alpha,M,\Delta\right)\Big|_{\Delta=0}. \tag{13}$$

From expression (11) follows that there are two possibilities of transition of magnetic system into superconducting state: 1) $\Delta = 0$ and 2) $\Delta^2 = f_1/f_2$. The first case corresponds to second-kind phase transition (at $f_1 > 0, f_2 < 0$), and the second case – to first-kind phase transition (at $f_1 < 0$, $f_2 < 0$). Here is crucial the sign of the coefficient f_1, depending on x and M. The point $f_1 = 0$ corresponds to the value $x = x_c$, when the type of phase transition is changing. The critical temperature is not a monotonic decreasing function of x. There is a range of ambiguous compliance between x and T_c. It an area of instability of normal state relative to the formation of Cooper pairs. Obviously, at $x > x_c$ the equation (12) has to be examined at $\Delta \neq 0$, which corresponds to first-kind phase transition. In particular, unambiguous dependence of T_c on x can be represented graphically, after calculating based on (10) the difference in free energy at low temperatures and determining x from the condition $\delta F = 0$ at $T=T_c = 0$.

Further, expanding over the quantity $(1 - \mathrm{T}/\mathrm{T}_c)$ in eq. (13) and considering only quadratic terms over the quantity Δ^2, it is easy to find the expression for order parameter:

$$\Delta^2=\frac{2}{f_1}\left(1-\frac{T}{T_c}\right)T_c\left.\frac{\delta f_0}{\delta T}\right|_{\mathrm{T=Tc}}. \tag{14}$$

Replacing (14) in (11), for free energy we obtain:

$$\delta F=-\frac{1}{f_1}\left(1-\frac{T}{T_c}\right)^2\left(\left.\frac{\delta f_0}{\delta T}\right|_{\mathrm{T=Tc}}\right)^2. \tag{15}$$

Therefore, based on (15), for specific heat jump in the point $T=T_c$ we obtain the expression:

$$\delta\mathrm{C}=C(\Delta,M)-C(0,M)=-T\frac{\delta^2}{\delta T}\delta F=\frac{2}{f_1}T_c\left(\left.\frac{\delta f_0}{\delta T}\right|_{\mathrm{T=Tc}}\right)^2. \tag{16}$$

4. Phase transitions

The system of equations (3) – (5) contains the possibility for describing various phase transitions in examined system when temperature T and charge carrier density x change. This system contains parameter of magnetic ordering M, superconducting order parameter Δ, chemical potential μ, and also the components of incommensurability of magnetic state η_a and η_b.

As it was shown earlier [8, 4], superconductivity in examined system appears at $\mathrm{T_м} > \mathrm{T_c}$ on the background of incommensurable state of SDW. This fact corresponds to the necessity of examining the system (3) in two cases: 1) $\mathrm{M} \neq 0$, $\Delta = 0$ and 2) $\mathrm{M} \neq 0$, $\Delta \neq 0$. When the temperature of superconducting transition T_c is calculated is sufficient to examine the limiting cases $\mathrm{M} \neq 0$, $\Delta \to 0$.

In the case 1) we have a system of equations, describing SDW state in the absence of superconductivity, and in the case 2) this system contains the definition of quantities T_c, $M(T_c)$, μ, and also the values of η_a and η_b.

The obtained above main equations are a complex system and its solving may be performed numerically.

For the case 1), which corresponds to SDW state, we examine the system of equations:

$$\frac{1}{V} = \frac{1}{2}\int_0^{\tilde{W}} \frac{N(\varepsilon)d\varepsilon}{\sqrt{\varepsilon^2 + M^2}} \sum_{\alpha\beta j} \frac{\left[M^2 + j\mu_{\alpha\beta}\sqrt{\varepsilon^2 + M^2}\right] th\frac{1}{2T}\left(\sqrt{\varepsilon^2 + M^2} + j\mu_{\alpha\beta}\right)}{j\mu_{\alpha\beta}\left[\sqrt{\varepsilon^2 + M^2} + j\mu_{\alpha\beta}\right]},$$

$$\frac{1}{I} = \frac{1}{2}\int_0^{\tilde{W}} \sum_{\alpha\beta j} \frac{N(\varepsilon)d\varepsilon}{\sqrt{\varepsilon^2 + M^2}} th\frac{1}{2T}\left(\sqrt{\varepsilon^2 + M^2} + j\mu_{\alpha\beta}\right), \qquad (17)$$

$$x = \int_0^{\tilde{W}} \sum_{\alpha\beta j} \frac{N(\varepsilon)d\varepsilon}{\sqrt{\varepsilon^2 + M^2}} \frac{\left[\varepsilon^2 + \mu_{\alpha\beta}^2 + j\mu_{\alpha\beta}\sqrt{\varepsilon^2 + M^2}\right] th\frac{1}{2T}\left(\sqrt{\varepsilon^2 + M^2} + j\mu_{\alpha\beta}\right)}{j\mu_{\alpha\beta}\left[\sqrt{\varepsilon^2 + M^2} + j\mu_{\alpha\beta}\right]},$$

together with two additional equations that allow to determine the dependence of quantities η_a and η_b from T and x:

$$\frac{\delta}{\delta\eta_a}[F(M) - F(0)] = \sum_{\alpha\beta j} j\alpha \int_0^{\tilde{W}} N(\varepsilon)d\varepsilon \left[th\frac{1}{2T}\left(\sqrt{\varepsilon^2 + M^2} + j\mu_{\alpha\beta}\right) - th\frac{1}{2T}\left(\varepsilon + j\mu_{\alpha\beta}\right)\right] = 0$$

$$\frac{\delta}{\delta\eta_b}[F(M) - F(0)] = \sum_{\alpha\beta j} j\beta \int_0^{\tilde{W}} N(\varepsilon) \times$$

$$\times d\varepsilon \left[th\frac{1}{2T}\left(\sqrt{\varepsilon^2 + M^2} + j\mu_{\alpha\beta}\right) - th\frac{1}{2T}\left(\varepsilon + j\mu_{\alpha\beta}\right)\right] = 0, \qquad (18)$$

where $F(M) - F(0)$ is the difference of free energies.

In Fig. 1 the phase diagram (T, $\tilde{x}$) is shown as a result of the analysis of the solutions of these equations and determination of dependence of parameters η_a, η_b on temperature and impurity concentration [8, 11].

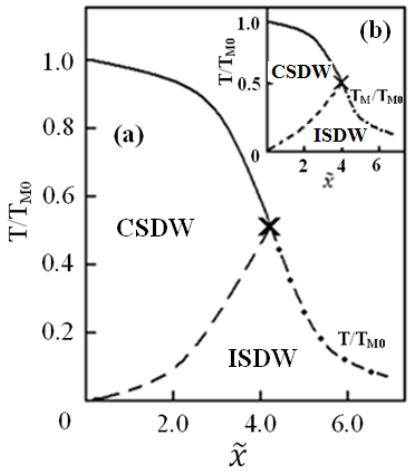

Fig. 1. Phase diagram (T, x̃). *CSDW* – commensurable, and *ISDW* – incommensurable spin density wave (a) case of isotropic energy spectrum (W_2 / W_1=*1*), (b) – case of anisotropic energy spectrum (W_2 / W_1=*1.3*). In the branching point marked with a cross, we have: case (a) T_M/T_{M0} = *0.49*, case (b) T_M/T_{M0} = *0.52*.

The dashed curve in the phase diagram of Fig. 1 separates incommensurable SDW (ISDW) state (low temperatures range) from commensurable one (high temperatures range). The comparison of two diagrams in Fig.1 (a and b) demonstrates the influence of the anisotropy of energy spectrum on phase diagram (T, $\tilde{x}$). It follows that the anisotropy of energy spectrum increases the area of ISDW (shifts the dashed curve to the area of higher temperatures). It is chosen: (1a) – isotropic case ($W_1 = W_2$); (1b) – anisotropic case $W_2/W_1=1.3$. Thus, both in isotropic and anisotropic case, the magnetic state of spin density wave splits into commensurable and incommensurable one.

As a result the dielectric gap shifts relative to the Fermi surface (q_x,; $q_y \neq 0$) and, therefore, free carriers appear on the Fermi surface. In such a way, the examined here mechanism (violation of nesting and shifting of dielectric gap) may lead to the transition of the system to gapless magnetic state and to the possibility of appearance of superconductivity.

The limiting case $M \neq 0$, $\Delta \to 0$, $T = T_c$ leads to the system of eq. (17), where we have to consider $T = T_c$. The obtained in this way system demonstrates the appearance of superconductivity in the magnetic phase, i.e. determines the coexistence of magnetism and superconductivity.

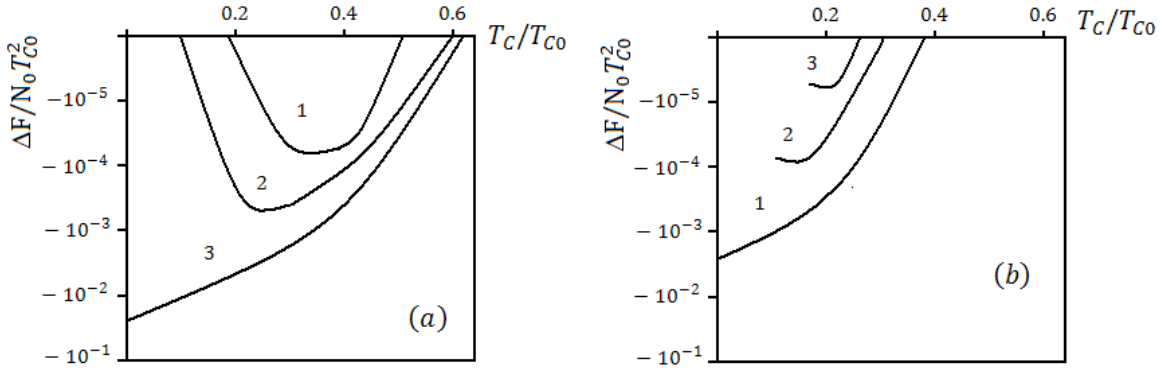

Fig. 2. Temperature dependence of free energy difference at various values of parameters $\tilde{x}$ *and t.* Case (a) curve 1 corresponds to $\tilde{x} = 3.6$ and *t=0.8*, curve 2 – to $\tilde{x} = 4.2$ and *t=0.6*, curve 3 – to $\tilde{x} = 4.6$ and *t=0.4*. Case (b) curve 1 corresponds to $\tilde{x} = 6$ and *t=0.3*, curve 2 – to $\tilde{x} = 4$ and *t=0.2*, curve 3 - $\tilde{x} = 2$ and *t=0.1*.

The quantities $t = T_{c0}/T_{м0}$, $\tilde{x} = x/2N_0$ and T are important theory parameters. Here T_{c0} and $T_{м0}$ are renormalized temperatures of superconducting and magnetic transitions.

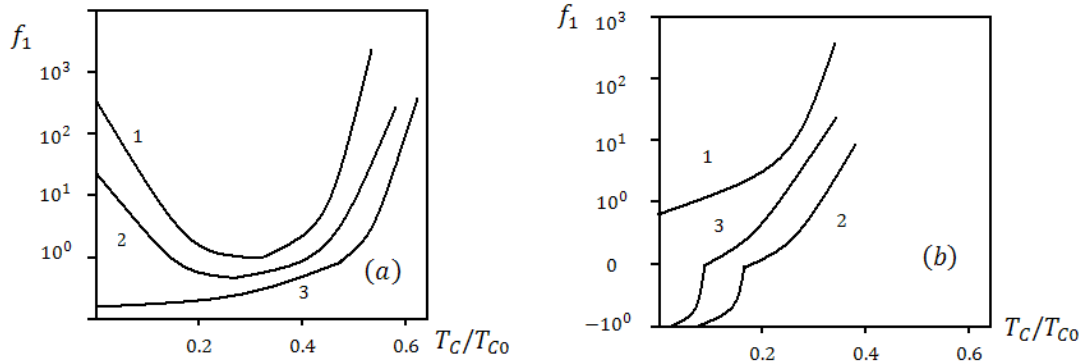

Fig. 3. The dependence of coefficient f_1 on critical temperature of superconducting transition. The curves are marked similarly to Fig. 2. The values of parameters $\tilde{x}$ and t is similar to Fig. 2.

In Fig. 2 the temperature dependence of free energy difference at various values of t and $\tilde{x}$ parameters is shown. From these results follows that in a wide range of temperatures the difference of free energies has a negative value, which speaks that the appearance of superconductivity on the background of incommensurable SDW state is profitable. Wherein second – order phase transitions are possible in low temperatures range (Fig. 2a, curves 1-3) and first – order ones in low temperatures range (Fig. 2b, curves 2 and 3). The same result we obtain when the function $f_1(T)$ from (13) is studied (Fig. 3). The type of phase transition is determined by the ratio between quantities T_{C0} and T_{M0}. We have a second – order phase transition to superconducting state (Fig. 3a) where $f_1 > 0$ in the whole range of examined values of T_c and first – order one $f_1 < 0$ (Fig 3b, curves 2 and 3).

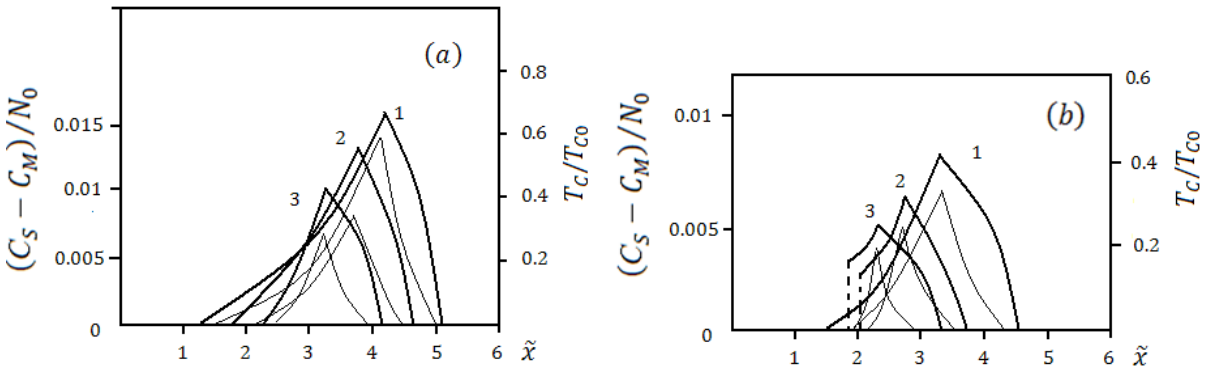

Fig. 4. The dependence of temperature of superconducting transition (bold curves) and $\frac{C_S - C_M}{N_0}$ on charge carrier density. Case (a) curve 1 corresponds to *t=0.8*, curve 2 – to *t=0.6*, curve 3 – to *t=0.4*. Case (b) curve 1 corresponds to *t=0.3*, curve 2 - *t=0.2*, curve 3 - *t=0.1*.

The dependence on charge carrier density of two quantities T_c/T_{c0} (bold curves 1-3) and $\delta C/N_0 = \big(C(\Delta, M) - C(0, M)\big)/N_0$ (thin curves 1-3) is presented in Fig. 4 a, b. As it follows from this figure the quantities T_c/T_{c0} and $\delta C/N_0$ reach the maximum at nearly the same values of carrier density $\tilde{x}_{max}$. Superconducting state occurs at doping in the point $\tilde{x} = \tilde{x}_{c1}$, reaches the maximum value in the point $\tilde{x} = \tilde{x}_{max}$ and vanish at the point $\tilde{x} = \tilde{x}_{c2}$. The behavior of T_c/T_{c0} is presented in the form of deformed bell-shaped curve. The absence of symmetry in this dependence on carrier density is explained by the influence of magnetic state on superconductivity. Indeed, the definition of T_c contains the magnetic order parameter $M(T_c)$, which suppresses superconductivity. The value of this quantity in the area $\tilde{x} < \tilde{x}_{max}$ is bigger than in the area $\tilde{x} > \tilde{x}_{max}$, that is manifested in the form of dependence T_c/T_{c0} on $\tilde{x}$.

In these figures the curves for the specific heat are lesser deformed than the curves for T_c, due to the presence of additional factors in the definition of δC in (16).

The concrete values of theory parameters t and $\tilde{x}$ are given in figures captions. An example of experimental results related to FeAs – based HTSC compounds is given in Fig. 5. The comparison of our curves given in Fig. 4 with experimental ones from Fig. 5 suggests that qualitative dependence of T_c on $\tilde{x}$ is in agreement with experimental data [13].

In the case of heat capacity jump qualitative agreement may be obtained if it assumed that there is a peak in the dependence of electron state density N_0 on $\tilde{x}$ similar to the dependence $T_c(\tilde{x})$. The presented theory doesn't contain other possibilities. It is natural that the examined

description of coexistence of magnetism and superconductivity based on a simple model (1) isn't enough for obtaining complete agreement with experimental data related to complex FeAs-based compounds.

Perhaps, it may be necessary to take into account the overlapping of energy bands on the Fermi surface, additional electron – electron interactions, associated with consideration of charge and spin fluctuations etc. Reasoning on this subject can be found in experimental studies (see, for instance [13]).

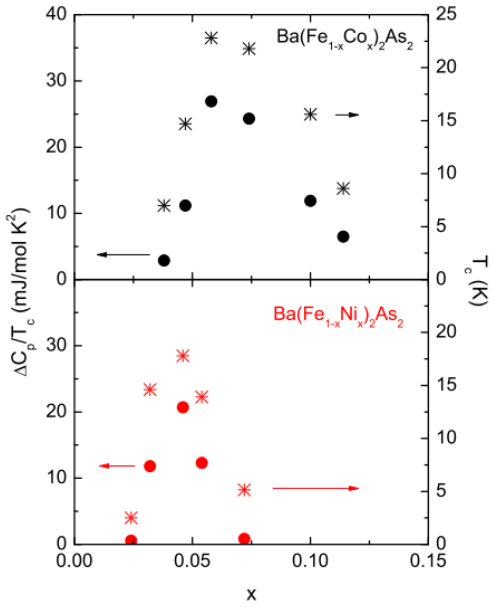

Fig. 5. $\Delta C_p/T_c$ (little circles, left axis) and T_c (asterisks, right axis) as functions on impurity concentration x, $Ba(Fe_{1-x}Co_x)_2As_2$ (the upper part) and $Ba(Fe_{1-x}Ni_x)_2As_2$ (the bottom part).
The graph corresponds to Fig. 2 in [13] here $\Delta C_p = C_S - C_M$.

5. Conclusions

This paper is focused on the identification of various phase transitions in quasi-two-dimensional lattice with a cosine – type electron energy dispersion law and the presence in the system of interactions responsible for magnetic phase (SDW) and superconductivity.

Chemical doping with impurity leads to the violation of nesting on Fermi surface and instability of SDW state. In this case, the taking into account of umklapp - processes changes the value of wave vector of spin density wave. At $Q \neq 2\ k_F$ the dielectric gap shifts relative to Fermi surface. As a result, the system passes into stable gapless magnetic state (incommensurable SDW state). Free carriers appear on Fermi surface and possibility for superconductivity is opened. Thus, we may conclude:

1. When quasi-two-dimensional system is doped with impurity with increasing of charge carrier concentration $\tilde{x}$ successive phase transitions commensurable state of spin density wave (CSDW) - incommensurable state of spin density wave (ISDW).
2. On the background of ISDW formation of Cooper pairs and coexistence of magnetic and superconducting states are possible when $T_c < T_M$. If $T_c > T_M$ superconductivity doesn't appear.
3. The area where superconductivity and magnetism coexist is determined mainly by the value of the parameter $t = T_{C0}/T_{M0}$.

4. The dependence of T_c/T_{c0} on impurity concentration $\tilde{x}$ is presented in the form of deformed bell-shaped curve. Superconductivity appears in the point $\tilde{x}_{c1}$, reaches the maximum in the point $\tilde{x}_{max}$, and vanishes at $\tilde{x}_{c2}$. The type of phase transition determines the value of parameter *t*. In the area of low temperatures and small $\tilde{x}$ the phase transition is first-order one. Qualitative agreement with experimental data for a number of *FeAs*-based compounds.
5. Heat capacity jump $\delta C = C(\Delta, M) - C(0, M)$ as a function of $\tilde{x}$ has the same bell-shape but is less deformed then in the case of T_c/T_{c0} due to an additional factor in the definition of this value.

Acknowledgments. The research was supported by project 15.817.02.08F "Statistical, Kinetic, and Quantum Methods for Studying Many-Body Systems. Application to the Condensed State" and developed at the Institute of Applied Physics of the Academy of Sciences of Moldova.

References

[1] V. A. Moskalenko, M. E. Palistrant, and V. M. Vakalyuk, Usp. Fiz. Nauk 161, 155, (1991) [Sov. Phys. Usp. 34, 717, (1991)]; Solid State Commun. 69, 747 (1989); cond-mat/03099671.
[2] M. E. Palistrant, Condens. Matter Phys. 12, 1, 677, (2009).
[3] M. E. Palistrant and L.Z. Kon, Ukr. J. Phys. 55, 44, (2010).
[4] M. E. Palistrant, J. Exp. Theor. Phys. 150, 1(7), 97, (2016).
[5] V. A. Moscalenko, Fiz. Met. Mettaloved; 8, 503, (1959); [in English] Phys. Met. Metalogr. 8, 25, (1959).
[6] H. Suhl, B.T. Matthias, and L.R. Walker, Phys. Rev. Lett. 3, 552 (1959).
[7] A. V. Chubukov. and P.J. Hirschfield, Phys. Today 68, 46 (2015); arXiv: 1412.7104v1.
[8] M. E. Palistrant, Teor. Mat. Fiz. 168 (3), 503 (2011); [in English] Theor. Math. Phys. 168 (3), 1290, (2011).
[9] M. E. Palistrant, and F. T. Kochorbe, Physica C, 194 (3–4), 351, (1992).
[10] A. A. Abrikosov, L. P. Gorkov, and I. E. Dzyaloshinskii, Methods of Quantum Field Theory in Statistical Physics, Dover Public., Inc., New York, 1963.
[11] M. E. Palistrant and V. A. Ursu, Zh. Eksp. Teor. Fiz. 143, 4, 1 (2013); [in English] J. Exp. Theor. Phys. 116, 4, 641, (2013).
[12] M. E. Palistrant and V. M. Vakalyuk, Fiz. Nizk. Temp. 18, 847 (1992); [in English] J. Low Temp. Phys. 18, 597, (1992).
[13] Sergey L. Bud'ko, Ni Ni, and Paul C. Canfield, Phys. Rev. B 79, 220516, (2009); arXiv: 0907, 2936.

AN ULTRASOUND-ASSISTED SOL–GEL METHOD FOR THE SYNTHESIS OF NANO TITANIUM DIOXIDE

A. Abramova[2], V. Abramov[2], T. Gutul[1], A. Mirzac[1], and A. Sidorenko[1]

[1]*Institute of Electronic Engineering and Nanotechnologies "D.Ghitu", Academy of Sciences of Moldova, Academiei str. 3/3, Chisinau, MD-2028 Republic of Moldova*
E-mail: anatoli.sidorenko@kit.emu

[2]*Kurnakov Institute of General and Inorganic Chemistry of the Russian Academy of Sciences(IGIC RAS), Leninskii pr. 31, Moscow, 119991 GSP-1Russian Federation*
E-mail: anna_v_abramova@mail.ru

(Received August 25, 2016)

Abstract

An ultrasound-assisted sol–gel method is used to prepare titanium dioxide (TiO_2) nanoparticles. The resulting nanoparticles are characterized by scanning electron microscopy (SEM) and FTIR spectroscopy. The applicability of the method is verified; the morphology of the nanoparticles is compared with that of the particles prepared by a sol–gel method that was not assisted by ultrasound. The main advantage of the ultrasonically assisted sol–gel method is the possibility of avoiding the use of ethanol, which is crucial for the industry in terms of process upscaling possibilities and ecological requirements.

1. Introduction

Recently, sol–gel technologies for preparing ultrafine powders have found wide application due to the possibility of obtaining high-purity products with a predetermined particle size distribution and various combinations of components [1–2]. Sol–gel technology is based on transformations in the following sequence: hydrolysis → polymerization → nucleation → particle growth → sol formation → gel. Therefore, hydrolysis is the most important step of the sol–gel process. The material's quality is affected by hydrolysis catalysts, pH, the amount of water used, the type of solvents used, and temperature. It has been experimentally proven that homogenous condensation, phase formation and particle growth in different steps of hydrolysis lead to the formation of a sol and a gel. In this case, growth temperature and pH are factors that increase the particle growth rate in different steps of hydrolysis and control the dimension and crystallinity of the particles [1–2].

Titanium is a crucial material for a variety of applications. For example, colloidal solutions of TiO_2 nanoparticles, which exhibit antibacterial and antistatic properties, are increasingly often used in textile processing [3, 4]. The sol–gel method has high potential in the case of TiO_2 nanoparticle synthesis because the morphology and structure of the particles are crucial for the functional properties of the particles. In the case of sol–gel synthesis, titanium alkoxides, such as

tetraisopropoxide, titanium tetrabutoxide, or titanium tetrachloride, can be used as titanium-containing precursors [5]. Alcohols and ketones are suitable organic solvents for sol–gel methods in the case of TiO_2 synthesis.

It has been proven in several researches that the use of ultrasound can contribute to the formation of nanoparticles with a predetermined size in various processes [6, 7]. The use of ultrasound typically leads to the formation of smaller particles with a narrower particle size distribution [7]. In the case of Ti, it has been shown hat the use of ultrasound may also be of advantage for sol–gel synthesis [5]. The effect of ultrasound might also be important for the production of functionalized materials based on TiO_2, because it may be used for process triggering and particle size reduction in the case of hydrolysis at a low ethanol concentration. In the case of industrial processes, a reduction in the use of ethanolysis is very important for environmental and safety reasons.

In previous research, we prepared colloidal solutions and powders of zinc oxide nanoparticles using a combination of a sol–gel method and ultrasonic treatment [8].However, in recent years, few researches have been conducted to study nanoparticles obtained by a sol–gel method combined with ultrasonic treatment and the particle morphology. As mentioned above, the formation of titanium dioxide nanoparticles at low temperatures using inorganic solvents is relevant for industrial applications; it is especially important for the textile industry. Thus, the goal of this research is to study the particles prepared at a low ethanol concentration using an ultrasonically assisted sol–gel method and compare the morphology of the particles with that of the particles synthesized at a higher ethanol concentration in the absence of ultrasound.

2. Experimental

2.1. Materials and equipment

Titanium sulfate $Ti(SO_4)_2$ (≥99.7%), urea $(NH_2)_2CO$ (≥99.0%), ethanol (≥98.5 %), and sodium hydroxide (≥99.9%) were purchased from Sigma-Aldrich. Distilled water was used in the experiment. All chemicals were used as received without further purification.

The setup for ultrasonic treatment of the solution included a reactor (*1*) with the working volume of 1 L. The emitter of the oscillations contained a waveguide (*2*) and an ultrasonic transducer (*3*). The waveguide system was fixed in a position to provide the generation of ultrasonic oscillations in the liquid volume in the reactor. The setup power and the liquid volume were chosen to provide the generation of oscillations in the entire volume of the fluid. The transducer was powered by an ultrasonic generator (*4*).

The output of the acoustical power of the system was 2.0 kW, the working frequency of the transducer and waveguide was 25 kHz. The parameters of acoustical equipment made it possible to reach an intensity of ultrasonic radiation into the liquid of 10 W/cm^2. To maintain the operating temperature at 60ºC, a heat exchanger was used. A scheme and a photograph of the ultrasonic setup are shown in Fig. 1.

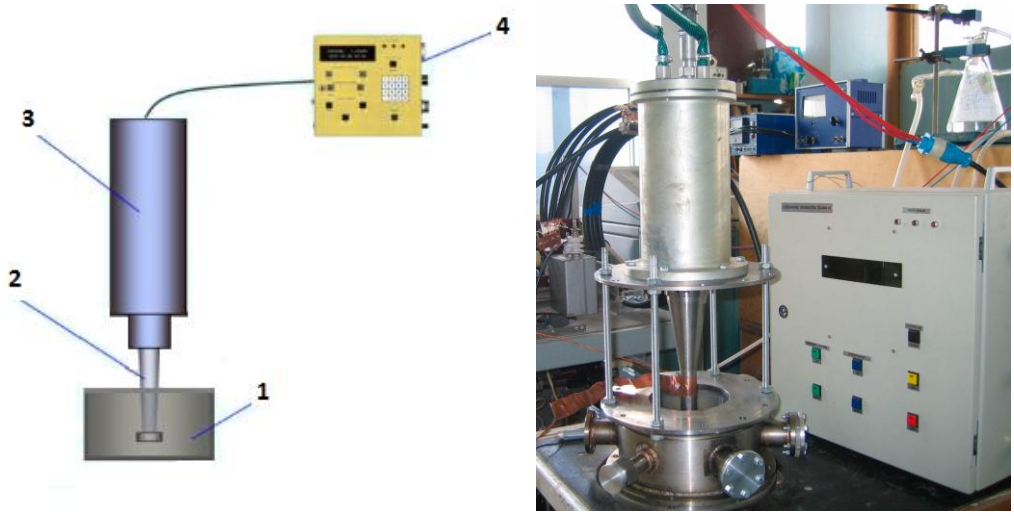

(a) (b)

Fig. 1. Scheme (a) and photograph (b) of the ultrasonic setup

Two samples of nano TiO_2 were synthesized for comparison and morphological analysis.

2.2. Synthesis of nanoTiO_2 (sample 1)

TiO_2 nanoparticles were synthesized by hydrolyzing titanium sulfate $Ti(SO_4)_2$. A certain amount of titanium sulfate with a weight of 0.96 g was completely dissolved in 80 mL of distilled water and 10 mL of ethanol. The designated amounts of urea (2.4 g) and surfactant were subsequently added to the above solution. Synthesis was conducted at 60˚C under stirring for 1 h. The resulting gel was dried at 80°C for 4 h.

2.3. Synthesis of nanoTiO_2 (sample 2)

TiO_2 nanoparticles were synthesized by hydrolyzing titanium sulfate $Ti(SO_4)_2$. A certain amount of titanium sulfate with a weight of 0.96 g was completely dissolved into 80 mL of distilled water. The designated amounts of urea (2.4 g) and surfactant were subsequently added to the above solution. The prepared mixture was placed into the ultrasonic setup and heated to 60˚C under continuous ultrasonic impact for 1 h; the best results analyzed herein were obtained after a 4-h treatment. The operating frequency of the ultrasonic oscillations was 25 kHz (standard frequency for industrial applications). The resulting gel was dried at 80°C for 4 h.

2.4. Methods

The resulting material was studied by FTIR spectroscopy using a PerkinElmer Spectrum 100 FTIR spectrometer in a spectral range of 650–4000 cm^{-1}. Scanning electron microscope (SEM) images were recorded with a Quanta 200 electronic microscope operating at 30 kV with secondary and backscattered electrons in a high vacuum mode.

3. Results and discussion

The morphology and sizes of the titanium dioxide nanoparticles are shown in Figs. 2 (sample 1) and 3 (sample 2). Apparently, in the presence of water, hydrolysis results in the formation of hydrocomplexes, which can be represented as linear weakly crosslinked 'polymers' [9]. Further gelation can lead to the rearrangement of the atoms and the adhesion of intersecting linear chains of the polymer; these processes also have an effect on the grain growth during heat treatment. .An important role in the formation of a gel matrix is played by water molecules, which contribute to the formation of a continuous bound system owing to hydrogen bonding.

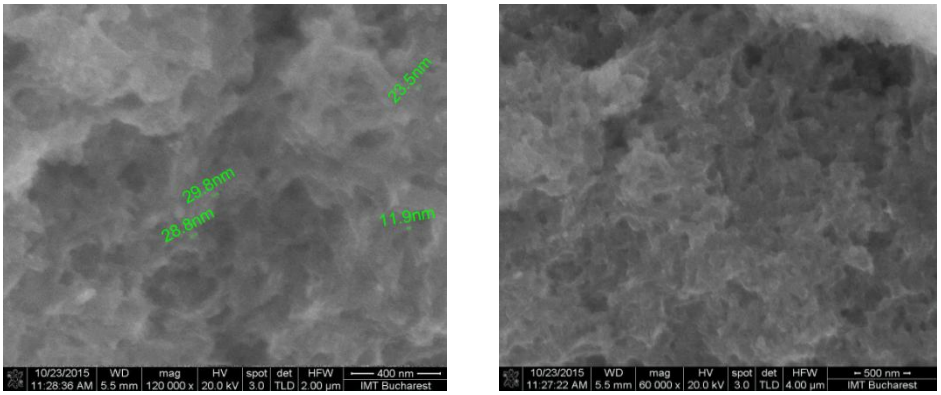

Fig. 2. SEM images of titanium dioxide nanoparticles (sample 1).

The micrographs in Fig. 2 show titanium oxide nanoparticles with sizes in a range of 10–30 nm in a gel matrix. The micrograph in Fig. 3 shows the nanoparticles synthesized using the ultrasonic setup. It was observed that these nanoparticles have a homogenous structure, which consists of well-formed spherical nanoparticles with sizes of about 50 nm.

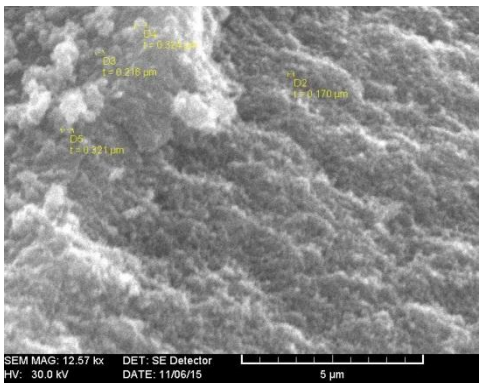

Fig. 3. SEM images of titanium dioxide (sample 2).

The FTIR spectra of TiO_2 nanoparticles of both samples lie in a range of 3600–550 cm^{-1}. No significant differences in the spectra of the two different samples were observed. A broad band was observed in a region of 3600–1650 cm^{-1}; it is assigned to stretching vibrations of hydroxyl (O–H), representing the water as moisture. An absorption band around 2054–2302 cm^{-1}

was observed; it is attributed to the existence of CO_2 molecules in the air. In both cases, we observed a peak between 800 and 450 cm^{-1}; this peak was assigned to the Ti–O stretching bands [10]. Strong absorption between 800 and 450 cm^{-1} has confirmed that the synthesized particles were TiO_2 nanoparticles.

4. Conclusions

In the present study, we have investigated the conditions of synthesis of nanosized titanium dioxide particles using a sol–gel method. We have studied the effect of ultrasound on the resulting nanoparticles and analyzed the possibility of using ultrasound during synthesis to avoid or reduce the use of ethanol. The morphology of the resulting nanoparticles has been studied. The research has confirmed that ultrasound contributes to the formation of nanoparticles with a homogeneous shape and a narrow size distribution. The research has shown a great potential for the application of ultrasound in new environmentally friendly industrial processes for the formation of TiO_2 nanoparticles with predefined characteristics owing to the substantiated possibility of reducing the ethanol consumption.

References

[1] Yu. Qiao-Zhen and Ai-Ai Shen, J. Fiber Bioeng. Inf. 64, 65, (2008).
[2] S. Ortelli, A.-L. Costa, and M. Dondi, Materials 8, 7988, (2015).
[3] Patent RU 2517121
[4] http://www.plasmatreat.de/industrieanwendungen/textilfertigung/funktionalisierung-von-geweben/antibakterielle-textilbeschichtung.html, accessed September 22, 2015.
[5] D. V. Pinjari, Krishnamurthy Prasad, P.R. Gogate, S.T. Mhaske, and A.B. Pandit, Ultrason. Sonochem.23, 185, (2015).
[6] A. Abramova, A. Gedanken, V. Popov, E.-H. Ooi, T. J. Mason, E. M. Joyce, J. Beddow, I. Perelshtein, and V. Bayazitov, Mater. Lett. 96, 121, (2013).
[7] A. V. Abramova, V. O. Abramov, A. Gedanken, I. Perelshtein, and V. M. Bayazitov, Beilstein J. Nanotechnol. 5, 532, (2014).
[8] T. Gutul, E. Rusu, N. Condur, V. Ursaki, E. Goncearenco, and P.Vlazan, Beilstein J. Nanotechnol. 5, 402, (2014).
[9] T. Sugimoto, X. Zhou, and A. Muramatsu, J. Colloid Interface Sci. 252, 339, (2002).
[10] C. Wang, Z.-X. Deng, and Y. Li, Inorg. Chem. 40, 5210, (2001).

s

PHOTOELECTRICAL PARAMETERS OF *n*CdS–*p*CdTe THIN-FILM SOLAR CELLS WITH A CdO BUFFER LAYER

P. Gashin, L. Gagara, P. Ketrush, I. Inculetz, V. Fiodorov, and Al. Quassem Amjad

Moldova State University, Mateevici str. 60, Chisinau, Republic of Moldova
Email: gashinpetru@yahoo.com

(Received July, 29)

Abstract

The results of the studies of the effect of a CdO buffer layer on the photoelectrical parameters of CdS–CdTe solar cells have been described. It has been found that the formation of a 5–8 nm thick CdO buffer layer leads to an increase in the CdS–CdTe solar cell open circuit voltage (V_{oc}) by 90–140 mV, short circuit current (I_{sc}) by 1.4–3.2 mA/cm^2, and efficiency by 2.8–4.1% at 300 K and an illumination of 100 mW/cm^2.

1. Introduction

Cadmium telluride (CdTe) is one of the main materials for the fabrication of low-cost solar cells, which is stipulated by the theoretically predictable efficiency up to 30% of the single junction device structures based on CdTe [1, 2]. Recently, the efficiency of laboratory samples of CdTe-based solar cells and large area modules of 19.6 and 16.1%, respectively, has been achieved [3]. However, this efficiency is considerably lower than the theoretical limit; therefore, the exploration of the possibilities of enhancing this parameter is important from both theoretical and economical viewpoints.

The key element of these solar cells is the thin-film *n*CdS–*p*CdTe heterostructure. A CdS thin film is used as a "window" for the radiation to the active *p*CdTe layer.

The efficiency of solar cells based on *n*CdS–*p*CdTe heterojunctions is mainly determined by recombination loses at the interface. To enhance the solar cell efficiency, it is necessary to decrease the interface state concentration. For this purpose, different buffer layers formed at the *n*CdS–*p*CdTe hetrojunction interface are used.

The results of the effect of a nanothick CdO buffer layer on the photoelectrical parameters of *n*CdS–*p*CdTe solar cells are described in this paper.

2. Experimental

CdS–CdTe heterojunctions were prepared by successive deposition of CdS and CdTe layers onto glass substrates (2×2 cm^2). The substrates were previously covered with a transparent (~80%) conducting (~10^{-3} Ω m) SnO_2 layer deposited by the “quasi-closed space” method. The effect of the source and substrate temperatures on the structure and electrophysical parameters of CdS and CdTe layers was studied to determine the optimum temperatures:

T_{sour} = 580°C and T_{sub} = 390°C for CdS and T_{sour} = 535°C and T_{sub} = 450°C for CdTe.

The CdS layers had the thickness of 0.3–0.6 μm and the electron concentration of 1.6×10^{18} cm^{-3}; the CdTe layers had the thickness of 8–14 μm and the hole concentration of 2×10^{15} to 8×10^{15} cm^{-3}.

Before the deposition of the CdTe layer, a thin CdO layer (5–50 nm) was deposited onto a part of the CdS layer. CdO layers were prepared by magnetron sputtering of a cadmium plate in an oxygen atmosphere at a direct current. CdO layer thickness was controlled by the time of sputtering and determined from the calibration curve of the dependence of the CdO layer thickness on sputtering duration.

The resulting thin-film heterostructures were subjected to a "chloride" treatment to enhance their photosensitivity. For this purpose, the structures were exposed to a methanol–$CdCl_2$ solution for 3–5 h. After that, a heat treatment at 380°C was conducted for 30 min.

The CdS–CdTe heterojunction configuration (Fig. 1) provides measurements of the dependences for elements with and without a CdO layer prepared under similar technological conditions.

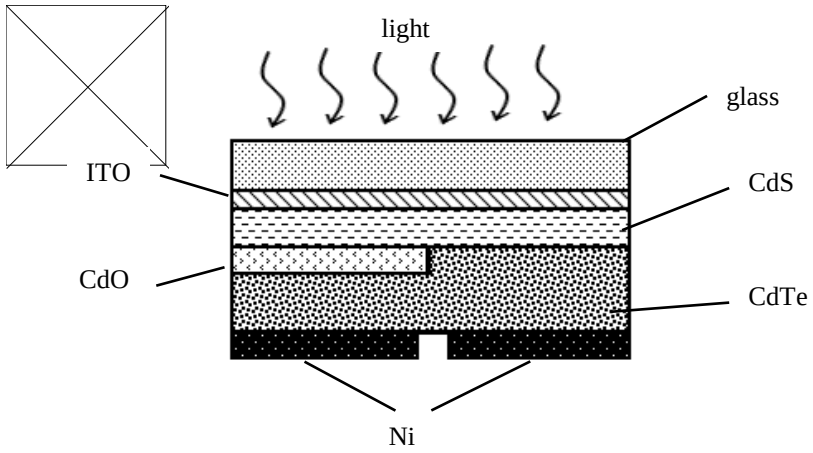

Fig. 1. Cross section of a CdS–CdTe solar cell with a CdO buffer layer.

The *I–U* dependences of SnO_2–CdS–CdO–CdTe–Ni and SnO_2–CdS–CdTe–Ni structures were studied using a KEITHLEY 4200-SCS measurement unit. The photosensitivity spectra of the heterojunctions were studied using an MDR-23 monochromator with a resolution power of 2.6 nm/mm. All spectra were normalized to the quantity of incident photons.

3. Experimental results and discussion

The high value of surface recombination rate considerably decreases the solar cell output power and conversion efficiency. The current intensity in the solar cell external circuit is given by the formula [1]

$$I = I_0\left(e^{\frac{eU}{e^{nkT}}} - 1\right) - I_f \qquad (1)$$

Where I_0 - is saturation current, I_f –is photocurrent. The surface recombination increases saturation current and decreases the solar cell output voltage:

$$U_{xx} = \frac{nkT}{e} \cdot ln\left(\frac{I_f}{I_0} + 1\right) \quad (2)$$

Since I_0 and I_f depend on surface recombination rate, the quantitative comparison of the effect of the CdO buffer layer can be made by coming from the efficiency of I_0 decreasing and I_f increasing in the structures with a CdO buffer layer compared with the structures without this layer.

The studies of *I–U* dependences of *n*CdS–*p*CdTe heterojunctions with and without a CdO buffer layer showed that the presence of a CdO layer does not change the current flow mechanism; however, it decreases saturation current I_o.

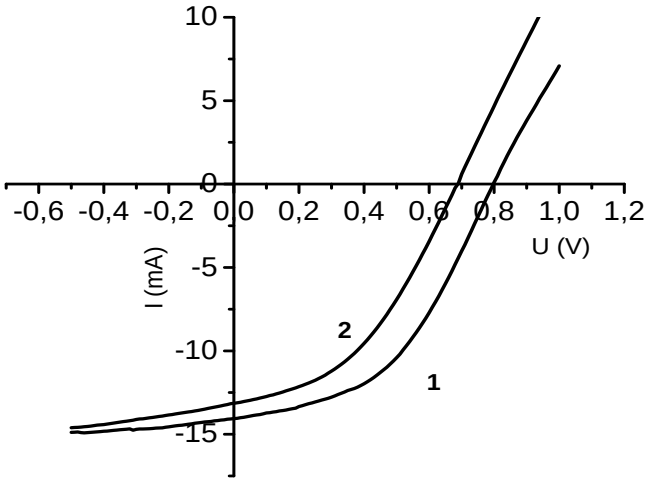

Fig. 2. *I–U* dependences under illumination for SC: (*1*) CdS–CdO–CdTe and (*2*) CdS–CdTe.

The load dependences of the CdS–CdO–CdTe structure (CdO layer thickness of ≈6 nm) (curve *1*) and the *n*CdS–*p*CdTe heterojunction (curve *2*) measured at 300 K and an illumination of 100 mW/см^2 are shown in Fig. 2. The photoelectrical parameters, such as fill factor FF and efficiency of solar energy conversion to electrical one, determined from these dependences are as follows: for *n*CdS–*p*CdTe heterojunction: U_{oc} = 0.69 V, I_{sc} = 26. 53 mA/cm^2, FF = 0.46, ŋ = 7.32%; for the CdS–CdO–CdTe structure: U_{oc} = 0. 8 V, I_{sc} = 25.7 mA/cm^2, FF = 0.42, ŋ = 9.76%. The photoelectrical parameters of a set of structures with and without a CdO layer, which were measured under the same conditions, are given in the table.

Table 1. Open circuit voltage and short circuit current of CdS–CdTe heterojunctions with and without a CdO layer measured at 300 K and an illumination of 100 mW/cm^2

Samples	U_{oc}, V	I_{sc}, mA/cm^2
Г53, CdO	0.77	25.8
-----	0.68	21.4
Г151, CdO	0.81	25.6
-----	0.68	23.2
Г197, CdO	0.79	24.0
-----	0.70	22.0
Г227, CdO	0.78	26.4
-----	0.64	26.0
Г228, CdO	0.77	26.2
-----	0.67	26.0
К136, CdO	0.79	22.4
-----	0.70	20.0
Г176, CdO	0.78	26.2
-----	0.61	19.4
Г177, CdO	0.78	25.2
-----	0.70	22.0

It is evident from the table that all structures containing a CdO layer have higher photoelectrical parameters: U_{oc} by 90–140 mV and I_{sc} by 1.4–3.2 mA/cm^2.

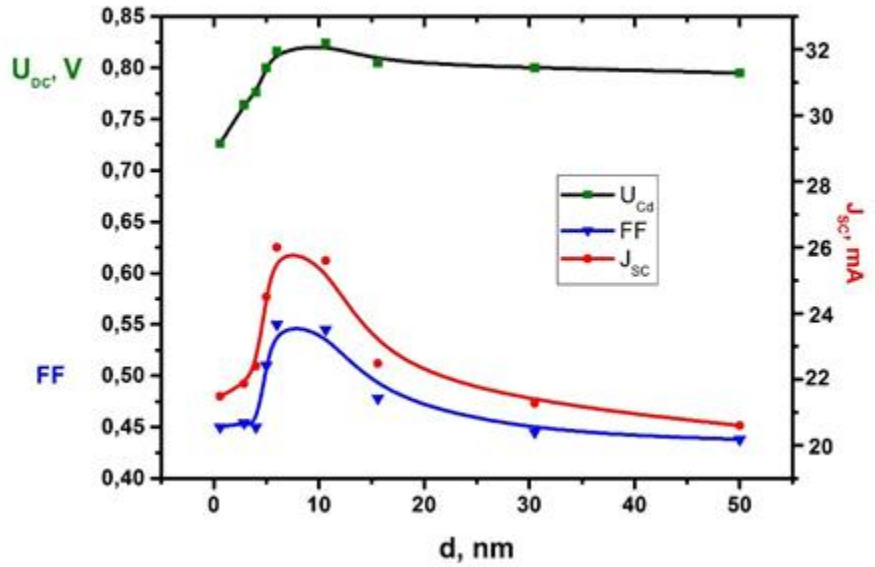

Fig. 3. U_{oc} , I_{sc} ,FF, and efficiency as a function of the CdO buffer layer thickness for the CdS–CdO–CdTe SC.

Dependences of U_{oc} , I_{sc}, FF, and efficiency of solar energy conversion into electrical on CdO layer thickness for the *n*CdS–*p*CdTe heterojunction with a buffer CdO layer at the interface, which were measured at 300 K and an illumination of 100 mW/cm^2, are shown in Fig. 3.

It is evident that the CdO layer thickness has a significant effect on the short circuit current and fill factor of the load characteristic; for open circuit voltage, it sharply increases at low values of CdO layer thickness; for thicknesses higher than 10 nm, U_{oc} remains unchanged at a level of ~0.8 V.

From the analysis of the given dependences it was determined that the optimum thickness of the CdO layer is 5–8 nm. This finding is attributed to the fact that, at low thicknesses, the CdO layer is tunnel-transparent for charge carriers, while at high thicknesses, this layer blocks the charge carrier flow.

The study of the photoluminescence of the CdTe layers at luminescence excitation through a CdS layer showed that, in the case of formation of a CdO layer, the luminescence spectral distribution does not change and its intensity increases by 1.4–1.6 times. This feature indicates that the introduction of a CdO buffer layer leads to a decrease in the concentration of recombination centers at the *n*CdS–*p*CdTe heterojunction interface.

The sensitivity spectral region for *n*CdS–*p*CdTe heterojunctions with and without a CdO layer is located in a wavelength region of 0.50–0.83 μm (Fig. 4); that is, it is limited by the photon energy close to the band gap of the heterojunction component materials. The spectral sensitivity is fairly homogeneous and exhibits sharp edges, which indicate the absence of the predominant effect of volume recombination on charge carrier collection. The presence of a CdO layer does not change the shape of the sensitivity spectral dependence and only increases the sensitivity.

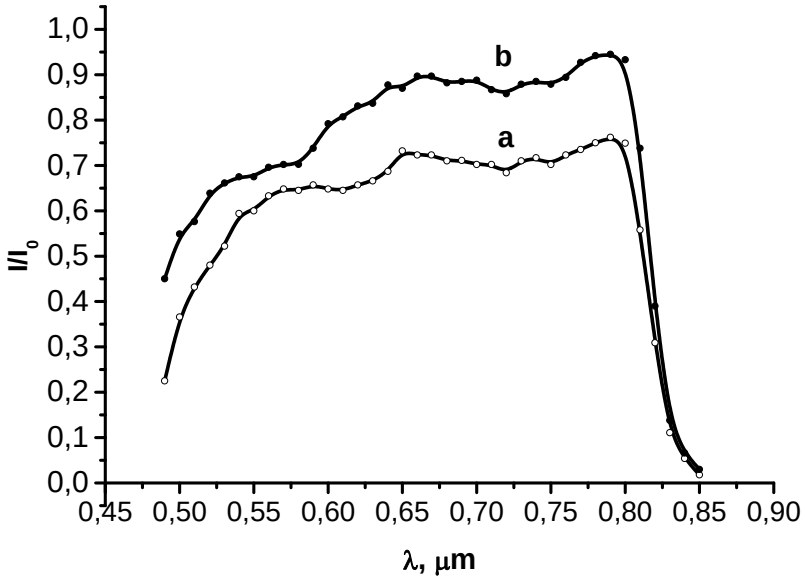

Fig. 4. Photosensitivity spectrum of (a) CdS–CdTe and (b) CdS–CdO–CdTe SC.

4. Conclusions

The formation of a thin (5–8 nm) CdO layer at the *n*CdS–*p*CdTe heterojunction interface leads to a decrease in the recombination center concentration, which results in an increase in the efficiency of the solar energy conversion to electrical one by 2.8–4.1%.

References

[1] K. Durose, P. R. Edwards, and D. P. Holiday. J. Cryst. Growth, 197, 733 (1999).
[2] C. H. Henry, J. Appl. Phys. 51(8), 4494 (1980).
[3] M. A. Green, K. Emery, Y. Hishikawa, W. Warta, and E. D. Dunlop, Prog. Photovolt. Res. Appl. 21 (1), 1 (2013).
[4] H. R. Moutinho, M. M. Al-Jassim, D. H. Levi, P. C. Dippo, and L. L. Kamerski, J. Vac. Sci. Technol. A16, 1251, (1998).

A LOW-TEMPERATURE STUDY OF THE UV EMISSION IN SOL-GEL DIP-COATED SILVER-DOPED ZINC OXIDE THIN FILMS

L. Hammiche, D. Djouadi*, and A. Chelouche

Laboratoire de Génie de l'Environnement (LGE), Faculty of Technology, University of Bejaia, Algeria

**E-mail: djameldjouadi@yahoo.fr*

Abstract

Undoped and 3 at % Ag-doped ZnO thin films deposited on glass substrates by the sol–gel dip-coating technique have been studied. X-ray diffraction (XRD) measurements have revealed that the two films are polycrystalline and exhibit a ZnO hexagonal wurtzite structure with an average crystallite size of less than 5 nm. SEM images have demonstrated a homogeneous dispersion of the grains with a spherical morphology of the doped sample. The optical transmittance of the deposited films has indicated that the films transparency exceeds 80% in the visible range. The room temperature photoluminescence (PL) spectra have shown that the UV band (385 nm) intensity is not affected by Ag doping. The PL spectra of pure ZnO thin film have revealed that the bound exciton (BX) and the free exciton (FX) emissions are dependent on recorded temperature. The PL spectrum at 77 K of Ag-doped ZnO has demonstrated that doping with silver enhances BX and optical phonons replica (2LO) (centered at 3.168 eV) emissions. This result indicates that the peak observed at 3.168 eV is not only due to 2LO but also to the transition of electrons from the conduction band to a defect level induced by silver atoms in ZnO crystallites.

Keywords: Ag-doped ZnO, thin films, sol–gel, dip-coating, low-temperature photoluminescence

1. Introduction

Nanosized wurtzite ZnO is one of the most thoroughly studied semiconductor oxides due to promising applications of this material in optoelectronic and UV photodetectors [1], which are mostly associated with the specific properties of ZnO, such as a wide band gap (3.37 eV) and a large exciton binding energy (60 meV) at room temperature. The optical properties of undoped and transition metal-doped ZnO thin films have been intensively studied in order to improve emission efficiency. Silver is considered as a promising element for doping ZnO because it acts as an acceptor and is actively involved in the improvement of the UV emission [2–5]. Gruzintsev et al. [6] have reported that silver can be considered as a good candidate for producing a shallow acceptor level in ZnO when the metal substitutes Zn sites. Kang et al. [7] have demonstrated the possible synthesis of p-type ZnO by the substitution of Ag ions into Zn ion sites.

Silver-doped ZnO nanostructured thin films have been synthesized using various techniques [8–12]; the sol–gel method is the most common to prepare thin films with a controlled doping level and minimize the intrinsic defect concentration.

The violet luminescence from ZnO thin films prepared by pulsed laser deposition (PLD) was observed for the first time by Jin et al. [13]. This emission is the result of the existence of defects. It is largely accepted that, in ZnO, defects are oxygen vacancy (V_O), zinc vacancy (V_{Zn}), interstitial oxygen (O_i), interstitial zinc (Zn_i) and antisite oxygen (O_{Zn}) with different oxidation degrees. The energy levels of these defects were calculated by Xu et al. [14] using the full-potential linear muffin-tin method. At low temperatures, the semiconductor crystals photoluminescence (PL) has complex spectral emissions in the near band gap region resulting from excitonic trapping and associated effects.

Low-temperature PL spectroscopy is a sensitive tool for the characterization of impurities and a helpful method for understanding the optical and electrical performances of the materials [15]. Generally, at low temperatures, the thermal broadening and deactivation effects (observed at higher temperatures) are reduced and the bound exciton recombination dominates the PL emission. In the literature, few works have been reported on the dependence of PL of Ag-doped ZnO thin films on temperature. For example, Lu et al. [16] have reported the effect of O_2 partial pressure on the UV emission of ZnO thin films grown by PLD using the low-temperature PL spectroscopy. Djurisic and et al. [17] have studied the temperature dependence of the excitonic emission spectra of ZnO nanorods synthesized by a hydrothermal process. However, to the best of our knowledge, the temperature dependence of the UV emission of Ag-doped ZnO thin films synthesized by the sol–gel process has not yet been reported.

In this paper, ZnO thin films are prepared by the sol–gel method and dip-coated on glass substrates. The temperature-dependent UV emission of pure and 3% Ag-doped ZnO thin films is investigated.

2. Materials and methods

In this study, zinc acetate 2-hydrate, ethanol, and diethanolamine (DEA) were used as a zinc precursor, solvent, and stabilizer, respectively, to prepare a 0.6 M sol concentration. An Ag-doped ZnO sol was prepared by adding silver nitrate to zinc acetate to obtain a solution with an atomic ratio of [Ag]/[Zn] = 0.03. Undoped ZnO and 3% Ag-doped ZnO solutions were subjected to continuous magnetic stirring at 40°C for 1 h. The films were deposited on glass substrates using the dip-coating technique. The pulling speed and the number of the deposited layers were fixed at 20 mm/min and 3, respectively. After each deposited layer, the film was preheated at 200°C for 40 min. Finally, the prepared thin films were annealed in a muffle furnace at 500°C for 2 h.

The prepared thin films were characterized by grazing incidence X-ray diffraction (XRD) using a PanAnalytical diffractometer. X-rays were produced from a CuK_α radiation source (wavelength 1.5418 Å) at an acceleration voltage of 40 kV and a current of 30 mA. SEM images were recorded using a Zeiss scanning electron microscope. Optical transmittance spectra were recorded using a Safas uvmc^2 UV-Visible spectrophotometer. The PL spectra were recorded using a Jobin–Yvon HR460 spectrophotometer; the samples were excited by a 244 nm wavelength laser.

3. Results and discussion

Figure1 show XRD patterns of undoped and 3% Ag-doped ZnO thin films prepared by the sol–gel process. The peak positions indicate that both deposited films exhibit a ZnO polycrystalline wurtzite hexagonal structure. The addition of Ag atoms leads to a shift of the

pronounced peaks toward small diffraction angles. The result indicates an increase in the lattice parameters. After Ag-doping, the lattice parameters values increased from 5.1699 to 5.2672 Å for "*c*" and from 3.2315 to 3.2756 Å for parameter "*a*".
In wurtzite ZnO, the Zn–O bond length *L* is given by the following formula [18, 19]:

$$L = \sqrt{\left(a^2/_3\right) + (0.5 - u)^2 c^2} \quad (1)$$

where the parameter u is given (in the wurtzite structure) by the equation [18, 19]

$$u = \left(a^2/_{3c^2}\right) + 0.25 \quad (2)$$

The calculated Zn–O bond length in the pure and Ag-doped ZnO films is found to be 1.96577 and 1.9958 Å, respectively. An increase in the Zn–O bond length in the Ag-doped ZnO film shows that Ag atoms substitute the zinc atoms in the ZnO lattice. Since the radius of the Ag^+ ion (1.22Å) is greater than that of the Zn^+ ion (0.72Å), an increase in the number of Ag ions in the Zn lattice sites expands the lattice parameters [20].
The crystallites size values were calculated by the Scherer's equation

$$D = \frac{0.89\lambda}{\beta cos\theta} \quad (3)$$

where λ is the X-ray wavelength (1.5418 Å), β is the full width at half-maximum of the ZnO (101) line (in radians), and θ is the diffraction angle.

The crystallites size was not strongly modified after the addition of silver atoms (<5 nm). The relatively strong intensity of the (101) peak shows that heterogeneous nucleation can be easily implemented in the presence of silver ions in the ZnO structure, which contributes to the growth rate in this direction.

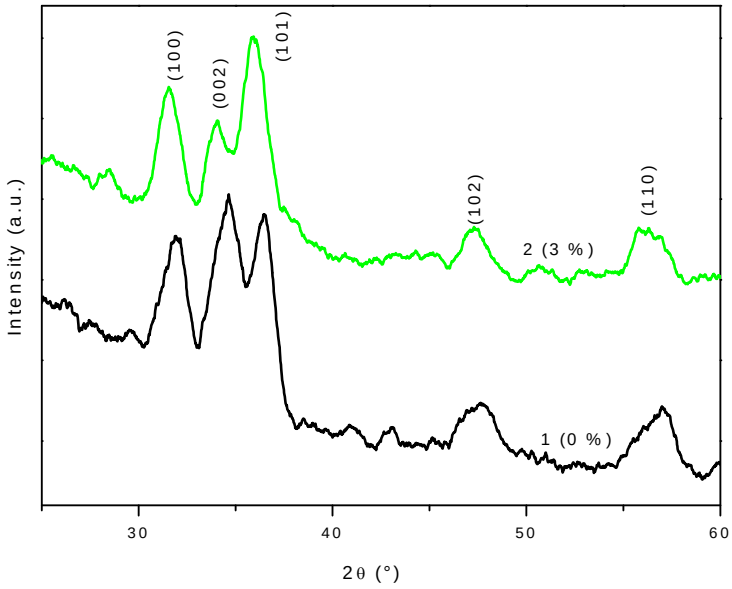

Fig. 1. XRD patterns of (*1*) the undoped and (*2*) 3% Ag-doped ZnO thin films.

Figure 2 shows the SEM micrographs of the undoped and 3% Ag-doped ZnO thin films. They demonstrate a homogeneous distribution of ZnO crystallites on the surface of the glass substrate. It is evident that the undoped film is more compact. On the other hand, the Ag-doped ZnO grains are spherical and their average size is greater than that of the undoped grains. The presence of some pores in the Ag-doped film is observed.

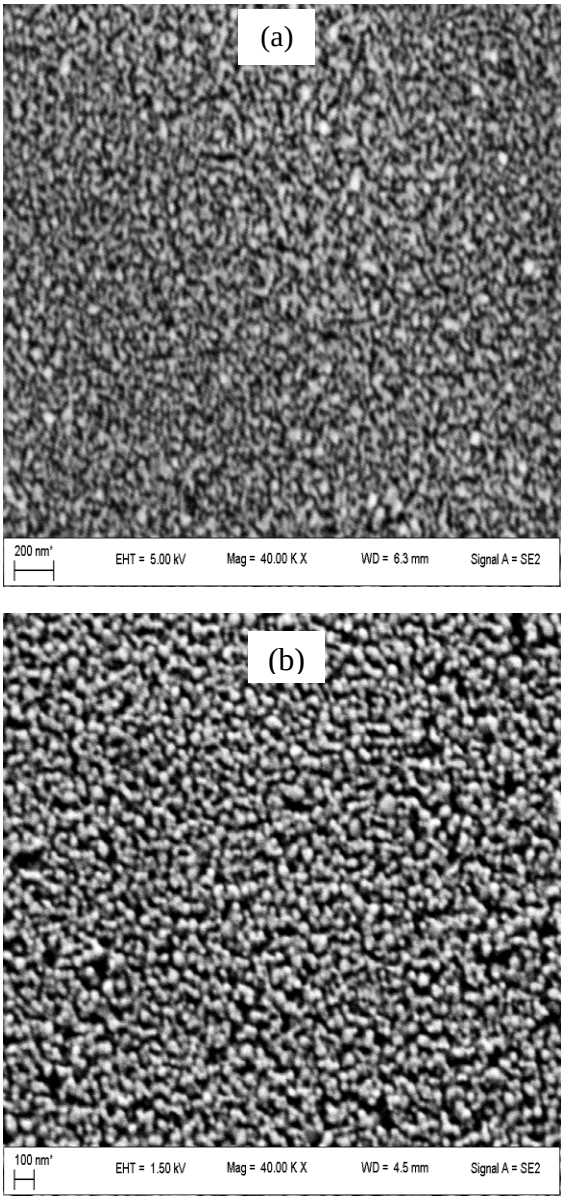

Fig. 2. SEM images of (a) the undoped and (b) 3% Ag-doped ZnO thin films.

The optical transmittance spectra of the films are shown in Fig. 3a. Both the undoped and Ag-doped ZnO films have high transparency in the visible range. The introduction of Ag atoms leads to an increase in the transmittance with a slight shift toward shorter wavelengths. Figure 3b shows the plot of $(\alpha h\nu)^2$ versus photon energy ($h\nu$) obtained from the data of Fig. 3a. Extrapolation of the linear portion to the energy axis at $(\alpha h\nu)^2 = 0$ gives the value of the optical

band gap E_g. The estimated E_g value is about 3.255 eV for both films. The results indicate that the optical band gap is not affected by the introduction of Ag ions in ZnO at the used silver doping concentration.

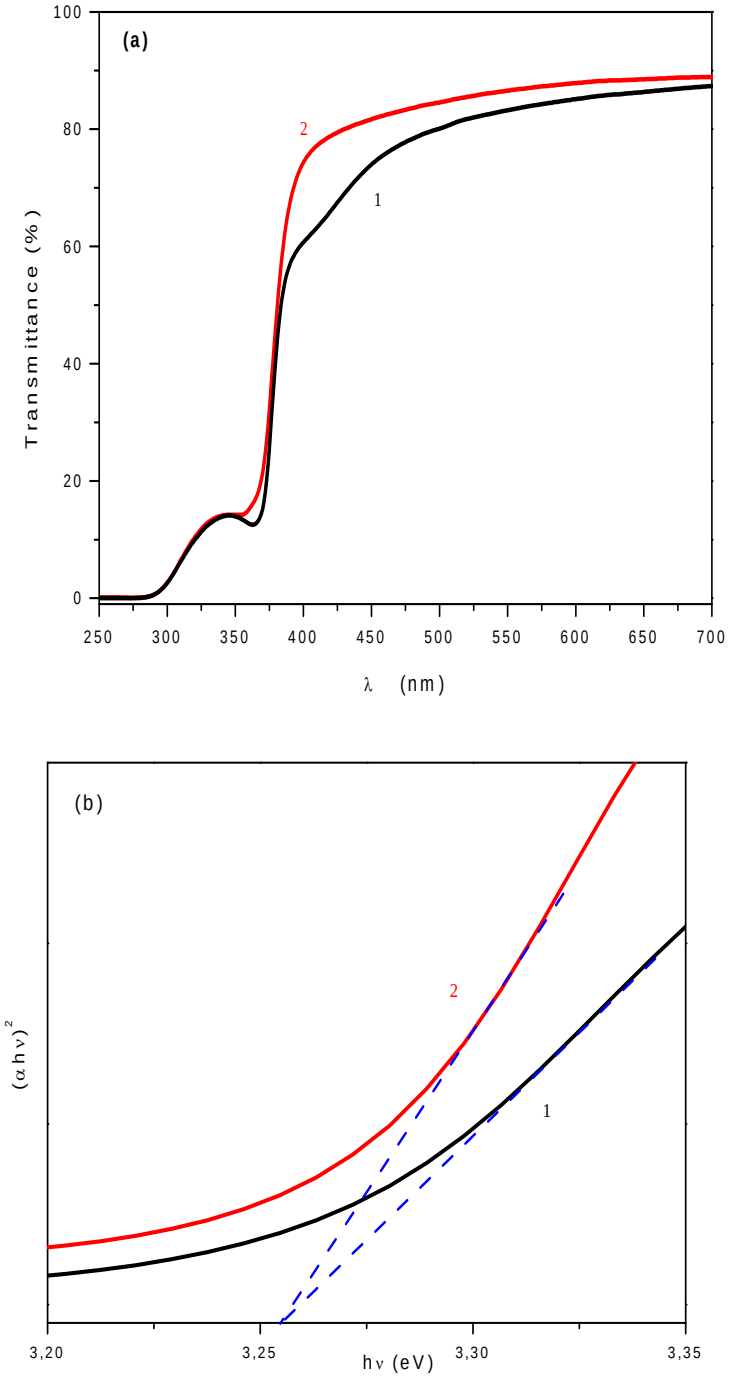

Fig. 3. (a) Transmittance spectra and (b) $(\alpha h\upsilon)^2$ versus photon energy plots of (*1*) the undoped and (*2*) 3% Ag-doped ZnO thin films.

Figure 4 shows the current–voltage curves of the pure and 3% Ag-doped ZnO thin films prepared by the sol–gel process. It can be seen that the current linearly increases with increasing applied voltage; this finding indicates an ohmic behavior of the prepared ZnO thin films. The electrical resistance in pure ZnO is greater than that in the doped film because the conductivity of ZnO films is slightly improved with the incorporation of Ag ions. Xian and et al. [21] have reported similar results. This result can also be attributed to the fact that silver doping can greatly enhance the separation of electron–hole pairs.

Room temperature UV PL spectra of the undoped and 3% Ag-doped ZnO thin films are shown in Fig. 5. Both spectra exhibit a very weak UV emission peak centered at 385 nm corresponding to the near band edge (NBE) emission which is attributed to exciton transitions. The introduction of Ag ions does not affect the intensity and position (no shift is observed) of NBE emission band. The result suggests that 3% Ag doping does not induce any modification in the optical band gap, as confirmed by the optical transmittance measurements.

The NBE emission spectra of the undoped and 3% Ag-doped ZnO thin films at the liquid nitrogen temperature (77 K) are shown in Fig. 6. It is evident that the intensity of NBE emission of the 3% Ag-doped ZnO film is much higher than that of the undoped one. Xu et al. [22] reported that the enhancement of the NBE emission in Ag-doped ZnO thin films can result from a new luminescence center caused by Ag atoms. We can state that the enhancement of the UV emission is probably due to the fact that the photoelectrons easily escape from Ag ions which lead to a low diffusion of excitons in ZnO and, therefore, to an increase in their concentration.

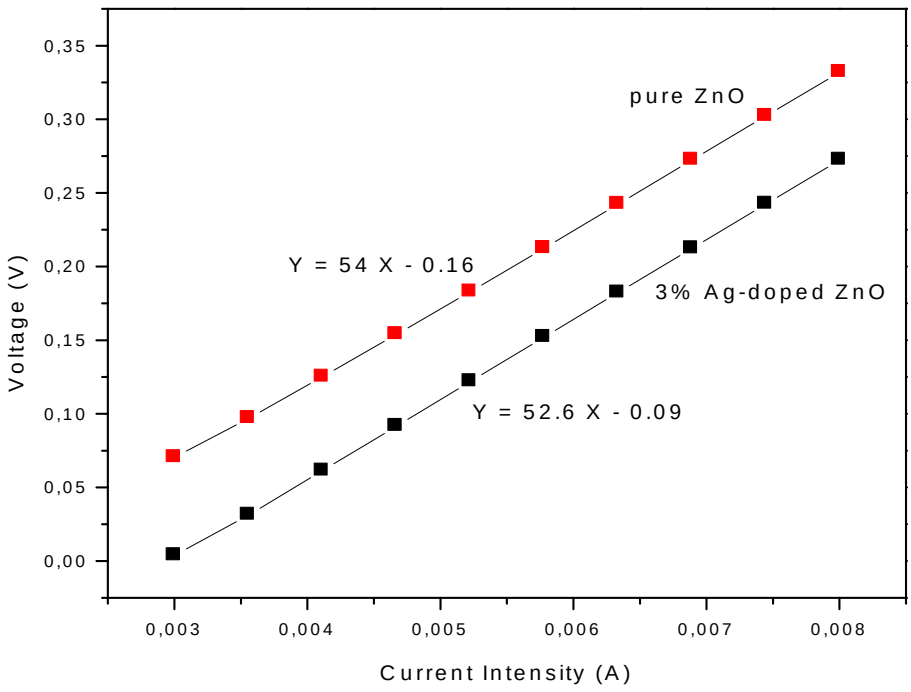

Fig. 4. Current–voltage curves of the pure and 3% Ag-doped ZnO thin films.

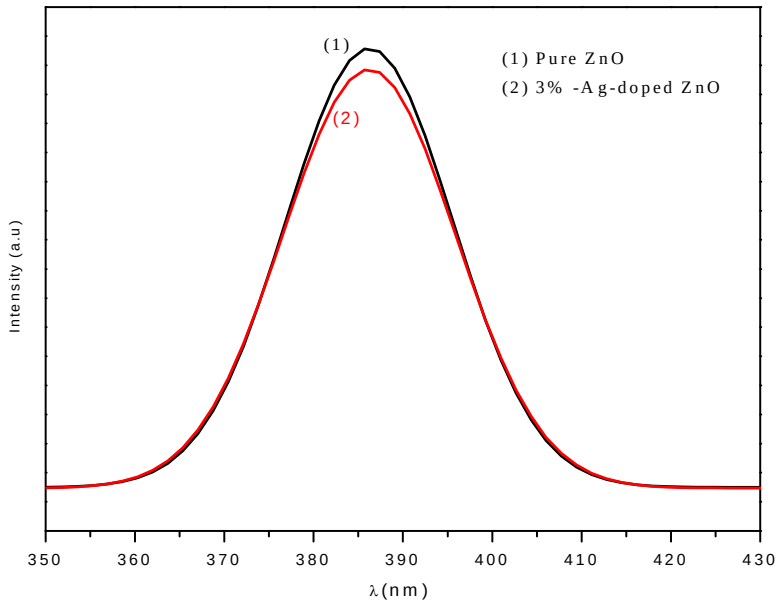

Fig. 5. Room-temperature UV PL spectra of the (*1*) undoped and (*2*) 3% Ag-doped ZnO thin films.

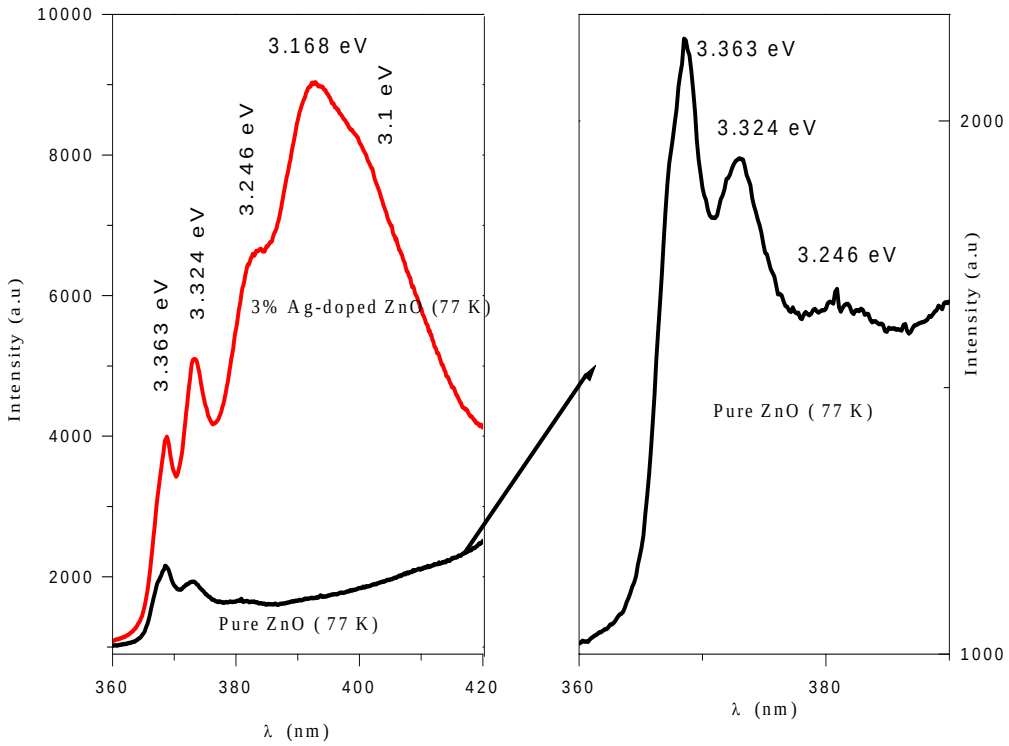

Fig. 6. UV PL spectra of undoped and 3% Ag-doped ZnO thin films at 77 K.

It is evident that the NBE emission of the undoped ZnO thin film consists of three bands centered at 3.363, 3.324, and 3.246 eV. The peak at 3.363 eV is attributed to the radiative recombination of free excitons (FX) and the band centered on 3.324 eV is due to the recombination of bound excitons (BX). It is well established that the longitudinal optical (LO) phonon is the dominant lattice relaxation in ZnO during PL excitation; the LO phonon energy is found to be 72 meV [23]. The peak at 3.246 eV is attributed to the transition assisted by the first-LO phonon replica (1LO). The NBE PL spectrum of 3% Ag-doped ZnO shows various peaks at 3.363, 3.324, 3.246, and 3.168 eV and a shoulder at 3.10 eV. Peaks at 3.168 and 3.10 eV were not observed in the spectrum of undoped ZnO. These peaks can be attributed to Ag ions or defect level transitions. The emission of these two lines can also be attributed to the second-LO (2LO) (3.168 eV) and third-LO (3LO) (3.10 eV) phonon replicas since they are approximately separated by the ZnO LO phonon energy. The absence of 2LO and 3LO peaks in pure ZnO is due to an increase in the thermal activation energy which becomes larger than the binding energy of related excitons [24]. The most important emission in the Ag-doped ZnO film observed at 77 K is due to the 2LO optical phonon (3.168 eV); the BX emission (3.324 eV) is higher than the FX emission (3.363 eV), while in the undoped ZnO film, the FX emission is higher than the BX emission. At the nitrogen temperature, pure ZnO shows a dominant UV emission from FX; in the Ag-doped ZnO film, the dominant emission is from BX and longitudinal optical (LO) phonon replica peaks. The spectra show that Ag doping can enhance all the PL emissions in the UV. The BX emission and the related LO phonon replicas are significantly enhanced in Ag-doped ZnO. The LO phonon is found to be the dominant lattice relaxation in the Ag-doped ZnO film during PL; LO phonon replicas for most of NBE features are distinguishable.

The UV PL spectra measured at different temperatures for the undoped and 3% Ag-doped ZnO thin films are shown in Fig. 7. It is evident that both BX and FX emission intensities increase with decreasing temperature. However, the BX emission of Ag-doped ZnO decreases with increasing temperature and completely disappears at 150 K (13 meV). This finding is attributed to the fact that the thermal activation energy increases and becomes greater than the related binding energy. Due to the depopulation of defects with increasing temperature, the bound exciton features in Ag-doped ZnO can exhibit transitions which are observed only at temperatures below 77 K. The FX emission at 77 K in pure ZnO is more intense than the BX emission.

In addition, it is evident that the UV emission edge is shifted to the region of lower wavelengths with decreasing temperature in both thin films. This shift is due to an increase in the band gap with decreasing temperature. In addition, for the same reasons, the positions of the bands observed at 3.363 and 3.324 eV in the undoped and doped films are shifted to lower energies. Note that the introduction of Ag atoms in ZnO does not affect the FX and BX band positions. For the Ag-doped film, the intensity of NBE emission peaks decreases with decreasing temperature from room temperature to 250 K and then strongly increases for lower temperatures (from 250 to 77 K). This behavior is probably due to the supremacy of the exciton band-to-band emission. It is well known that this emission disappears with increasing temperature in the semiconductor [25]. This temperature dependence is dominated by the transition between the BX emission at low temperature and the FX emission at high temperature [26]. For Ag-doped ZnO, the most intense emission observed at 77 K is due to the 2LO phonon replica. These distinguishable emissions observed only at 77 K indicate that doping with silver enhances the BX emissions and 2LO phonon replica. It is probable that the peak at 3.168 eV is attributed not only to 2LO, but also to the transition of electrons from the conduction band to a defect level induced by the introduction of silver atoms in ZnO.

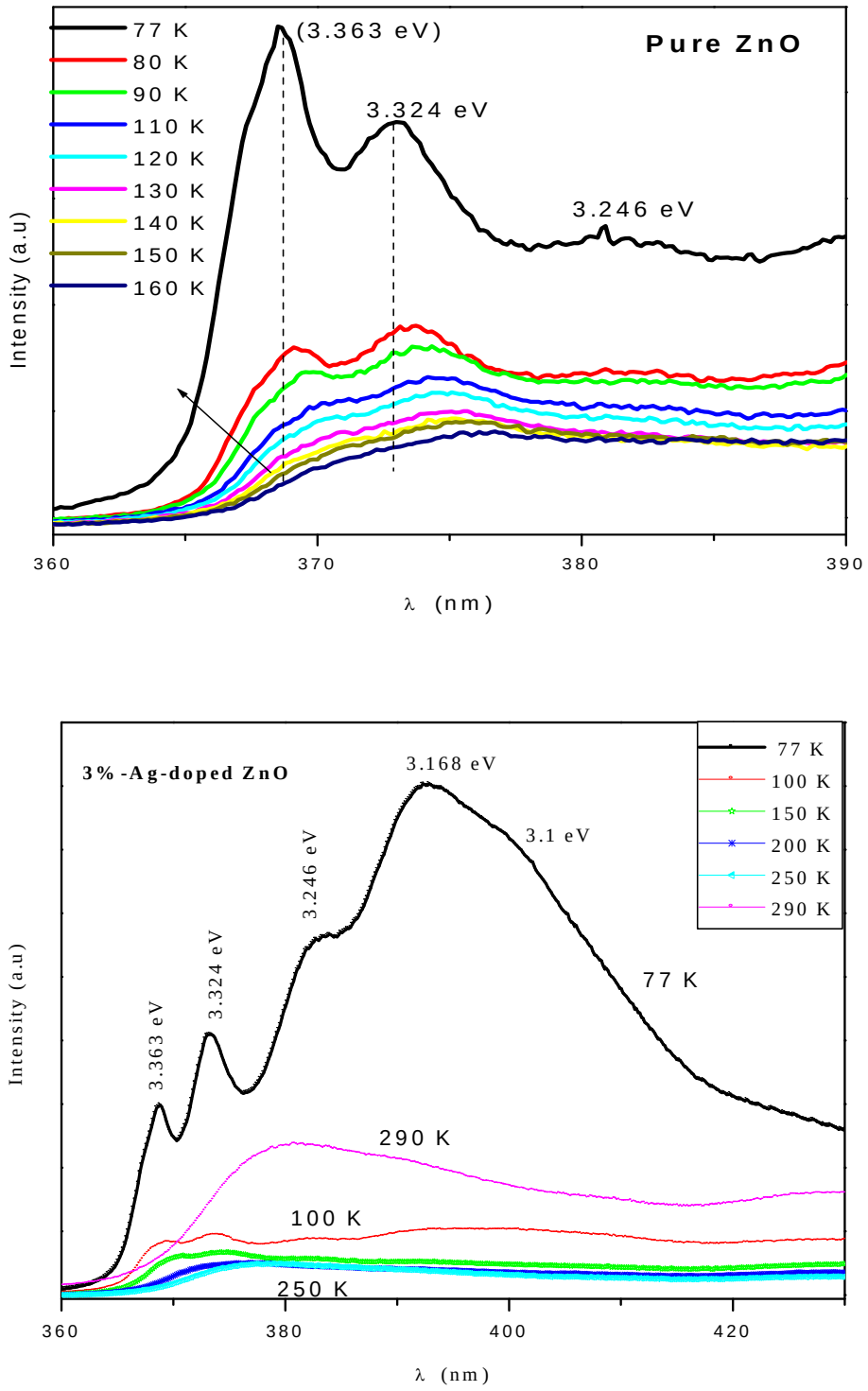

Fig. 7. Temperature dependent UV PL spectra of the undoped and 3% Ag-doped ZnO thin films.

With increasing of recorded temperature from 77 K, the intensity of the PL emission decreases, reaches a minimum at 250 K and then afresh increases for higher temperatures. This new increase of the intensity is due to the supremacy of the band-to-band emission [27].

4. Conclusions

Pure ZnO and Ag-doped ZnO thin films were synthesized by the sol–gel process and dip-coated on glass substrates. The prepared films have a ZnO hexagonal wurtzite structure; Ag ions are incorporated into the lattice of ZnO. Grain distribution in the films is homogeneous and uniform. Ag ions enhance the transparency of the film and do not affect the optical band gap. The introduction of Ag ions in the ZnO lattice strongly enhances the UV emission at the nitrogen temperature compared to the undoped samples. The UV emission decreases with increasing recorded temperature up to 250 K and then slightly increases at higher temperatures. At 77 K, BX and FX emission dominates at high and low temperatures, respectively, in the undoped ZnO sample. In Ag-doped ZnO, the most intense emission observed at 77 K is due to the 2LO optical phonon replica and the BX emission is found to be greater than the FX emission. This indicates that doping with silver enhances the BX and 2LO emissions and the peak observed at 3.168 eV is attributed not only to the 2LO phonon replica, but also to the transition of electrons from the conduction band to a defect level caused by the introduction of silver atoms in ZnO crystallites.

References

[1] S. Singh and M.S.R. Rao, Phys. Rev. B 80, 045210, (2009).
[2] F. Xian, K. Miao, X. Bai, Y. Ji, F. Chen, and X. Li, Optik 124, 4876, (2013).
[3] I. S. Kim, E. K. Jeong, D. Y. Kim, M. Kumar, and S. Y. Cho, Appl. Surf. Sci. 255, 4011, (2009).
[4] D. Djouadi, A. Chelouche, and A. Aksas, J. Mater. Environ. Sci. 3 (3),585, (2012).
[5] R. Chen, C. Zou, J. Bian, A. Sandhu, and W. Gao, Nanotechnology 22,105706, (2011).
[6] A.N. Gruzintsev, V. T. Volkov, and E.E. Yakimov, Semiconductors 37,259 (2003).
[7] H. S. Kang, B. D. Ahn, J. H. Kim, G. H. Kim, S. H. Lim, H. W. Chang, and S. Y. Lee, Appl. Phys. Lett. 88, 202108, (2006).
[8] R. Deng, Y. Zou, and H .Tang, Physica B 403 2004, (2008).
[9] I. S. Kim, E.K. Jeong, D.Y. Kim, M. Kumar, and S.Y. Choi, Appl. Surf. Sci. 255, 4011, (2009).
[10] V. S. Khomchenko, T. G. Kryshta, A. K. Savin, L. V. Zavyalova, N. N. Roshchina,
V. E. Rodionov, O. S. Lytvyn, V.I. Kushnirenko, V.B. Khachatryan, and J.A. Andraca-Adame, Superlattices Microstruct.42, 94, (2007).
[11] F. Fang, D. Zhao, X. Fang, J. Li, Z. Wei, S. Wang, J. Wu, and X. Wang, J. Mater. Chem. 21, 14979, (2011).
[12] A. Chelouche, D. Djouadi, H Merzouk, and A.Aksas, Appl. Phys. A115, 613, (2014).
[13] B. J. Jin, S. Im, and S. Y. Lee, Thin Solid Films 366 (1), 107, (2000).
[14] P. S. Xu, Y. M. Sun, C. S. Shi, F. Q. Xu, and H. B. Pan, Nucl. Instrum. Methods B 199286, (2003).

[15] K. Kim, P. C. Debnath, D. H. Lee, S. Kim, and S. Y. Lee, Nanoscale Res. Lett. 6,552 (2011).
[16] Y. Lu, X. P. Li, S. C. Su, P. J. Cao, F. Jia, S. Han, Y. X. Zeng, W. J. Liu, and D. L. Zhu, J. Lumin.152, 254, (2014).
[17] A. B. Djurisic, Y. H. Leung, K. H. Tam, Y. F. Hsu, L. Ding, W. K. Ge, Y. C. Zhong, K. S. Wong, W. K. Chan, H. L. Tam, K. W. Cheah, W. M. Kwok, and D. L. Phillips, Nanotechnology 18, 095702, (2007).
[18] C. Barret and T.B. Massalski, Structures of Metals: Crystallographic Methods, Principles and Data, Oxford, Pergamon Press, (1980).
[19] S. Singhal, J. Kaur, and T. Namgyal, Physica B 407, 1223, (2012).
[20] H. S. Kang, B. D. Ahn, J. H. Kim, G. H. Kim, S. H. Lim, H. W. Chang, and S. Y. Lee, Appl.Phys.Lett**.** 88, 202108, (2006).
[21] F. Xian, K. Miao, X. Bai, Y. Ji, F. Chen, and X. Li, Optik 124, 4876, (2013).
[22] J. Xu, Z. Y. Zhang, Y. Zhang, B. X. Lin, and Z. X. Fu, Chin. Phys. Lett. 22 **(**8), 2031, (2005).
[23] A. Teke, Ü. Özgür, S. Dogan, X. Gu, H. Morkoç, B. Nemeth, J. Nause, and H. O. Everitt, Phys. Rev. B 70, 195207 (2004).
[24] S. Singh, D. Nakamura, K. Sakai, T. Okada, and M. S. R. Rao, New J. Phys. 12, 023007, (2010).
[25] C. Li, Y. Lv, L. Guo, H. Xu, X. Ai, and J. Zhang, J. Lumin.122–123, 415(2007).
[26] T. Pauporté, E. Joanno, F. Pelé, B. Viana, and P. Aschehoug, J. Phys. Chem. C113 10422, (2009).
[27] R. Chen, C. Zou, J. Bian, A. Sandhu, and W. Gao, Nanotechnology 22, 1, 105706, (2011).

INSTALLATION AND TECHNOLOGY OF ELECTROSPARK ALLOYING OF METAL SURFACES

A. V. Rabalco and A. V. Sushyi

Joint-stock company TOPAZ factory, str. Dm. Cantemir 1, Chisinau, MD-2028 Republic of Moldova

E-mail: topaz@topaz.md

(Received August 26, 2016)

Abstract

Electrospark alloying (ESA) is a micro-bonding process capable of depositing wear-corrosion-resistant coatings to repair, improve, and extend the service life of the components and tools. During coating, short-duration electrical pulses ranging from a few microseconds to a few hundreds of microseconds are used to deposit the electrode (anode) material on the component surface (cathode) to produce a protective layer. One of the main components of installations for ESA is the current pulse source, which is responsible for technological parameters of the metal surface modification process. The data represent novel approaches to the formation of current pulses, which, in our opinion, will essentially expand the process capabilities.

1. Introduction

The TOPAZ factory started the development and production of advanced equipment for surface modification of machines and mechanism parts in order to expand the market for the factory's products. One of the fields of the realized products is manual and mechanized systems for electrospark alloying (ESA) of metal surfaces. This modification method is based on the phenomenon of erosion and polar transferring of the anode material (applied material) to the cathode (processed workpiece surface) during an electric discharge between them in a gaseous medium.

The pioneers of this method of modification of metal surfaces (elaborated simultaneously with the method of electrospark dimensional processing of metals) were Soviet scientists, married couple, USSR State Prize winners Boris Romanovich Lazarenko and Nataliya Iosaafovna Lazarenko. Academician of the Academy of Sciences of Moldova B.R. Lazarenko was the organizer of the Institute of Applied Physics and the Experimental Factory of the Academy of Sciences in Chisinau. His scientific interests ranged between theoretical and applied aspects of electrophysicochemical methods of impacting on the material. The "Moldovan school" of physicochemical methods of metal processing founded by B.R. Lazarenko allows the Topaz factory to produce machines and introduces the world-class physicochemical methods of metal processing, in particular, for ESA.

It is known that the pulse current parameters and the physicochemical properties of the electrodes and interelectrode materials of the gaseous medium determine the following technological features and the properties of the resulting coatings: mass loss of the anode, mass

received by the cathode, gradient depth values of hardening effects in the near-surface coating area, residual stress level, coating thickness, etc.

An indispensable feature of the ESA method is the implementation of sparks between the electrodes. A spark must accompany each current pulse at any given time. Analysis of the current state in the field of the manufactured equipment for ESA revealed a number of shortcomings in the capabilities of the existing current generators; some of them are as follows [1, 2]:

—Reduction in the integrated electrical power applied to the interelectrode spark gap per unit time upon switch to a precision ESA mode due to the lack of possibility to compensate for its decrease by a corresponding increase in the pulse repetition frequency (its frequency is hardly set by limit characteristics of electromagnetic vibrators).

—Reduction in the amount of energy passing through the spark discharge in the case of using current pulses of long duration in connection with the short-circuiting of the spark channel by colliding electrodes (only a portion of the current pulse is accompanied by a spark discharge).

—Reduction in the amount of sparks in the total number of pulses upon switch to a precision mode because of the inability to provide an explosion of volume of contact microroughnesses under conditions of colliding electrodes (typically, the switch to precision modes is achieved through a decrease in the spark pulse energy by reducing the discharge voltage of the capacitor).

The foregoing had defined features of the ideology of construction of the current pulse generator developed by TOPAZ which were aimed at excluding the above-described disadvantages in the implementation of the ESA method. Simultaneously, activities focused on imparting new capabilities to the current pulse generator, and hence the technological process, were conducted. Let us explain some of the approaches in achieving these aims.

2. Results and discussion

One of the main objectives of the organization of high-performance process of coating modification by the described method (including new technological capabilities) is the possibility to organize a spark channel at any given time. Therefore, in the design of systems for ESA, it was necessary to reject the idea of formation of a spark channel by collision of the tool-electrode and the workpieces using an electromagnetic vibrator. Hence, there were limitations in the implementation of the electrospark coating formation, especially using high-precision alloying modes (high-frequency regimes of alloying at low pulse energies). The limitations are attributed to the impossibility of organizing the high-frequency operation of electromagnetic vibrators. Moreover, there was no possibility of using pulse groups with different parameters of current pulses and pauses between them to implement additional properties of the process (e.g., a group of six to eight 1-ms pulses).

In view of the above, we proposed to use an electromagnetic vibrator to provide continuous sliding of the tool-electrode over the workpiece surface, i.e., maintain an electrical contact between them throughout the entire alloying process, rather than to implement periodic mutual collisions of the electrodes [2, 3].

The experimental results confirmed the possibility of the designed equipment to increase the productivity, while traversing the area subjected to alloying, especially for alloying with small quantities of electrical energy pulses. Enhancement of the performance was not only due to an increase in the pulse repetition frequency by using ESA with the tool-electrode sliding along the workpiece surface, but also by reducing the proportion of pulses with a full short circuit

caused by the collision of the counter electrodes. At the same time, the implementation of the tool-electrode oscillations on the workpiece surface also opens an ample possibility of rapidly exposing to the ESA process using bursts of pulses with different electrical parameters and with controllable duration pauses between the pulses in group. It was found that this approach to implementing the process significantly changes the patterns of electrode erosion and polar transfer of the material of the tool-electrode to the workpiece and thus the surface properties of the workpieces.

To organize the ESA process using groups of pulses with different parameters, a special current generator has been developed at the Topaz factory. It is based on the idea of formation of parameters of an individual pulse (as well as their sets in groups) by the parallel–serial superposition of individual pulses from several independent discharge contours. In the developed generator, the number of these contours (in which current switching is carried out by powerful transistors) can be six and more (depending on production engineering demands). Figure 1 shows current oscillograms to illustrate some possibilities of energy release in the spark gap for both an individual current pulse (one contour) and a group of pulses from different contours with different capabilities in the technological circuit design.

With the parallel–serial addition of current pulses (using the example of three contours), it is possible to obtain varied parameters of duration and amplitude of the total current pulses (Figs. 1a–1d). In the case of the parallel simultaneous addition of pulsed currents, for example, three contours, it is possible to obtain the total momentum of a half sinuous current with a 1300-A current amplitude at a pulse duration at the base of 85 μs (Fig. 1e).

Application of pulse-width modulation can significantly enhance the capacity of each generator circuit in terms of the energy parameters per pulse, including its form.

It is also possible to organize modes with an increased mass erosion transfer from the anode to the cathode as a result of aggregate discharges collected in a burst for a given program. Research of the mechanism of mass transfer caused by exposure to sparks under these conditions revealed the possibility of increasing the mass transfer by a factor of 1.5 and more with unchangeable parameters of total energy spark discharges (e.g., alloying of steel 35–40 samples using a high-strength tungsten–cobalt tool-electrode). Investigation of the laws of formation of the coating surface under high mass transfer conditions revealed the necessity to implement electroerosion smoothing in one process step. This objective was accomplished by introducing additional pulses per burst. Figure 2 shows an oscillogram of pulse bursts consisting of a current pulse responsible for the organization of mass transfer and two pulses for the implementation of spark erosion grinding.

The average current of the pulse generator remains the same for all technological regimes of ESA. Its value was based on the conditions of restrictions on the thermal regime of the tool-electrode (the absence of the contact zone overheating). Thus, the cross-sectional area size of the tool-electrode was selected on the basis of convenience of the alloying process visualization. For example, for the processing of a BK8 alloy electrode on an area of 8 mm^2, the average current is 3 A. In the case of necessity of changing the processing area of the electrode in the lower side, regimes of the generator work at an average current of 2 and 1 A are provided without changing the energy release in a pulse mode or in their totality (bursts). The possibility of delivery of a single pulse (or single burst) in the interelectrode gap is also implemented to study the spatial resolution of erosive spots, which are necessary to generate sweep programs for effects from discharges in the case of a mechanized deposition process.

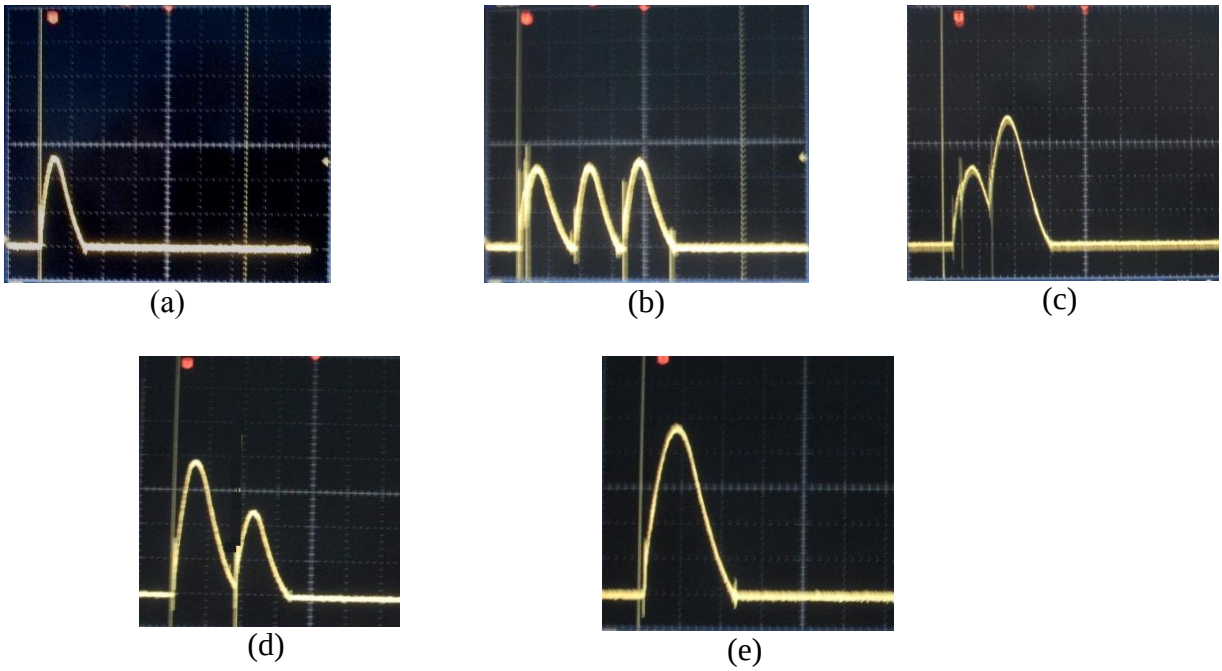

Fig. 1. Current oscillogram illustrating the possibilities of the superposition of sine-wave current of the individual circuit pulse generator: (a) one contour; (b) three contours, the currents of which are connected sequentially in time; (c) three contours, the first two currents are stacked sequentially in time, the third current is set parallel to the second folded and simultaneously with it in time; (d) three contours, the two first currents are set simultaneously, the third current is connected in series and in time after the end of the sum current of the first two contours; and (e) three contours, the currents of which are connected simultaneously. The scale interval is 265 A/Cage (C) along the vertical axis (current) and 40 μs/C along the horizontal axis (time).

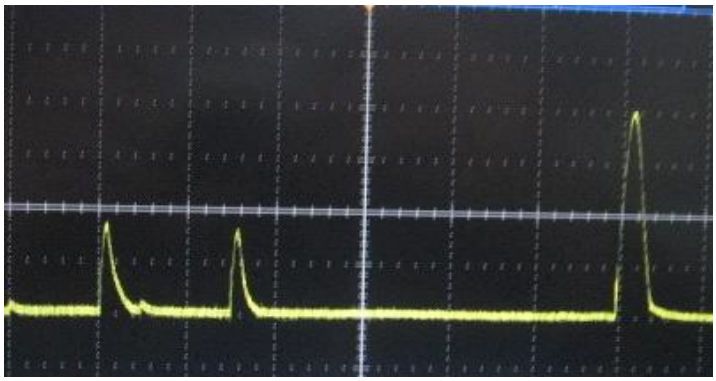

Fig. 2. Current oscillogram illustrating possibilities of transferring bursts of three sine-wave pulses in which the first two perform the electroerosion smoothing, the third provides the base layer coating. The scale interval is 265 A/C along the vertical axis (current) and 40–200 μs/C along the horizontal axis (time).

The generator is governed by a special programming device controlled by a human-machine interface imparting the above specified individual features to the technological process of electrospark modification of metal surfaces. These features are imparted by a change in pulse durations and pauses between each contour and the necessary time delays at various current superpositions of different contours.

References

[1] A. V. Rabalco, D. M. Griciuc, C. R. C. Somaraju, and O. Sahin, Elektron. Obrab Mater. 5, 133, (2000)
[2] A. V. Rabalco, D. M. Griciuc, and O. Sahin, Elektron. Obrab. Mater. 2, 16, (2001)
[3] A. Rabalco, D. Griciuc, V. Ermilov, and O. Sahin, MD Patent 1414, 2000.

EFFICIENT LOW-COST SOLAR CELLS BASED ON ITO–*n*Si

N. Curmei

Institute of Applied Physics, Academy of Sciences of Moldova,
Academiei str. 5, Chisinau, MD-2028 Republic of Moldova.
Email: ncurmei@gmail.com

(Received April 11, 2016)

Abstract

A vapor phase pyrolysis deposition (VPPD) method has been described in [1] and applied to prepare indium tin oxide (ITO) thin films with thicknesses about 400 nm, with a conductivity of $8.3 \cdot 10^3\ \Omega^{-1}\ cm^{-1}$, and a transparency of 80% in the visible spectral range. The layers have been deposited on the (100) surface of the *n*-type Si wafers with a concentration of $10^{15}\ cm^{-3}$, and their morphology has been examined. The as-deposited ITO thin films consist of crystallites with a height of 300–400 nm and a width of 100–200 nm. Properties of low-cost Cu/ITO/SiO_2/*n*-Si/n^+Si/Cu solar cells fabricated by depositing ITO layers on *n*-Si wafers have been studied. The maximum efficiency has been found to be 13.8%.

1. Introduction

Today, an optimum way of a direct conversion of solar energy into electricity is to resort to solar cell (SC) devices. This approach is an ecologically friendly method of using renewable energy sources. However, a widespread application of photovoltaic converters is hampered by their relatively high cost. To solve this problem, it is necessary to develop methods based on easier-preparation processes at lower temperatures compared to those in the manufacturing conventional photovoltaic devices based on *p*-*n* junctions. One of these methods is the utilization of SC based on semiconductor–insulator–semiconductor (SIS) structures, which can be easily implemented by the deposition of a transparent conductive oxide (TCO) layer on the surface of "solar" semiconductors. A thin insulator layer at the oxide–semiconductor interface is mostly formed during the TCO deposition for which a variety of techniques are applied. Among them, the spray pyrolysis deposition method is of a particular interest due to its simplicity, moderate preparation temperatures, high deposition rates, and vacuum-less conditions [2]. The TCO films with a band gap on the order of 3.3–4.5 eV are transparent in the entire region of the solar spectrum, including the blue and ultraviolet regions. In SC the TCO layer contributes also to the collection of separated charge carriers and, at the same time, it acts as an antireflection coating. In the SC fabrication, the most frequently used TCO materials are tin dioxide (SnO_2), indium oxide (In_2O_3), and their mixture known as indium tin oxide (ITO). Namely, ITO thin films have been applied for the first time for the preparation of Si-based SIS structures [3]. A detailed review of the development of the SC based on ITO/*n*-Si structures is presented in [4]. The theoretical analysis of energy losses in ITO/*n*-Si based SC has shown that their conversion efficiency depends on the thickness and structure of the insulating layer at the TCO–semiconductor

interface as well as on the substrate doping level, concentration of surface states, oxide electric charge, and temperature. The optimization of these parameters could result in a device efficiency of about 20% [5]. However, the reported efficiencies do not exceed 13% [4].

The aim of the present work is to study the structure of the ITO–Si interface, increase the conversion efficiency of Si-based SIS solar cells with the ITO thin film transparent emitter, and simplify the fabrication process for obtaining low-cost Cu/ITO/SiO_2/*n*-Si/n^+Si/Cu solar cells with an efficiency close to 14%.

2. Experimental

2.1. Preparation of ITO thin films and ITO/n-Si structures

ITO thin films were deposited at 450°C on the *n*-Si (100) wafer surface by spraying an ethanol solution of $InCl_3$ and $SnCl_4$ in a ratio of 10:1 using compressed oxygen. The following chemical reactions take place on the heated substrate:

- $4InCl_3 + 3O_2 = 2In_2O_3 + 6Cl_2$
- $SnCl_4 + O_2 = SnO_2 + 2Cl_2$ (1)

In our earlier studies, ITO thin films were deposited in a setup using direct spray pyrolysis [6]. In the present work, the ITO layers were prepared by a specially developed Vapor Phase Pyrolysis Deposition (VPPD) method for a conformal coverage of the Si wafer surface. The VPPD technique was implemented by upgrading the spray pyrolysis setup presented in [7]. A special emphasis was made on a further development of the spray pyrolysis deposition method in order to obtain a more refined aerosol with the properties of a vapor flux. In the proposed VPPD setup (Fig. 1), the solution is sprayed first into a glass tube with a labyrinth of obstacles for a better dispersion and purification from large size droplets. Hence, a flux of solution vapors, rather than a flux of dispersed droplets, comes on the substrate surface. In addition, the vapor flow is in a wider range and can be better controlled. Polycrystalline ITO films with a columnar structure of the ITO crystallites were obtained. The crystallites show a width of 100–200 nm and a height of up to 400 nm, being thus comparable with the film thickness.

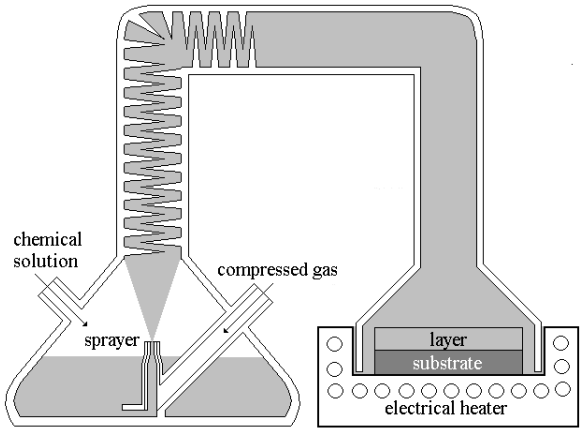

Fig. 1. Schematic drawing of the VPPD setup.

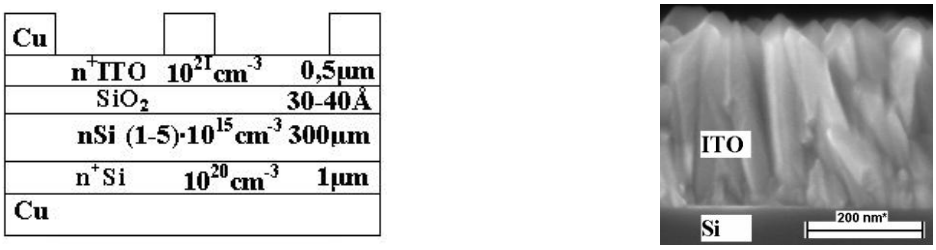

(a) (b)

Fig. 2. (a) Schematic image of the fabricated ITO/SiO_x/nSi and **(b)** its cross section

For ITO layers deposition and ITO/*n*-Si structure obtaining, *n*-Si (100) oriented wafers with a resistivity of 4.5 Ω cm were used as substrates. The surface treatment of silicon wafers (in all cases, it was the polished side of the plate) was carried out, without the traditional RCA treatment, in the following sequence: degreasing with a NH_3 solution heated to 70–80°C: H_2O_2:H_2O (1 : 1 : 8) for 15–20 min; processing in hydrofluoric acid for 2 min; rinsing in distilled water and holding at a temperature of 450°C for 10 min immediately prior to the ITO deposition. The as-obtained ITO/*n*-Si structure was the base for the SC fabrication, which ends by the deposition of a Cu grid contact on the front side of the SC and a Cu continuous contact on their rear side. The schematic image of the fabricated Cu/ITO/SiO_2/*n*-Si/n^+Si/Cu solar cell and the cross section of this structure are presented in Figs. 2a and 2b, respectively. The thicknesses of their component layers and the values of the substrate electrical parameters are also presented there.

It should be noted that the spray pyrolysis is a non-vacuum low temperature method for ITO layers deposition, which can be considered as a promising approach for the low-cost effective processing of SC based on ITO/*n*-type Si structures. To achieve this goal, it is necessary to determine and adjust the optimum preparation parameters of the ITO layer, the thickness of the insulator SiO_2 layer and, especially, the Si wafer surface state.

The thickness of the front ITO layer can be adjusted for an antireflection condition coating. At the same time, it should be taken into account that the thickness of this layer determines its electrical resistance and therefore affects the magnitude of the photocurrent. High values of open circuit voltage and conversion efficiency may be achieved by the formation of a SiO_2 insulator layer with the thickness allowing obtaining a maximum potential barrier height and a minimum saturation current at the ITO/Si interface. At the same time, the SiO_2 insulator layer must be tunnel transparent for the charge carrier transport; therefore, the optimal SiO_2 layer thickness must not exceed a few tens of Angstrom. In addition, it is also necessary to select the optimal Si wafer thickness for a better match to the carrier collection length.

2.2. Characterization methods

The crystallographic structure of the ITO thin-films was studied by X-ray diffraction using an X'PERT-MPD (Philips) diffractometer using CuK_α radiation (1.5405 Å). The K_β component was eliminated by using a Ni filter. The morphology of the ITO layers was investigated by scanning electron microscopy (SEM) using a TESCAN VEGA microscope. The chemical composition of the films was studied in the same SEM microscope by an integrated

INCA energy dispersive X-ray EDX analysis system. Measurements of the thickness and surface morphology of SiO_2 films were performed using a scanning probe microscope (SPM) and an atomic force microscope (NTEGRA Aura, NT-MDT).

Photovoltaic parameters of the SC devices, i.e., short-circuit current density (J_{sc}), open-circuit voltage (U_{oc}), fill factor (FF), and efficiency (Eff.) were determined from the illuminated current–voltage characteristics under standard test conditions. The simulated sunlight was obtained using a Telecom STV sun tester with a Philips 1000W Xe arc-lamp and an AM1.5 filter. The light source was calibrated to 100 mW/cm^2 using a calibration cell.

3. Properties of ITO–*n*Si heterostructures

3.1. Electrical properties

In all types of heterostructures, the mechanism of charge carrier transport through a barrier strongly depends on the interface status, which, in its turn, is determined by the chemical and thermal treatment of contacting surfaces of semiconductor materials. In particular, in the case of structures of the type oxide semiconductor/semiconductor, for example, ITO/*n*-Si, the quality of the interface is heavily dependent on the surface state of the silicon wafer. Before the ITO layer deposition, the Si surface could be degreased and etched, as described in [8], or without etching, as in the present paper. Dark current–voltage characteristics in a temperature range of 293–413 K have been studied in both cases. The general behavior of the *I–U* curves of directly biased devices investigated in [8] is characterized by the presence of two straight-line regions with different slopes. In the first region, at external voltages lower than 0.3 V, the *I–U* curves are parallel; that is, their slope is constant. In this way, two mechanisms of the direct current flow are observed: (i) tunneling recombination at direct voltages of less than 0.3 V and (ii) over barrier emission at voltages higher than 0.3 V. In the former case, the direct current flow could be interpreted as multistep tunnel recombination transitions of electrons from the silicon conduction band into the ITO conduction band. For structures without etching Si surface, which are studied in the present paper, Fig. 3a shows that, for the samples of the same type at the applied voltages corresponding to the straightening of the band and the disappearance of the potential barrier, the slopes of the *I–U* dependences do not differ. The mechanism of the charge carrier transport through the barrier corresponds to the model [9], according to which the transfer of charge carriers is the tunneling through the potential barrier and recombination transitions in the space charge region. Thus, the current–voltage characteristic can be described by the following equation:

$$I = I_o \exp(AU) \exp(BT) \qquad (2)$$

where *A* and *B* are constants independent of voltage and temperature, respectively.
The values of factors *A* and *B* calculated for the curves presented in Fig. 3a in the case of voltages less than 0. 6 V are 14 V^{-1} and 0.05 K^{-1}, respectively.

In this case, the feature of the mechanism does not correspond to the charge carrier transport over the barrier. The observed fact can be explained by the presence of a thin oxide layer at the ITO/Si interface obtained on the silicon surface during the manufacture of the structures (Fig. 3b).

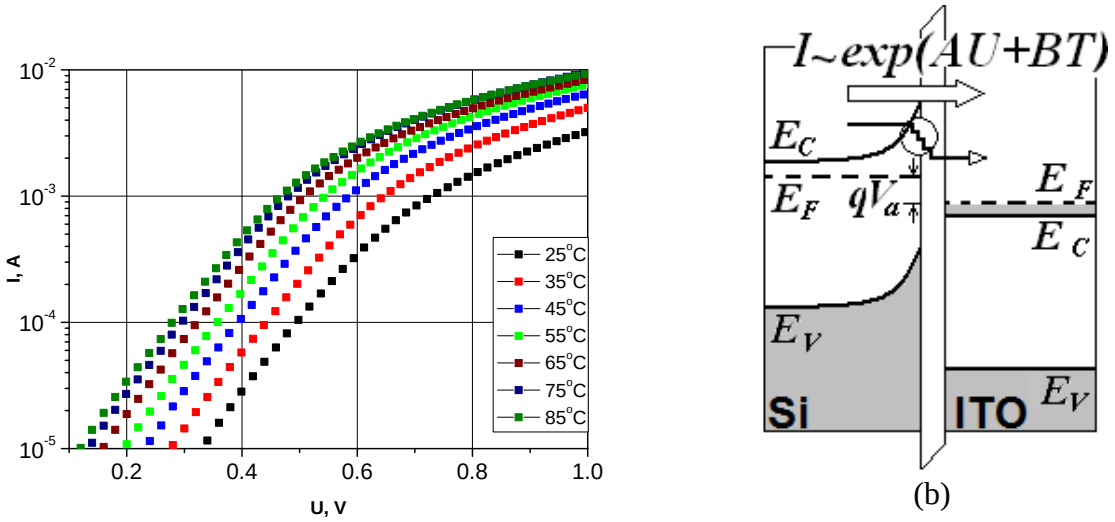

Fig. 3. (a) Dark *I–U* characteristics (low-temperature anneals) and **(b)** band diagram of ITO/*n*-Si heterostructures.

The mechanism of the charge carrier transport through the barrier for the ITO/Si heterostructures obtained by ITO layers deposition on non-etched Si wafers surface corresponds to the mechanism from the first region of ITO/*n*-Si structures obtained in [8].

At voltages higher than the diffusion potential of 0.6 V, the current flow for all types of samples is determined by the Ohm law.

3.2. Photoelectrical properties

The photoresponse of these structures (see Fig. 4) was observed in the energy range corresponding to the energy values of the widths of the silicon and ITO bands gap.

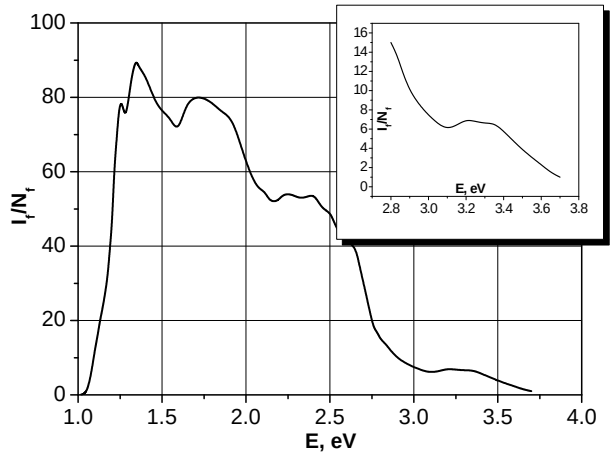

Fig. 4. Spectral distribution of photosensitivity of Cu/ITO/SiO_2/*n*-Si/n^+Si/Cu structures.

In fact, the energy of the incident light flux higher than 1 eV leads to the beginning of light absorption in silicon and the generation of electron–hole pairs. The pairs are separated by the junction electric field; as a result, the appearance of an electrical signal is observed. At the

luminous flux of energy of 3.7 eV, when the light is already absorbed in a very narrow layer near the frontal surface in ITO, the photoresponse disappears due to an intense recombination of nonequilibrium charge carriers. The insert in Fig. 4 shows an enhanced photosensitivity of Cu/ITO/SiO_2/*n*-Si/n^+Si/Cu photovoltaic cells in the ultraviolet region of the spectrum.

The load *I–U* characteristics of the obtained Cu/ITO/SiO_2/*n*-Si/n^+Si/Cu solar cells measured in different radiation power (*W*) conditions in a range of 100–1000 W/m^2 are presented in Fig. 5. From these data, the dependences of short-circuit current I_{sc} and open-circuit voltage U_{oc} on the radiation power values has been calculated. A linear $I_{sc} = f(W)$ dependence and a logarithmic $U_{oc} = f(W)$ dependence were found, which is typical for all *p–n* junctions.

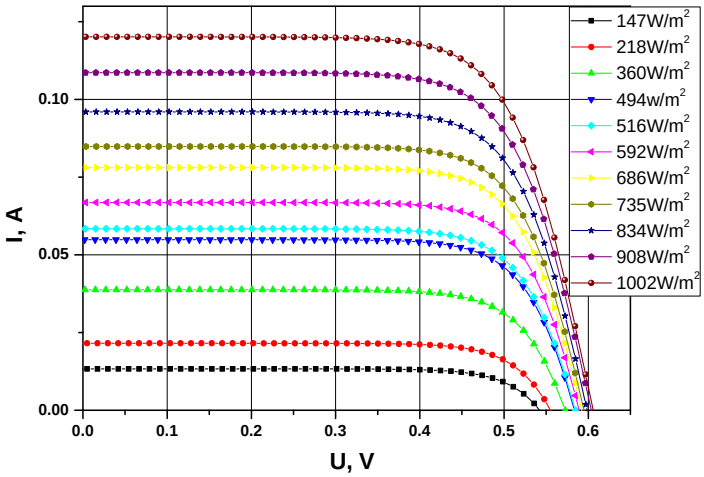

Fig. 5. Load *I–U* characteristics of Cu/ITO/SiO_2/*n*-Si/n^+Si/Cu SC under different radiation power conditions.

It is clear from Fig. 5 that, at 147 W/m^2, the following photoelectrical parameters values were obtained: short-circuit current density of 3.59 mA/cm^2, open-circuit voltage of 541 mV, fill factor of 0.76, and efficiency of 10.06%. An increase in *W* to 1000 W/m^2 leads to the following values: short-circuit current density of 32.46 mA/cm^2, open-circuit voltage of 606 mV, fill factor of 0.70, and efficiency of 13.80%. These data have been obtained for a cell with an active area of 6 cm^2.

4. Conclusions

(1) Technological conditions for non-vacuum manufacturing of MIS type efficient low-cost Cu/ITO/SiO_2/*n*-Si/n^+Si/Cu solar cells have been elaborated. Photovoltaic devices with efficiencies of up to 14% have been fabricated using the VPPD method.
(2) It has been found that the most effective Cu/ITO/SiO_2/*n*-Si/n^+Si/Cu solar cells are obtained without etching the silicon substrates oriented in the (100) plane in HNO_3 : HF.
(3) The spectral distribution of the photosensitivity of ITO/SiO_2/*n*-Si structures covers a wide range of energies (1.1–3.7 eV), particularly the ultraviolet range of the spectrum of solar radiation.

Acknowledgments. This research was carried out in the framework of STCU project 5985 and Institutional Project CSSDT 15.817.02.04A whose support is acknowledged.
The author thanks Dr. Olga Iliasenco for technical assistance in preparing this manuscript.

References

[1] A. Simashkevich, D. Serban, L. Bruc, N. Curmei, V. Hinrichs, and M. Rusu, Thin Solid Films, (2016), doi:10.1016/j.tsf.2016.04.047, (accepted for publication)
[2] C. G. Granqvist and A. Hultaker, Thin Solid Films 1, 411, (2002).
[3] J. B. DuBow. D. E. Burk, and J. R. Sites, Appl. Phys. Lett. 29 (8), 494, (1976).
[4] A. Simashkevich, D. Serban, and L. Bruc, Chapter in the Book "Solar cells – silicon wafer-based technologies". Ed. L. Kosyachenco, InTech, 2011, 364 p.
[5] J. Shewchun, D. Burk, R. Singh M. Spitzer, and G. Dubow, J. Appl. Phys. 50 (10) 6524, (1979).
[6] A. Simashkevich, D. Serban, L. Bruc A. Coval, V. Fedorov, E. Bobeico, and I. Usatii, Proc. of the 20th European Photovoltaic Solar Energy Conference, (Barcelona) 980, (2005).
[7] W. Badawy, F. Deckert, and K. Doblhofer, Solar Energy Mater. 8, 363, (1983).
[8] A. Simashkevich, D. Sherban, M. Rusu, L. Bruk, and Iu. Usatii, Proc. of the 24th European Photovoltaic Solar Energy Conference, (Hamburg), 2230, (2009)
[9] A. R. Riben and D. L. Feucht, J. Electr. 20, 583, (1966).

PREPARATION OF CAST GLASS-COATED AMORPHOUS MAGNETIC MICROWIRES

S. A. Baranov[1,2]

[1]*Institute of Applied Physics, Academy of Sciences of Moldova,*
Academiei str.5, Chisinau, MD-2028 Republic of Moldova
E-mail: baranov@phys.asm.md
[2]*Departament de Genie Physique, Ecole Polytechnique de Montreal,*
C.P. 6079, succ. Centre-ville, Montreal H3C 3A7, (Quebec) Canada
E-mail: sabaranov07@mail.ru

(Received January 13, 2016)

Abstract

Technological aspects of the Ulitovsky–Taylor method for the preparation of glass-coated microwires with different structure of metallic cores are analyzed. The residual stress distributions in microwires of this type determine the domain structures. The residual stress in cast amorphous micro- and nanowires is studied.

1. Introduction

Cast glass-coated ferromagnetic amorphous microwires (CGCFMWs) are known to exhibit good magnetic properties. CGCFMWs are composite materials that consist of a metallic core and a glass coating. The glass-coating induces strong residual stress in the core. This residual (mechanical) stress affects the magnetostriction value that is determined by large magnetoelastic anisotropy.

The magnetic properties of CGCFMWs are determined by the composition, which gives the sign and magnitude of their magnetostriction, and by dimensions, i.e., metallic core diameter, glass-coating thickness, and their ratio, which are extremely relevant for the level of residual stresses induced during preparation. The magnetomechanical coupling between residual stresses and magnetostriction is mainly responsible for the distribution of anisotropy axes and domain structure formation.

2. Preparation by the Ulitovsky–Taylor method

CGCFMWs are one of the families of the amorphous materials which now are attracting growing interest due to magnetic properties and promising technological applications. A simple technology of production was first introduced in 1924 by Taylor, after whom this method is named [1–5]. Later (1950–1964), this method was significantly improved by Ulitovsky in order to produce large amounts of these microwires [3–5].

The preparation of cast glass-coated amorphous magnetic microwires by the Ulitovsky–Taylor method and the study of the magnetic properties thereof were reported in [1–14]. Amorphous microwires produced by the "in-rotating-water quenching" method have distinctive magnetic properties since they have different magnetic domain structures [7].

Technological aspects of the Ulitovsky–Taylor method for the preparation of CGCFMWs with different structure of metallic core are analyzed below (Figs. 1–3).

In the process, a few grams of the master alloy with a desired composition is placed inside a Pyrex-like glass tube placed directly within a high frequency inductor heater (Fig. 2). The alloy is heated up to the melting point to form a droplet. The portion of the glass tube adjacent to the melting metal softens and envelopes the metal droplet. After that, a glass capillary is drawn from the softened glass portion and wound on a rotating coil (Fig. 1).

Parameters of critical quenching rates for the preparation of a metastable, amorphous, or supersaturated state are 10^4–10^7 K/s.

Under suitable drawing conditions, the molten metal fills the glass capillary and a CGCFMW is thus formed where the metal core is completely coated with a glass shell (Fig. 3).

The microstructure and, hence, properties of the CGCFMW mostly depend on the cooling rate, which can be controlled by a cooling mechanism where the metal-filled capillary enters into a stream of a cooling liquid (water or oil) on its way to the receiving coil.

The properties of the microwire are largely attributed to the microstructure of the metal core. The casting analysis method offers the possibility of rapid cooling and solidification of the liquid metal in a nonequilibrium process allowing the formation and existence of metastable metallic phases. The microstructure of the rapidly cooled metal depends on the chemical composition and melting temperature of the metal and the cooling rate. Depending on the critical cooling rates, different metastable phases can be formed: a supersaturated solid solution, microcrystalline and amorphous phases.

The main advantages of this method for the preparation of CGCFMW are as follows [1–5, 10–14]:

- ✓ The preparation of continuous long pieces of a microwire of up to 10^4 m.
- ✓ Wide range of variation in parameters. (Geometrical: typical metallic core diameter *d* of 0.5–70 μm; glass coating thickness of 1–50 μm).Control and adjustment of geometrical parameters (inner metal core diameter *d* and glass thickness) during preparation.
- ✓ The presence of a vacuum machine to vary the pressure inside the Pyrex tube in order to control metallic core diameter *d.*
- ✓ Reproducibility of the microwire properties in mass production.

The main technological parameters for the preparation of glass-coated microwires are presented below.

The geometrical characteristics of the microwire depend on the physical properties of the glass and the metal, the diameter of the initial glass tube, and the parameters of the heating inductor.

According to previous analysis, the most significant effect on the geometry of a microwire comes from the glass properties. Wire radius R_g is estimated as follows:

$$R_g \sim A\frac{\eta^{2-k}}{V_d^{\,k}\sigma_s^{\,1-k}}, \qquad A \sim \frac{1}{\rho}, \tag{1}$$

where k is the parameter dependent on casting rate ($0 < k < 1$); ρ is the density (wire); V_d is the casting rate; σ_s is the surface tension (glass); and η is the dynamical viscosity (glass):

$$\eta \sim \eta_o \exp\{\frac{\Delta H}{kT} + c[\exp(\frac{\varepsilon}{kT}) - 1]\}, \quad (2)$$

where $\varepsilon \sim 2 \cdot 10^2$ kJ/mol; $\Delta H \sim 10^2$ kJ/mol; and η_0, c are material constants.

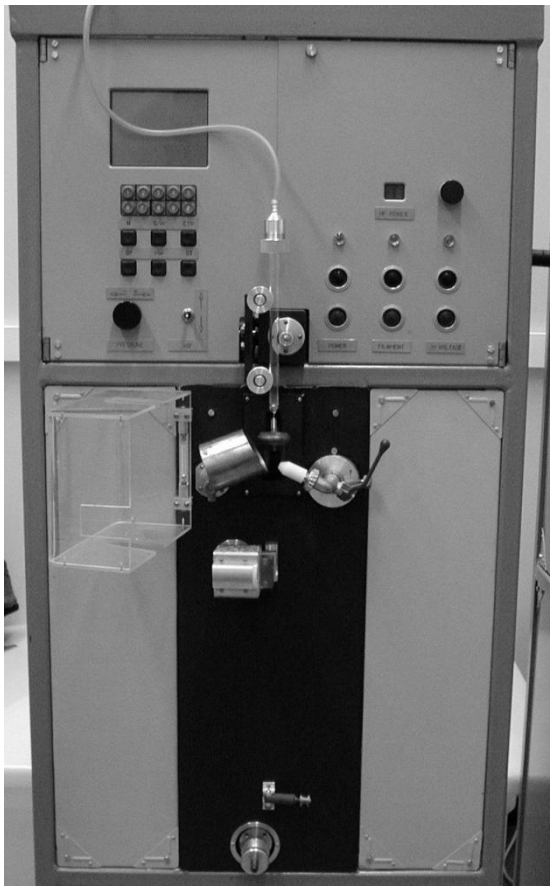

Fig. 1a. Machine for the preparation of CGCFMWs by the Ulitovsky–Taylor method (produced at AMOTEC Ltd, Moldova).

Fig. 1b. Novel machine for the preparation of CGCFMWs by the Ulitovsky–Taylor method (produced at MFTI Ltd, Moldova).

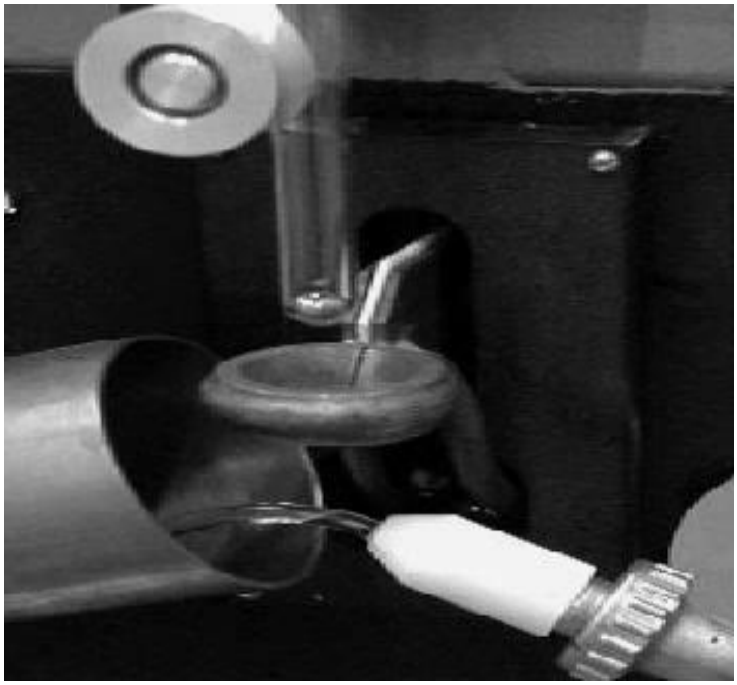

Fig. 2. Image of the microwire preparation process using the Ulitovsky–Taylor method.

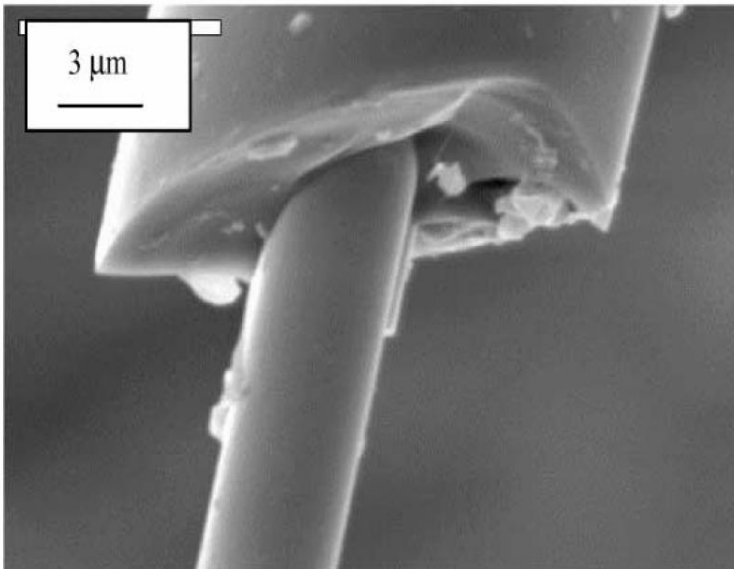

Fig. 3. Cast glass-coated ferromagnetic amorphous microwire (CGCFMW).

According to [10, 11]:

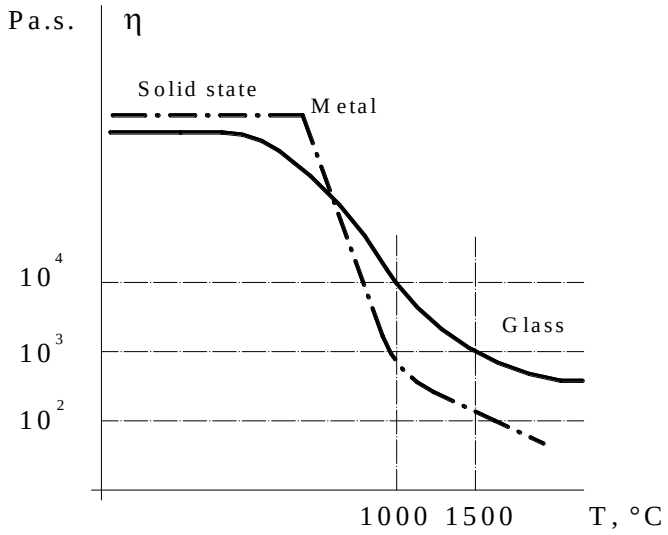

Fig. 4. Viscosity η as a function of temperature. The temperature region where the casting process can be implemented is indicated by dashed lines.

Formula (1) suggests the following. If the casting rate is extremely low, the R_g value is high. We obtain a formula similar to that in [10, 11]:

$$R_g \sim \frac{\eta^{5/3}}{\sigma^{2/3} V^{1/3} \rho} \quad , \tag{3}$$

where $k = 1/3$.
If the casting rate is sufficiently high, we obtain for R_g [10, 11]:

$$R_g \sim \frac{\eta^{4/3}}{\sigma^{1/3} V^{2/3} \rho} \tag{4}$$

where $k = 2/3$.

We obtain the theoretical limit of extremely high casting rates where $k \to 1$:

$$R_g \sim \frac{\eta}{V \rho} \tag{5}$$

Particular attention is paid to parameters determining the casting and cooling rates that are responsible for the microstructure of as-cast microwires (amorphous or microcrystalline).

3. Residual stresses

It was shown in [6–9, 12–14] that significant residual stresses occur inside the metallic core and glass coating as a consequence of the difference in thermal expansion coefficients of the

metal and the glass. The value of these stresses depends on ratio x between metallic core diameter $d = 2r_m$ and total microwire diameter $D = 2R_g$:

$$x = (D^2/d^2 - 1) \tag{6}$$

$$\sigma_r = \sigma_\phi \equiv P_\nu ,$$

where

$$P_\nu = \sigma_0 \frac{kx}{[k[1-2\nu]+1]x + 2[1-\nu]}, \tag{7}$$

If the Poisson coefficient is $\nu = 1/3$, then

$$\sigma_r = \sigma_\phi \equiv P = \varepsilon E_1 \frac{kx}{[k/3+1]x + 4/3}, \tag{7a}$$

and

$$\sigma_z = P \frac{[k+1]x + 2}{kx + 1}, \tag{8}$$

where $\sigma_0 = E_1 (a_1 - a_2) (T^* - T)$, k is the ratio of Young's moduli, $k = E_2/E_1 = 0.3 - 0.6$.
Numerical calculation indicates that, for small values of x, the $\sigma_z(x)$ dependence is nearly linear and exhibits saturation (up to 1 GPa) approximately at x = 10 [6–9, 12–14].

In terms of the model used for the stress formation in the microwire, the microwire strand preserves liquid status from its axis to internal radius b, while it freezes earlier from b to metallic core radius R, and only elastic residual stresses persist.
So, if

$$b < r < R ,$$

this model gives

$$\sigma_r = P_1' - \frac{c_1}{r^2}, \qquad \sigma_\varphi = P_1' + \frac{c_1}{r^2}, \tag{9}$$

The conditions of peak stresses on the strand surface, which can be estimated from (6)–(8), assume the boundary conditions. The numerical calculations suggest that the residual stresses for the CGCMNW decrease in the succeeding layers (in absolute magnitude), while remaining tensile. Analytical dependences of the residual stresses on the cylinder radius coordinate are important for calculation of the domain wall (DW) width. They are presented (according to [6–9, 12–14]) in the following form:

$$\sigma_{r(1)} \approx P\left[1-\left(\frac{b}{r}\right)^2\right],$$
$$\sigma_{\varphi(1)} \approx P\left[1+\left(\frac{b}{r}\right)^2\right], \quad (10)$$

In addition, at $r < b$, this model gives

$$\sigma_{r(2)} = 2K \times \ln\left(\frac{r}{b}\right), \quad (11.a)$$

$$\sigma_{\varphi(2)} = 2K \times \left[1+\ln\left(\frac{r}{b}\right)\right], \quad (11.b)$$

$$\sigma_z = \nu[\sigma_r + \sigma_\varphi], \quad (11.c)$$

where K is the thermoelastic constant [6–9, 12–14] and ν is the Poisson's coefficient. Note that a rigorous solution should be obtained by lacing equations (10) and (11a,b) at $r = b$ and taking into consideration the fact that they are unacceptable at $r = 0$; also note that $\sigma_r < \sigma_\varphi$ for any r.

4. Conclusions

In the preparation of cast glass-coated amorphous microwires, the residual stresses increase from the axis attaining maximum values on the surface. We have written a simple analytic expression for the switching field dependence on residual stresses, the radius of the metallic core of the microwire, the magnetostriction constant, and temperature; it has been experimentally verified. The macroscopic mechanism of domain wall activation qualitatively explains the main switching field dependence as an exponential form of temperature.

Theory of thermoplastic relaxation can be used to show that residual stresses will increase on the surface of a microwire, which corresponds to the previously obtained experimental data.

Cast glass-coated amorphous microwires exhibit residual magnetization due to the specific distribution of residual stresses. This property of microwires can be used for designing long-term magnetic storage elements and other electronic devices.

The main technological parameters for the preparation of glass-coated microwires have been described. Particular attention has been paid to parameters determining the casting and cooling rates that are responsible for the microstructure of as-cast microwires (amorphous or microcrystalline). The following conclusions should be outlined.

The method of continuous casting of glass-coated microwires (Ulitovski–Taylor method) has some limitations determined by the properties of the metal and the glass. The diameters of glass-coated microwires obtained by this technique are limited. In addition, there are limitations on quenching rate and metallic alloy composition.

The range of working temperatures for casting is specific for a given composition of the metallic alloy and the glass for each metallic alloy–glass pair; it depends on the viscosity of the glass and the metal and other physical properties.

The range of existence of metastable phases (amorphous, nanocrystalline, or microcrystalline) is limited to the quenching rate of the metallic core. That maximum quenching rate depends on metallic core diameter, glass coating thickness, chemical composition, and drawing rate.

The main specific feature of cast glass-coated microwires is the occurrence of residual stresses arising from the difference of thermal expansion coefficients of the metallic alloy and the glass coating. This feature is the main factor determining the physical properties of glass-coated microwires, particularly magnetic properties.

Acknowledgments. The author is grateful to A. Yelon, D. Menard, G. V. Lomaev, A. I. Dikusar, and M. Vazquez for discussion and important comments.

References

[1] G. F. Taylor, Phys. Rev., 23**,** 655, (1924).

[2] G. F. Taylor, Process and apparatus for making Filaments, Patented Feb. 24, 1931, United States Patent Office, 1, 793, 529.

[3] A. V. Ulitovski , USSR Patent no. 128427, Bull. Izobret. 3, 9, (1950).

[4] A. V. Ulitovski and N. M. Avernin, USSR Patent no. 161325, Bull. Izobret. 7, 14, (1964).

[5] A. V. Ulitovsky, I. M. Maianski, and A. I. Avramenco, USSR Patent no. 128427, Bull. Izobret. 10, 14, (1960).

[6] S. A. Baranov, V. N. Berezhanskii, V. L. Kokoz, S. K. Zotov, V. S. Larin, and A. V. Torkunov, Fiz. Met. Metalloved., 67 (1), 73, (1989).

[7] S. A. Baranov, Surf. Eng. Appl. Electrochem., 47 (4), 316, (2011).

[8] S. A. Baranov, D. Laroze, P. Vargas, and M. Vazquez, Physica, B., 372, 324, (2006).

[9] S. A. Baranov. Mold. J. Phys. Sci. 13 (3–4), 229, (2014).

[10] E. Ia. Badinter, N. R. Berman, I. F. Drabenco, V. I. Zaborovski, Z. I. Zelikovski, and V. G. Cheban, Litoi mikroprovod i ego svoistva (Cast Microwire and its Properties). Shtinitsa, Kishinev, 1973, 199 p.

[11] V. S. Larin, A. V. Torkunov, A. Zhukov, J. González, M. Vázquez, L. Panina, J. Magn. Magn. Mater. 249, 39, (2002).

[12] S. A. Baranov, Met. Sci. Heat Treat. 43 (3–4), 167, (2001).

[13] S. A. Baranov, Met. Sci. Heat Treat. 45 (7–8), 280, (2003).

[14] S. A. Baranov. Mold. J. Phys. Sci. 14 (3–4), 201, (2015).

ENVIRONMENTAL IMPACT STUDIES RELATED TO ICE-FORMING AEROSOL USAGE IN CLOUD SEEDING ACTIVITIES IN MOLDOVA

E. I. Potapov, A. S. Sidorenko, and E. A. Zasavitsky

Gitsu Institute of Electronic Engineering and Nanotechnologies, Academy of Sciences of Moldova, Academiei str. 3/3, Chisinau, MD-2028 Republic of Moldova
E-mail: efim@nano.asm.md

(Received September 7, 2016)

Abstract

The results of studies of the lead and silver content in water bodies and air and the ice nuclei concentrations in the regions subjected to hail protection in the Republic of Moldova in 1977–1991 are summarized. Until 1983, hail-hazardous clouds were seeded mostly with crystallizing pyrotechnic compositions based on lead iodide; subsequently, silver iodide was used. The problems of environmental pollution in the regions involved in the activities using various crystallizing reagents based on heavy metals are discussed. Accumulation of these metals depending on the type and lifetime of the reagents used is estimated.

1. Introduction

Weather manipulation to mitigate the adverse effects of climate change and the damage caused by natural disasters, such as drought, devastating downpours, and hail, is one of the most important problems of modern science and practical life. In this context, it is particularly important to develop and improve the methods and techniques of active impacts (AIs) aimed at artificial precipitation control, hail prevention, and dissipation of fogs and clouds.

A significant effect on the climate—both globally and regionally—is exerted by aerosols. Aerosols have an impact on both the development of ecosystems and human health.

Aerosol particles in the atmosphere affect the climate directly (absorbing and scattering radiation) and indirectly (impacting and changing the cloud properties). The latter effect, which is referred to as "indirect aerosol effect," occurs because aerosols act as cloud condensation nuclei (CCN) and ice nuclei and thus influence the cloud albedo, lifetime, and other cloud properties. The indirect aerosol effect represents the most uncertain components in future climate scenarios. A challenge in quantifying the aerosol indirect effect is the assessment of both the spatial and temporal variation of CCN. The answer to the question whether an aerosol acts as a CCN to form cloud droplets is determined by both the size and chemical composition of the aerosol [1]. In this case, only an insignificant portion of particles—on the order of particle per million—is the active ice nucleation sites [2].

A particular case of aerosols is artificial ice-forming aerosols used for AIs on atmospheric processes. These impacts are conducted for the protection of agricultural crops and industrial facilities from hail and for the simulation of artificial precipitation. In this case, an important issue is the study of their effect on the environment.

In Moldova, the formation and development of activities on AIs on clouds dates back to the 1960s–1970s. The use of ice-forming compositions (reagents) based on lead iodide (PbI_2) or silver iodide (AgI) for this purpose has necessitated the study of potential accumulation of components of these substances (Pb, Ag) in natural objects, particularly taking into account the fact that, in common with all heavy metals, excessive amounts of lead and silver in the body are toxic. This is particularly true for regions subjected to a long-term and intensive application of these reagents. In the world, the potential environmental impacts of cloud seeding using silver iodide have been studied since the 1960s [3].

Based on the data of studies in different regions of the USSR, it has been found that, during the dissipation of clouds, the reagent is largely entrained with precipitation onto the earth's surface; the rest of its mass penetrates the free atmosphere and then can be transported by air flows to a distance of up to 150 km. It has been shown that, during hail-protection activities, high concentrations of lead and silver are observed in the air in the AI regions; these concentrations depend on the amount of artificial ice-forming compositions introduced into the atmosphere. In seeding convective clouds, the residence time of AgI in the cloud medium is about 20 min [4–13].

To study the effect of systematic AIs using ice-forming reagents on the accumulation of Pb and Ag metals in natural objects, research in the regions subjected to antihail protection in the Moldavian SSR was conducted from 1977 to 1991. The objects of observation were surface and landlocked water bodies---mostly artificial---and ground air. Since 1967, in Moldova, AIs on hail processes have been conducted using ice-forming compositions made of pyrotechnic mixtures containing 60% of lead iodide. Since 1979, formulations containing 2% AgI have been introduced into practice. At present, silver iodide is the most common cloud-seeding material in weather modification projects.

A systematic monitoring of lead and silver content in water bodies and air covers the period from 1977 to 1991 and from 1983 to 1991, respectively. By 1983, the total number of water bodies under observation was 103; 64 of them were located in the protected areas (PAs); the rest, in the control areas (CAs).

Aerosol measurements were conducted at the center of the PA. To determine the Pb and Ag concentrations in the air, every day, from 9 a.m. to 9 p.m., aerosol samples were taken at a height of 12 m above the ground according to a special procedure. The samples were collected on AFA-KhA-20 analytical filters. The filters and water samples were analyzed by atomic absorption spectrophotometry. The sensitivity of the method was 10^{-8}–10^{-9} g, the error was ±15% [14]. The experimental design and routine, the accuracy of measurements of analyzed samples, and the confidence level of the results were confirmed by international expert estimates on the basis of comparative measurements with the participation of specialized research institutes of Russia, Ukraine, and the Republic of Moldova in the 1990s.

Average consumption of PbI_2 and AgI (g/ha) in hail-protection seasons in Moldova in 1978–1991

Agent	Year														
	1978	1979	1980	1981	1982	1983	1984	1985	1986	1987	1988	1989	1990	1991	Average
PbI	11.5	17.1	13.3	10.2	8.5	10.5	7.2	7.2	–	–	–	–	–	–	10.7
AgI	–	–	–	–	–	0.35	0.24	0.24	0.43	0.28	0.28	0.22	0.12	0.16	0.26

In a hail-protection season, depending on its intensity and duration, the consumption of PbI_2 and AgI in ice-forming pyrotechnic compositions was 7.2–17.6 and 0.12–0.43 g/ha of protected area, respectively (table). These data suggest that, every year, significant amounts of lead penetrated the atmosphere in limited areas subjected to AIs.

Figure 1 shows the scheme of location of water bodies in the PAs and CAs and the location of the aerosol measurement site. The CAs were selected so as to minimize the risk of impact on them from AIs in PAs. A necessary requirement for the selection of CAs was their proximity to PAs with respect to physicogeographical and geological features. These conditions were most completely met by water bodies in the CAs in Ukraine and the south of Moldova.

Fig. 1. Scheme of location of the aerosol measurement site and water bodies in the PAs and CAs in the Republic of Moldova in the period of 1983–1991.

A systematic sampling of water from water bodies was conducted twice a year—before (April) and after (October) hail protection season—from 1983 to 1991, except for 1990. The maximum permissible concentration (MPC) of silver was 50 μg/L in drinking water, 0.5 $\mu g/m^3$ in air, and 2.82 mg/kg in soil. The MPC of Pb is 30 μg/L in water and 3 $\mu g/m^3$ in air. It should be noted that lead is one of the most toxic metals; some international organizations and similar government agencies in different countries have included it into the list of priority pollutants. This fact was one of the reasons for switching to pyrotechnic compositions containing silver iodide for using in AIs on atmospheric processes.

2. Results of measurements of lead and silver concentrations in water bodies

Under conditions of Moldova with the priority development of the agricultural sector, there were no metallurgical, merchant-coke, and oil-refining complexes, which are sources of atmospheric pollution with metals. The used organic and mineral fertilizers and pesticides contained extremely small amounts of lead and silver. Therefore, these factors were not taken into account.

A powerful source of lead emission in the atmosphere was automotive transport. The concentrations of lead [Pb] in soil in regions with heavy traffic were ten times higher than their baseline values [15]. Therefore, water bodies located at a distance of no less than 200–300 m from automobile roads with heavy traffic were selected for observations.

In rivers and lakes of Europe, the [Pb] content was 0.4–7.3 μg/L [16]. There are some evidences of a tendency of metal accumulation in natural environment objects [17]. In the late 1970s and the early 1980s, in the central part of Moldova, the lead content in surface waters did not exceed 10 μg/L [15]. This value coincides with the results obtained by us for this region in the period of activities [16].

Figure 2 shows the average [Pb] values in the autumn samples of water from water bodies in the PAs and CAs in Moldova and the CAs in Ukraine. The highest [Pb] values for the entire period of studies were recorded in the PA at the center of Moldova. In 1977, there, the average [Pb] value was 9.5 μg/L against a value of 4.5 μg/L in the water bodies of the CAs. In 1983, the average Pb concentration in the PAs was 22.9 μg/L against 10.7 μg/L in the CAs (Ukraine). In 1988, [Pb] was 26 μg/L in the PAs and 13 μg/L in the CAs (Ukraine). The [Pb] increment was 2.213 μg/L per year in the PAs and 1.0 μg/L in the CAs.

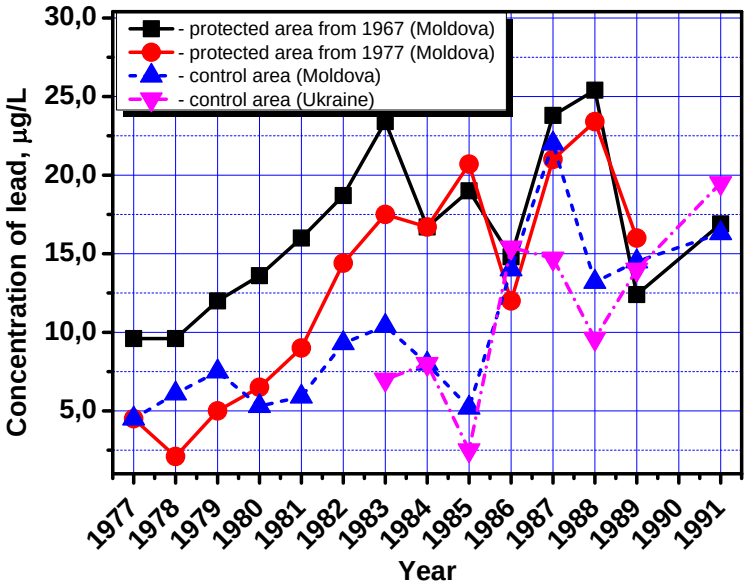

Fig. 2. Average lead concentration in autumn water samples from the water bodies in the PAs and CAs in the period of 1977–1991.

High lead concentrations in the water bodies in the PAs compared to the values in the CAs were observed almost in the entire period of observations. An exception was provided by the last two years, when the metal concentrations were almost equal in all the studied water bodies. It should be noted that, since 1986, only AgI-based reagents were used in AIs.

To estimate the impact of AIs as a source of the studied metals (Me), the metal concentrations in water bodies in the autumn and spring water samples were compared: $\Delta[Me] = [Me]_{autumn} - [Me]_{spring}$.

Figure 3 shows the Δ[Pb] values according to the results of measurements in water bodies in the PAs in Moldova and the CAs in Ukraine. By 1986, for water bodies in the PAs and CAs, the Δ[Pb] values began to decrease. A short series of Δ[Pb] values for water bodies in the PAs with the intensive use of PbI_2 (1981–1982) cannot be a basis for making an unambiguous conclusion about the role of AIs as a lead source affecting the increment of this metal in summer. However, in these two years, in the PAs, Δ[Pb] ≈ 2 μg/L; this value coincides with the concentration increment in the AI seasons. Noteworthy is the fact that, in the summer periods of 1986 and 1987, [Pb] abruptly increased in water bodies both in the PAs and in Ukraine and that, in subsequent years, the self-purification processes were dominant in the compared territories, i.e., Δ[Pb] < 0.

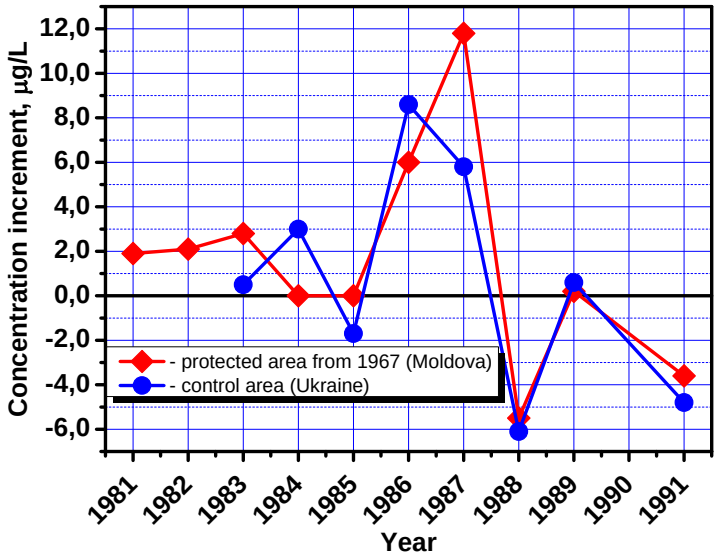

Fig. 3. Δ[Pb] values for water samples from the water bodies in the PAs (the central regions of Moldova) and CAs (Ukraine).

According to various estimates (the 1980s), in the world, anthropogenic sources of silver, particularly weather modification, amounted to about 1200 tons per year, while the natural sources yielded 150 tons per year [19]. These data suggest that the silver concentration ([Ag]) in natural media should be negligible. A low global background level of Ag in water is evidenced, for example, by analysis of water from the lakes in the Tien Shan Mountains, which gives a value of 0.6 μg/L [14].

Figure 4 shows the time variation of the silver content in the water bodies in the PAs and CAs (Ukraine). Throughout the entire period of observations, after AI seasons, the [Ag] value was in a range of 1.7–7.4 μg/L in the water bodies in the PAs and 0.9–4.1 μg/L in the water bodies of the CAs.

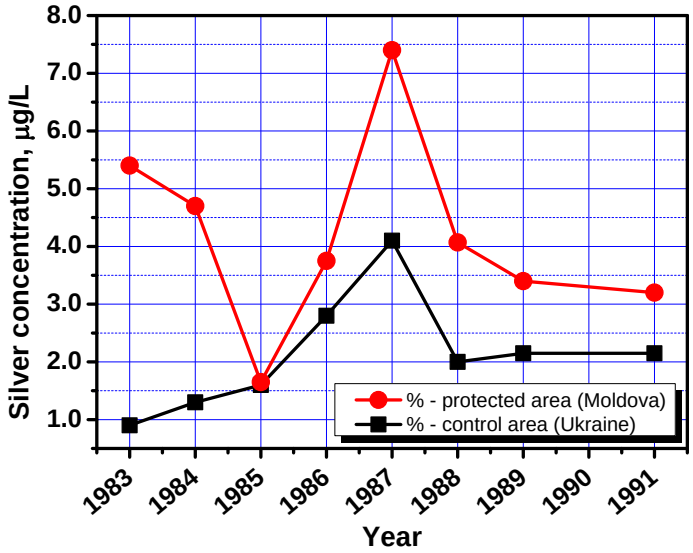

Fig. 4. Silver concentration in the autumn water samples from the water bodies in the PAs in Moldova and the CAs in Ukraine.

Correlation analysis has revealed no relationship between the silver content and the amount of AgI reagents consumed during hail suppression activities. However, the variation of the Δ[Ag] values in the PAs (Fig. 5) shows that the highest values are registered in years with the maximum consumption of AgI during AIs (1983, 1986). Since 1988, Δ[Ag] < 0 for all water bodies in the PAs and CAs.

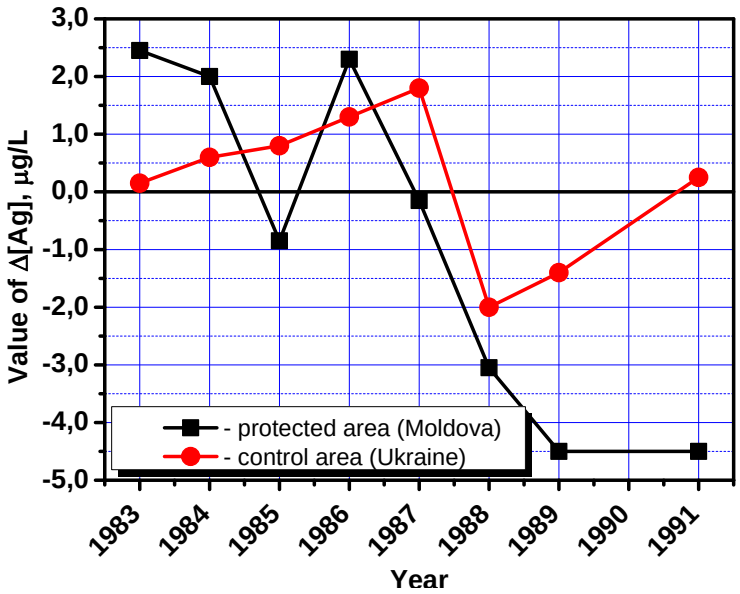

Fig. 5. Silver concentration increment in the water bodies in the PAs and CAs in the summer periods of 1983–1991.

The highest Δ[Ag] values are registered for the central regions of Moldova; in some years, these values are 3–4 µg/L higher than Δ[Ag] in the water bodies in the PAs with a lower level of hail

precipitation. It should be emphasized that Δ[Ag] in the PAs in the south regions of Moldova is almost the same as the Δ[Ag] value for the water bodies located in the territory of Ukraine.

The studies have shown that differences in [Ag] values in water bodies of different PAs can be attributed to their natural variability. This assumption is confirmed both by the absence of a correlation between the silver content and the amount of AgI-containing compositions introduced into clouds annually and by the fact that [Ag] in water bodies in PAs is inversely related to the total amount of precipitation (Q*mm*) occurring there in summer periods. For the central regions of Moldova, which is a territory with the longest use of AgI, correlation coefficient r(Q,[Ag]) = –0.69. For other regions of the PAs, this relationship is even weaker; however, all of them are characterized by an inverse correlation. This result suggests that the silver content in the studied water bodies in the PAs is determined by factors that are not directly related to hail suppression activities.

In discussing the nature of the time series of [Ag], it is essential to determine the trends. In this case, the trend is understood as a tendency of variation in the metal concentration in the studied water bodies for the entire period of observations. Taking into account the specific features of the studied experimental units (research subjects) and the nature of the possible effect on them exerted by a silver source (AIs), it is possible to use the following linear equation:

$$y_t = \alpha_0 + \alpha_1 t \text{ ,}$$

where y_t is the value of the studied quantity; α_0, α_1 are coefficients (α_1-trend), and t is the number of years (seasons) of measurements (t = 1, ..., n).

For all the studied territories, $\alpha_1 > 0$; that is, a positive tendency of increase in [Ag] in the water bodies was observed regardless of their location. The average value was α_1 = 0.52 and 0.35 μg/L per year for the PAs and CAs, respectively. However, the confidence levels (statistical reliability) of these trends are not high. Therefore, the hypothesis that stable increments in the silver content in water bodies in Moldova are attributed to hail-suppression activities with the use of AgI could not be confirmed with a high degree of probability.

3. Results of measurement of the lead and silver content in the ground air in PAs

In the 1960s, the average lead concentration in the air was 0.03 μg/m^3 in the industrial cities of the USSR and 0.02 μg/m^3 for rural areas. In the 1970s, in the United States, these concentrations were 1.6 and 0.3 μg/m^3, respectively [20]. In the European countries, the metal content in the air was in a range of 0.03–0.05 μg/m^3 [21].

According to [22], in autumn and summer, in the cities of the USSR, the average silver concentration in the air was 0.03–0.06 μg/m^3. From 1974 to 1979, in regions of hail-suppression activities in the Krasnodar Territory and North Caucasus, the average multiyear value was [Ag] = 0.087 and 0.045 ng/m^3, respectively [13].

Figure 6 shows the average concentration of Ag and Pb in the air in hail-protection seasons. The high lead content was registered in the periods of AIs using mostly PbI_2-based compositions, i.e., until 1983. In subsequent years, the seasonal values of [Pb] did not exceed 0.17 μg/m^3. In this period, the decrease was about tenfold compared with the level in 1977–1980.

In hail-protection seasons, the Ag concentrations were in a range of 0.001–0.043 μg/m^3; this level characterized the studied region as environmentally friendly. In the annual variation of [Ag], the highest values were registered in the period of June–August, the lowest concentrations occurred in autumn and winter (Fig. 7).

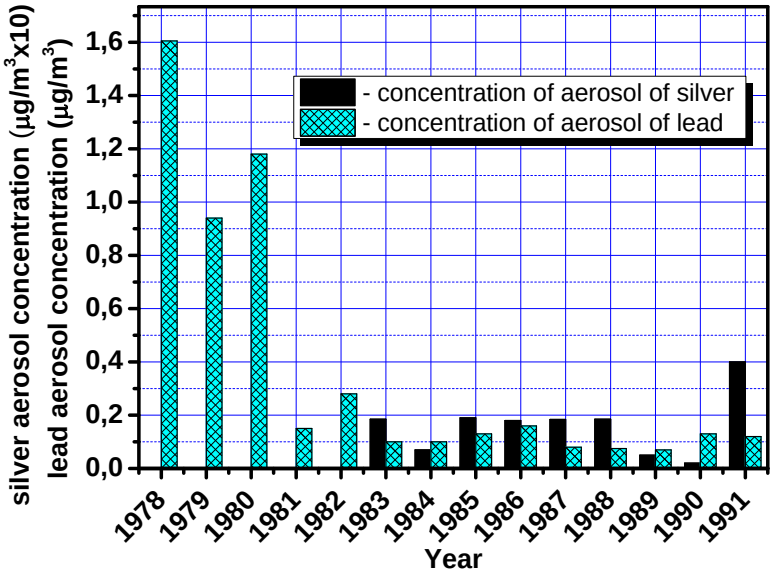

Fig. 6. Average concentration of silver ($\mu g/m^3 \times 10$) and lead ($\mu g/m^3$) in the ground air in hail-protection periods in the Republic of Moldova in 1978–1991.

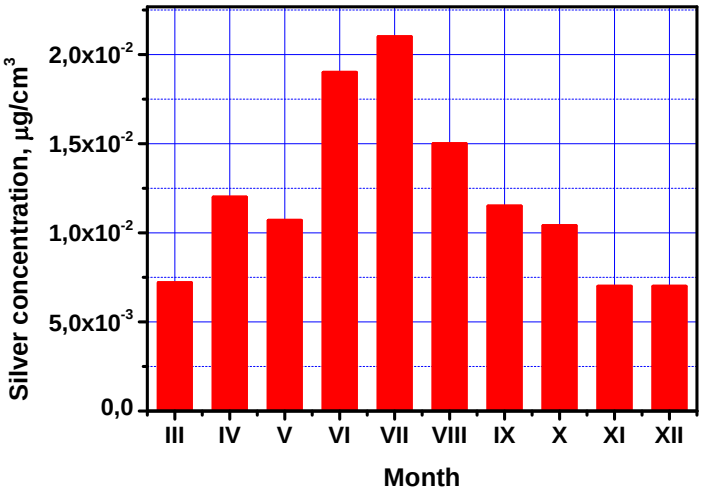

Fig. 7. Annual variation of [Ag] in the ground air (1983–1991).

The absence of silver accumulation in the air is also evidenced by the values of Ag concentration trends: $\alpha_1 < 0$ for both the annual average and the summer seasons (AI seasons) at $\sigma = 0.037$ and 0.007 $\mu g/m^3$, respectively.

4. Conclusions

Our studies of the effect of long-term cloud seeding with crystallizing reagents based on lead iodide and silver iodide on the environmental conditions in the regions involved in hail-suppression activities in the Republic of Moldova have revealed the following.

(1) There is a tendency of lead accumulation in surface waters from one hail-protection season to another with a value of about 2 μg per liter of water in the periods of use of lead iodide as a reagent.

(2) In some PAs, the lead content in water was close to maximum permissible values (MPC = 50 μg/L).

(3) There is a positive correlation between an increase in the lead concentration in water bodies and the amount of precipitation in the AI seasons in the studied territory.

(4) In the hail-protection seasons in 1978–1981, in some months, the average lead aerosol content in the ground air exceeded 1.0 $\mu g/m^3$.

(5) The monthly average lead aerosol concentrations in the ground air positively correlated with the amount of the reagent consumed in these periods.

(6) Upon switching to the use of ice-forming compositions based on 2% AgI for AIs, the water bodies and the ground air underwent self-purification of lead.

(7) In the cases of using ice-forming compositions with 2% AgI in hail-suppression activities, no statistically significant events of silver accumulation in water samples from water bodies in the PAs were registered.

(8) In the period of studies, the average silver concentration in water bodies in the PAs did not exceed 6.2 μg/L.

(9) Long-term observations of the use of AgI-based ice-forming compositions have not revealed either a tendency of silver aerosol accumulation in the ground air or its correlation with the amount of the consumed reagent.

(10) The results clearly show that there are no environmentally harmful effects arising from cloud seeding programs involving silver iodide aerosols in Moldova.

References

[1] B. Friedman, A. Zelenyuk, J. Beranek, et al., Atmos. Chem. Phys. 13, 11839, (2013).
[2] P. J. Demott, A. J. Prenni, X. Liu, et al., Proceedings of the National Academy of Sciences of the United States of America 107, 11217, (2010).
[3] A. K. Donald, Environmental Impacts of Artificial Ice Nucleating Agents, Dowden, Hutchinson & Ross, Inc., Stroudsburg, 1978.
[4] L. V. Burtseva, Trudy VGI, Gidrometeoizdat, Leningrad. 32, 74, (1975).
[5] I. I. Burtsev, L. V. Burtseva, T. I. Vorob'eva, et al., Trudy VGI, Gidrometeoizdat, Leningrad, 22, 201, (1973).
[6] I. I. Burtsev, L. V. Burtseva, T. I. Vorob'eva, and S. V. Shvedov, Trudy VGI, Gidrometeoizdat, Leningrad. 25, 98, (1974).
[7] I. I. Burtsev, T. I. Vorob'eva, M. M. Chernyak, S. V. Shvedov, Trudy VGI, Gidrometeoizdat, Moscow, 51, 140, (1982).
[8] T. N. Gromova, I. A. Skorodenok, N. V. Toropova, and T. M. Ungerman, Trudy Glavnoi Geofizicheskoi Observatorii, Gidrometeoizdat, Leningrad. 439, 84, (1981).

[9] A. V. Nikorici, T. D. Nikorici, E. I. Potapov, and S. S. Shalavejus, in Sb. Fizika Atmosfery, Mokslas, Vilnyus, 1989.
[10] E. V. Preobrazhenskaya, Trudy Glavnoi geofizicheskoi observatorii, Gidrometeoizdat, Leningrad, 239, 43, (1969).
[11] G. Supatashvili, A. Kartsivadze, L. Abesalashvili, N. Karsanidze, G. Asambidze Khimiya, biologiya (Tbilisi Univ.). 178, 15, (1976).
[12] T. I. Vorob"eva Trudy VGI, Gidrometeoizdat Moscow. 51, 127, (1982).
[13] T. I. Vorob"eva, L. P. Gushchina, E. N. Maslovskaya, et al. Trudy VGI, Gidrometeoizdat, Moscow. 74, 145, (1989).
[14] A. V. Arkharov, V. V. Ishchenko, E. I. Zotov, E. I. Potapov, Trudy CAO, Gidrometeoizdat, Moscow, 177, 123, (1992).
[15] N. F. Myrlyan, Geokhimiya agrolandshaftov Moldavii, Kishinev: Shtiinta, 1989.
[16] F. Ya. Rovinskii, V. I. Egorov, M. I. Afanas'ev, and L.V. Burceva. Problemy Fonovogo Monitoringa Sostoyaniya Prirodnoi Sredy. 7, 3, (1989).
[17] A. M. Nikanorov and Zhulidov A.V., Biomonitoring tyazhelykh metallov v presnovodnykh ekosistemakh, Gidrometeoizdat, St. Petersburg, 1991.
[18] E. S. Zharinova and E. I. Potapov, Trudy CAO, Gidrometeoizdat, Moscow, 142, 105, (1980).
[19] A. G. Amelin Teoreticheskie osnovy obrazovaniya tumana pri kondensatsii para, Khimiya, Moscow, 1972.
[20] T. M. Zhigalovskaya Meteorologicheskie Aspekty Zagryazneniya Atmosfery, Gidrometeoizdat, Moscow, 1971.
[21] Ya. Shatrokh and D. Zavodski, Problemy fonovogo monitoringa sostoyaniya prirodnoi sredy, Gidrometeoizdat, Leningrad. 7, 14, (1989).
[22] L. S. Ivlev, Khimicheskii sostav i struktura atmosfernykh aerozolei, LGU, Leningrad, 1982.

RADIATION EFFECTS ON AN UNSTEADY SQUEEZING FLOW IN THE PRESENCE OF A MAGNETIC FIELD

Kalidas Das[1] and Umaru Mohammed[2]

[1]Dept. of Mathematics, A.B.N. Seal College, Coochbehar, W.B., Pin-736101, India
E-mail: kd_kgec@rediffmail.com
[2]Department of Mathematics/ Statistics, Federal University of Technology, P.M.B 65, Minna, Nigeria
E-mail: digitalumar@yahoo.com

(Received March 22, 2016)

Abstract

This work is focused on the examination of the effect of thermal radiation on the heat and mass transfer characteristics of an incompressible electrically conducting fluid squeezed between two parallel plates in the presence of a transverse magnetic field. Using the similarity transformation, the governing system of nonlinear partial differential equations is transformed into similarity equations which are solved numerically using the Nachtsheim and Swigert shooting iteration technique together with the Runge–Kutta sixth-order integration scheme. Numerical results are presented through graphs and tables for pertinent parameters to show interesting aspects of the solution.

1. Introduction

The squeezing flow of Newtonian and non-Newtonian fluids has received considerable attention from researchers because of numerous applications in different engineering disciplines, such as polymer processing, transient loading of mechanical components, compression, injection molding, and squeezed films in power transmission. These flows are induced by two approaching parallel surfaces in relative motion. The application of a magnetic field in these flows makes it possible to prevent the unpredictable deviation of lubrication viscosity with temperature under certain extreme operating conditions. Stefan [1] was the first to initiate pioneering works on the squeezing flow by invoking a lubrication approach. Two-dimensional and axisymmetric squeezing flows between parallel plates have been addressed by Rashidi et al. [2]. Siddiqui et al. [3] discussed the effects of a magnetic field in the squeezing flow between infinite parallel plates due to the normal motion of plates. Domairry and Aziz [4] provided an approximate analytic solution for the squeezing flow of a viscous fluid between parallel disks with suction or blowing. Hayat et al. [5] extended the work presented in [4] to analyze the squeezing flow of non-Newtonian fluids taking second grade fluids. The homotopy perturbation method (HPM) has been applied in [3, 5] for the presentation of analytic solutions of the arising nonlinear problems.

In recent years, the study of heat and mass transfer of viscous fluids in a squeezing flow has increased due to their applications in many branches of science and engineering. A few representative fields of interest in which a combined heat and mass transfer effect plays an

important role are the design of chemical processing equipment, the formation and dispersion of fog, and the distribution of temperature and moisture over agricultural fields and groves of fruit trees. Heat transfer characteristics in a squeezing flow between parallel disks were studied by Duwairi et al. [6]. Khaled and Vafai [7] analyzed the hydromagnetic effects on flow and heat transfer over a horizontal surface placed in an externally squeezed free stream. Squeezing flows and heat transfer over a porous plate were investigated by Mahmood et al. [8]. Mustafa et al. [9] considered the combined effects of heat and mass transfer in a viscous fluid squeezed between two parallel plates. Chamkha [10] investigated the problem of heat and mass transfer by a steady flow of an electrically conducting fluid past a moving vertical surface in the presence of a first order chemical reaction. Kandasamy et al. [11] studied the nonlinear MHD flow with heat and mass transfer of an incompressible viscous electrically conducting fluid on a vertically stretching surface with chemical reaction and thermal stratification effects. Patil and Kulkarni [12] considered the effects of chemical reaction on the free convection flow of a polar fluid through a porous medium in the presence of internal heat generation.

However, the effect of thermal radiation on the flow and heat transfer has not been taken into account in most of the investigations. The radiation effect on an MHD flow and the heat transfer problem have become more important for industry. Cogley et al. [13] showed that, in an optically thin limit, the fluid does not absorb its own emitted radiation but the fluid does absorb radiation emitted by the boundaries. Raptis [14] investigated the steady flow of a viscous fluid through a porous medium bounded by a porous plate subject to a constant suction velocity in the presence of thermal radiation. Makinde [15] examined the transient free convection interaction with thermal radiation of an absorbing emitting fluid along a moving vertical permeable plate. Ibrahim et al. [16] discussed the case of a mixed convection flow of a micropolar fluid past a semi-infinite steady moving porous plate at varying suction velocity normal to the plate in the presence of thermal radiation and viscous dissipation. Das [17] analyzed the problem analytically to consider the effect of a first order chemical reaction and thermal radiation on a micropolar fluid in a rotating frame of reference. Recently, Das [18] has investigated the impact of thermal radiation on an MHD slip flow over a flat plate with variable fluid properties. The present study focuses on an unsteady MHD squeezing flow and heat transfer between two parallel plates in the presence of a transverse magnetic field and thermal radiation.

2. Mathematical formulation of the problem

Consider an unsteady two-dimensional squeezing flow of an incompressible viscous electrically conducting fluid between infinite parallel plates. The coordinate system is chosen such that the x-axis is along the plate and the y-axis is normal to the plate. The two plates are placed at $y = \pm h(t)$, where $h(t) = H(1 - \alpha t)^{1/2}$ and α is a characteristic parameter having dimensions of time inverse. The two plates are squeezed at a velocity of $v(t) = dh/dt$ until they touch. A uniform magnetic field of strength $B(t) = B_0(1 - \alpha t)^{-1/2}$ [19] is applied perpendicular to the plate, and the electric field is taken as zero. In addition, it is assumed that there exists a homogeneous first-order chemical reaction with time dependent reaction rate of $K_1(t) = k_1(1 - \alpha t)^{-1}$ between the diffusing species and the fluid. Here, the symmetric nature of the flow is adopted.

Under the stated assumptions, the governing conservation equations of mass, momentum, energy and mass transfer at an unsteady state can be expressed as follows:

$$\frac{\partial u}{\partial x}+\frac{\partial v}{\partial y}=0 \tag{1}$$

$$\frac{\partial u}{\partial t}+u\frac{\partial u}{\partial x}+v\frac{\partial u}{\partial y}=-\frac{1}{\rho}\frac{\partial p}{\partial x}+\nu\left(\frac{\partial^2 u}{\partial x^2}+\frac{\partial^2 u}{\partial y^2}\right)-\frac{\sigma B^2(t)}{\rho}u \tag{2}$$

$$\frac{\partial u}{\partial t}+u\frac{\partial v}{\partial x}+v\frac{\partial v}{\partial y}=-\frac{1}{\rho}\frac{\partial p}{\partial y}+\nu\left(\frac{\partial^2 v}{\partial x^2}+\frac{\partial^2 v}{\partial y^2}\right) \tag{3}$$

$$\frac{\partial T}{\partial t}+u\frac{\partial T}{\partial x}+v\frac{\partial T}{\partial y}=\frac{\kappa}{\rho C_p}\left(\frac{\partial^2 T}{\partial x^2}+\frac{\partial^2 T}{\partial y^2}\right)+\frac{\nu}{C_p}\left[4\left(\frac{\partial u}{\partial x}\right)^2+\left(\frac{\partial u}{\partial y}+\frac{\partial v}{\partial x}\right)^2\right]-\frac{1}{\rho C_p}\frac{\partial q_r}{\partial y} \tag{4}$$

$$\frac{\partial C}{\partial t}+u\frac{\partial C}{\partial x}+v\frac{\partial C}{\partial y}=D\left(\frac{\partial^2 C}{\partial x^2}+\frac{\partial^2 C}{\partial y^2}\right)-K_1(t)C \tag{5}$$

where u and v are velocity components along the x- and y-axis, respectively, ρ is the density of the fluid, υ is the kinematic viscosity, C_p is the specific heat at constant pressure p, κ is the thermal conductivity of the medium, T is the temperature of the fluid, C is the concentration of the solute, and D is the molecular diffusivity.

Following the Rosseland approximation with the radiative heat flux, q_r is modelled as follows:

$$q_r=-\frac{4\sigma^*}{3k^*}\frac{\partial T^4}{\partial y} \tag{6}$$

where σ^* is the Stefan–Boltzmann constant and k^* is the mean absorption coefficient. Assuming that the differences in temperature within the flow are such that T^4 can be expressed as a linear combination of temperature, we expand T^4 in Taylor's series about T_∞ and neglecting higher order terms, we obtain

$$T^4=4T_\infty{}^3T-3T_\infty{}^4 \tag{7}$$

Thus, we have

$$\frac{\partial q_r}{\partial y}=-\frac{16T_\infty{}^3\sigma^*}{3k^*}\frac{\partial^2 T}{\partial y^2} \tag{8}$$

Therefore, Eq. (4) reduces to

$$\frac{\partial T}{\partial t}+u\frac{\partial T}{\partial x}+v\frac{\partial T}{\partial y}=\frac{\kappa}{\rho C_p}\left[\frac{\partial^2 T}{\partial x^2}+\left(1+\frac{16T_\infty{}^3\sigma^*}{3k^*\kappa}\right)\frac{\partial^2 T}{\partial y^2}\right]+\frac{\nu}{C_p}\left[4\left(\frac{\partial u}{\partial x}\right)^2+\left(\frac{\partial u}{\partial y}+\frac{\partial v}{\partial x}\right)^2\right]. \tag{9}$$

The appropriate initial and boundary conditions for the problem are

$$\left.\begin{aligned} &u=0, v=v_w=\frac{dh}{dt}, T=T_H, C=C_H \text{ at y=h(t),}\\ &v=\frac{\partial u}{\partial y}=\frac{\partial T}{\partial y}=\frac{\partial C}{\partial y}=0 \text{ at y=0} \end{aligned}\right\}. \tag{10}$$

Using the following dimensionless quantities

$$\left.\begin{aligned} &\eta=\frac{y}{H\sqrt{1-\alpha t}},\ \ \mathrm{u}=\frac{\alpha x}{2(1-\alpha t)}f'(\eta),\ \ \ \mathrm{v}=-\frac{\alpha H}{2\sqrt{1-\alpha t}}f(\eta),\\ &\theta=\frac{T}{T_H},\ \ \phi=\frac{C}{C_H}, \end{aligned}\right\} \tag{11}$$

for Eqs. (2) and (3) and then eliminating the pressure gradient from the resulting equations, we can finally obtain

$$f'''-S\left(\eta f'''+3f''+ff'-f'f'''\right)-M^2f''=0 \tag{12}$$

Now Eqs. (9) and (5) take the following forms:

$$(1+N_r)\theta''2+\mathrm{Pr}\,S\left(f\theta'-\eta\theta'\right)+\mathrm{Pr}\,Ec\left(\mathrm{f}''^2+4\delta^2f'^2\right)=0, \tag{13}$$

$$\phi''+ScS(\mathrm{f}\,\phi'-\eta\phi')-Sc\gamma\phi=0, \tag{14}$$

with the associated boundary conditions

$$\left.\begin{aligned} &f=0,\ f''=0,\ \theta'=0,\ \phi'=0 \text{ for } \eta=0\\ &f=1,\ f'=0,\ \theta=1,\ \phi=1 \text{ for } \eta=1 \end{aligned}\right\}. \tag{15}$$

Here, $S=\frac{\alpha H^2}{2\upsilon}$ is the squeeze number where $S > 0$ corresponds to the plates moving apart, while $S < 0$ corresponds to the plates moving together (the so-called squeezing flow), $M=HB_0\sqrt{\frac{\sigma}{\mu}}$ is the Hartmann parameter, $\mathrm{Nr}=\frac{16T_\infty^3\sigma^*}{3k^*\kappa}$ is the thermal radiation parameter, $\mathrm{Pr}=\frac{\mu\mathrm{C}_p}{\kappa}$ is the Prandtl number, $Ec=\frac{v_w^2}{H^2T_H\,\mathrm{C}_p}$ is the Eckert number, $Sc=\frac{\upsilon}{D}$ is the Schmidt number, $\delta=\frac{H\sqrt{1-\alpha t}}{x}$ is the dimensionless number whose value is fixed throughout the entire study, and $\gamma=\frac{k_1H^2}{\nu}$ is the chemical reaction parameter, where $\gamma>0$ represents a destructive reaction, $\gamma<0$ represents a generative reaction, and $\gamma=0$ represents no reaction.

The parameters of interest for our problem are skin friction coefficient C_{fr}, reduced Nusselt number Nu_{r}, and reduced Sherwood number Sh_{r}. The local dimensionless skin friction coefficient is given by

$$C_{fr} = f''(1) \text{ , where } C_{f_r} = \frac{\sqrt{1-\alpha t}H^2 \mathrm{Re}_x}{x^2} C_f . \tag{16}$$

The rate of heat transfer in terms of the dimensionless Nusselt number is defined as follows:

$$\mathrm{Nu}_r = -\theta'(1) \text{ where } \mathrm{Nu}_r = \sqrt{1-\alpha t}\,Nu \tag{17}$$

Similarly the rate of mass transfer in terms of the dimensionless Sherwood number is given by

$$Sh_r = -\phi'(1) \text{ where } \mathrm{Sh}_r = \sqrt{1-\alpha t}\,Sh \tag{18}$$

3. Method of solution

The set of Eqs. (12), (13), and (14) under boundary conditions (15) was solved numerically by applying the Nachtsheim and Swigert shooting iteration technique [20] together with the Runge–Kutta sixth-order integration scheme. The unspecified initial conditions were assumed and then integrated numerically as an initial value problem to a given terminal point. A step size of $\Delta\eta = 0.001$ was selected to be satisfactory for a convergence criterion of 10^{-6} in nearly all cases. In order to ascertain the accuracy of our numerical results, the present study (in absence of a magnetic field and thermal radiation) was compared with the data of Mustafa et al. [9]. The $-f''(1)$, $-\theta'(1)$ and $-\varphi'(1)$ values were calculated for various *S* values. Excellent agreement was found between the results, as shown in Table 1. Thus, the use of the present numerical code for the current model was justified.

Table 1. Comparison of the values of Skin friction coefficient, Local Nusselt number, and local Sherwood number for various *S* values at $M = Nr = 0$

	Mustafa et al. [9]			Present Results		
S	$-f''(1)$	$-\theta'(1)$	$-\varphi'(1)$	$-f''(1)$	$-\theta'(1)$	$-\varphi'(1)$
-1.0	2.170090	3.319899	0.804558	2.170091	3.319899	0.804558
-0.5	2.614038	3.129491	0.7814023	2.614038	3.129491	0.7814023
0.5	3.336449	3.026324	0.7442243	3.336449	3.026324	0.7442243
2.0	4.167389	3.118551	0.7018132	4.167389	3.118551	0.7018132

4. Numerical results and discussion

To analyze the effects of different parameters of practical importance on the behaviour of the flow, heat and mass transfer characteristics, we plot the velocity, temperature and concentration profiles against η for different values of the pertinent parameters. In the simulation, the default values of the parameters are considered as M = 5.0, Sc = 1.0, S =1.0, Pr = 0.71, γ = 0.5, δ = 0.1, Ec = 1.0, and Nr = 2.0 (Mustafa et al. [9]) unless otherwise specified. For illustrations of the results, numerical values are plotted in Figs. 1–6 and Table 2.

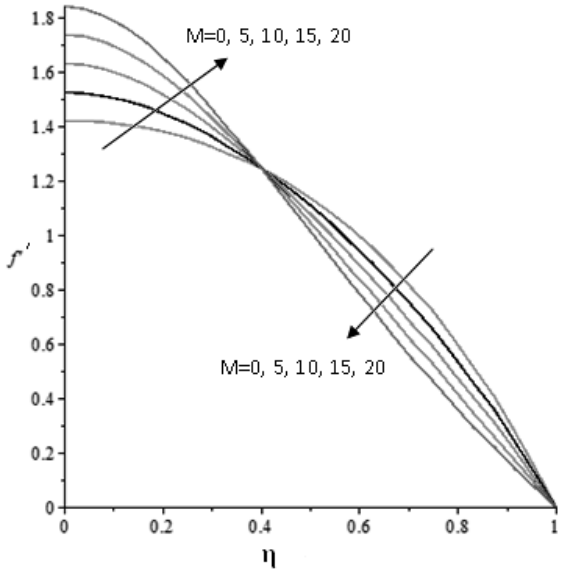

Fig. 1. Velocity profiles for various M values.

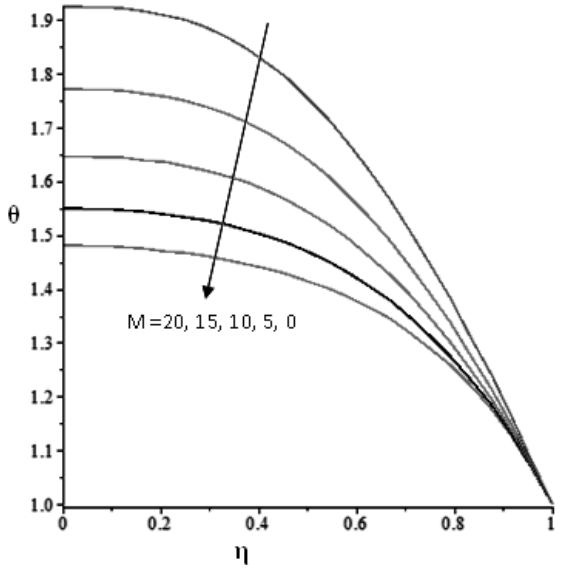

Fig. 2. Temperature profiles for various M. values.

The effect of Hartmann number M on the fluid velocity and temperature distribution is shown in Figs. 1 and 2, respectively. It is evident from Fig. 1 that the fluid velocity increases with increasing M values; therefore, the thickness of the momentum boundary layer for $\eta < 0.4$ (not precisely determined) decreases. However, an opposite trend is observed for $\eta \geq 0.4$ (not precisely determined). The reason behind this phenomenon is that application of a magnetic field to an electrically conducting fluid gives rise to a resistive-type force, which is referred to as the Lorentz force. This force exhibits a tendency to slow down the motion of the fluid in the boundary layer region. Figure 2 clearly indicates that the fluid temperature increases with increasing Hartmann number M in the central region and, as a consequence, the thickness of the thermal boundary layer decreases. This result qualitatively agrees with the expectations because the magnetic field exerts a retarding force on the convection flow and increases its temperature profiles. Table 2 presents the C_{fr}, Nu_{r}, and Sh_{r} values which are proportional to skin friction, rate of heat transfer, and rate of mass transfer from the surface of the plate, respectively, for the various M values. It is evident from the table that both the C_{fr} and Nu_{r} values decrease with increasing M. On the other hand, the effect of M value on Sherwood number Sh_{r} is not significant.

Table 2. Effects of various parameters on skin friction, local Nusselt number, and local Sherwood number

M	Nr	$-f''(1)$	$-\theta'(1)$	$-\varphi'(1)$
0.0	1.0	3.6384	1.7430	0.7287
0.2		3.6166	1.7410	0.7286
0.6		3.5730	1.7372	0.7283
1.0	0.0	3.5296	0.0000	0.7281
	0.5	-	1.1034	-
	1.0	-	1.7339	-

Figure 3 demonstrates the effects of thermal radiation parameter Nr on fluid temperature in the presence of a magnetic field. It is observed from the figure that temperature increases with increasing Nr in the middle region of the parallel plates and is minimal near the surface of the plates. Physically, this can be explained as follows: an increase in the radiation parameter means the release of heat energy from the flow region; therefore, the fluid temperature decreases as the thermal boundary layer becomes thinner. It is evident from Table 2 that with an increase in thermal radiation parameter Nr, the Nusselt number increases.

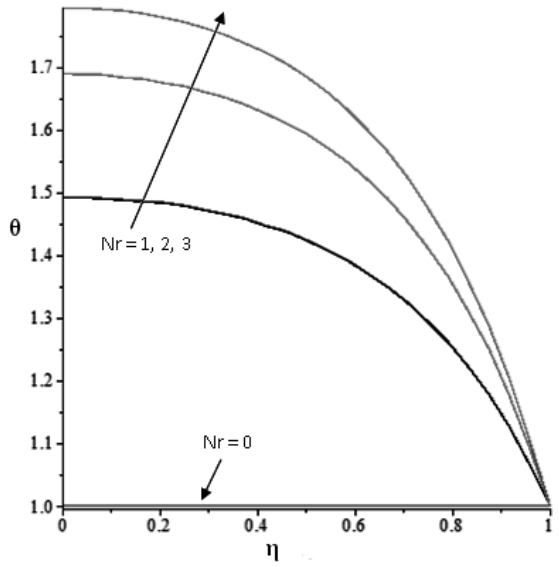

Fig. 3. Temperature profiles for various *Nr* values.

Effects of varying the value of squeeze number *S* on the velocity, temperature, and concentration distribution are illustrated in Figs. 4–6, respectively. With the increase in squeeze number *S*, the fluid velocity decreases first for $\eta < 0.45$ (not precisely determined); then it starts increasing, as shown in Fig. 4. It is evident from Fig. 5 that the fluid temperature decreases as *S* increases. It is worth mentioning that an increase in *S* can be associated with a decrease in the kinematic viscosity, an increase in the distance between the plates, and an increase in the velocities at which the plates move. The concentration distribution increases with increasing *S* values, as depicted in Fig. 6.

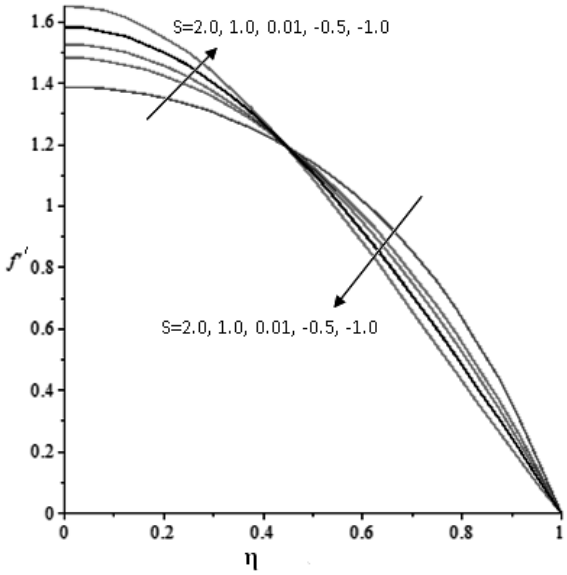

Fig. 4. Velocity profiles for various *S* values.

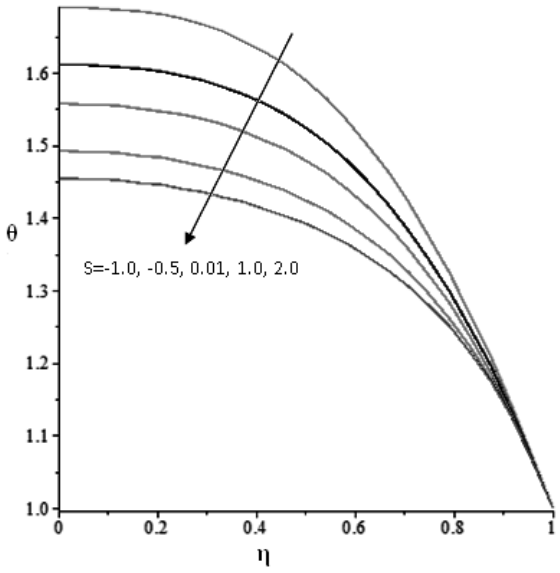

Fig. 5. Temperature profiles for various *S* values.

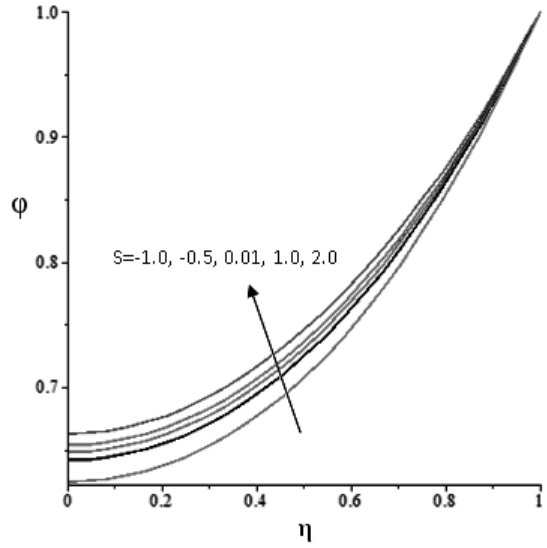

Fig. 6. Concentration profiles for various φ values.

5. Conclusions

In the present paper, the effect of a magnetic field and thermal radiation on the unsteady squeezing flow in a viscous incompressible electrically conducting fluid between two parallel plates has been analyzed using a numerical technique. Numerical results are presented through graphs and tables to illustrate the details of the flow characteristics and their dependence on

material parameters. Based upon the above-described results, the following conclusions can be drawn:

(i) The results indicate a decrease in the skin friction coefficient with an increase in the magnetic field strength. From an industrial point of view, this outcome is desirable since the drag force in the fluid squeezing between the plates decreases with increasing magnetic field strength.

(ii) With an increase in the thermal radiation parameter, the dimensionless heat transfer rate increases.

(iii) For an enhanced squeeze number, both the mass transfer coefficient and the heat transfer coefficient tend to decrease, while the skin friction coefficient tends to increase.

(iv) An increase in the relative strength of the magnetic field leads to a decrease in both the wall shear stress and the rate of heat transfer.

References

[1] M. J. Stefan, Abt. II, Österr. Akad. Wiss. Math.-Naturwiss. Kl. 69, 713, (1874)

[2] M. M. Rashidi, H. Shahmohamadi, and S. Dinarvand, Math. Probl. Eng. 2008, 935095, (2008)

[3] A. M. Siddiqui, S. Irum, and A. R. Ansari, Math. Model. Anal. 13, 565, (2008)

[4] G. Domairry and A. Aziz, Math. Prob. Eng. 2009, 603916, (2009)

[5] T. Hayat, A. Yousaf, M. Mustafa, and S. Obaidat, Int. J. Numer. Methods Fluids 69, 399, (2011)

[6] H. M. Duwairi, B. Tashtoush, and R. A. Domseh, Heat Mass Transfer 14, 112, (2004)

[7] A. R. A. Khaled, and K. Vafai, Int. J. Eng. Sci. 42, 509, (2004)

[8] M. Mahmood, S. Asghar, and M. A. Hossain, Heat Mass Transfer 44, 165, (2007)

[9] M. Mustafa, T. Hayat, and S. Obaidat, Meccanica 47, 1581, (2012)

[10] A. J. Chamkha, Int. Comm. Heat Mass Transfer 30, 413, (2003)

[11] R. Kandasamy, K. Periasamy, and K. K. S. Prabhu, Int. J. Heat Mass Transfer 48, 4557, (2005)

[12] P. M. Patil, and P. S. Kulkarni, Int. J. Therm. Sci. 47, 1043 (2008)

[13] A. C. Cogley, W. E. Vincenty, and S. E. Gilles, AIAA J. 6, 551, (1968)

[14] A. Raptis, Int. Comm. Heat Mass Transfer 25, 289, (1998)

[15] O. D. Makinde, Int. Comm. Heat Mass Transfer 32, 1411, (2005)

[16] F. S. Ibrahim, A. M. Elaiw, and A. A. Bakr, Appl. Math. Inf. Sci. 2, 143, (2008)

[17] K. Das, Int. J. Heat Mass Transfer 54, 3505, (2011)

[18] K. Das, Heat Mass and Transfer 48, 767, (2012)

[19] A. Hussain, S. T. Mohyud-Din, and T. A. Cheema, Chin. Phys. Lett. 29, 114705-1, (2012)

[20] N. G. Kafoussias, and N. G. Williams, Int. J. Eng. Sci. 33, 1369, (1995)

IN MEMORIAM OF ANDREI NICORICI

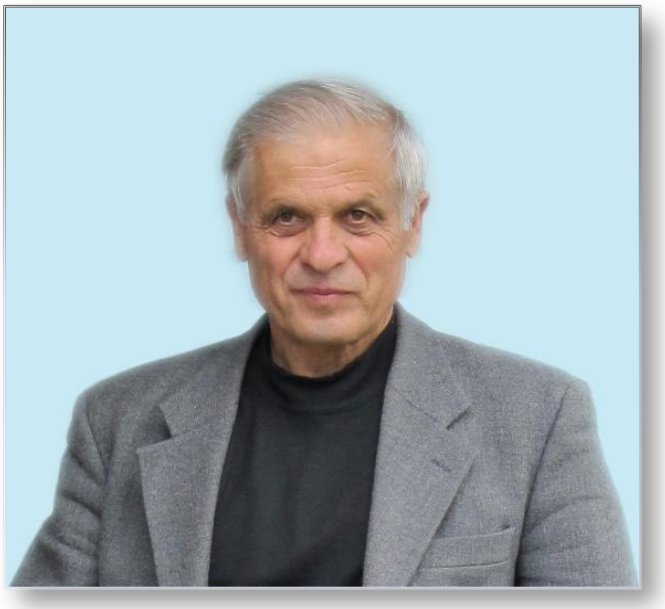

(December 23, 1947 – September 18, 2016)

We are deeply saddened by the passing away of one of the prominent physicists of the Republic of Moldova Dr. Andrei Nicorici on September 18**,** 2016.

Dr. Andrei Nicorici was born in Costiceni village, Noua Sulita district, Chernivtsi region, Ukraine on December 23, 1947. In 1965–1970 he was a student and completed his undergraduate degree at the Physics Department of the Faculty of Physical and Mathematical Sciences, Kishinev State University (at present, State University of Moldova). After graduation from the University, he was invited by Prof. I.C. Andronic to work at the Department of Electrophysics of the University, where he held the following positions: laboratory assistant, senior laboratory assistant, junior researcher, and senior researcher. As a laboratory staff member of the department, Andrei Nicorici improved the existing laboratory works and developed new ones; he designed a number of tools for the orientation, cutting, and machining of semiconductor crystals. He registered several innovation proposals.

In 1985, Andrei Nicorici successfully defended his thesis for the degree of candidate of physical and mathematical sciences (at present, doctor in physics and mathematics).

In 1987 he joined the Laboratory for low-temperature physics at the Institute of Applied Physics, Academy of Sciences of Moldova as a senior researcher; in 1995 he became a leading researcher. He proved to be a highly skilled specialist in the field of physics and technology of semiconductor materials. Andrei Nicorici successfully solved an intricate technological problem associated with the preparation of high-quality lead–tin chalcogenide crystals and films with controlled parameters.

Physicist Andrei Nicorici had the ability to solve extremely complex technological and scientific problems. His research was focused on physics of IV–VI semiconductors and device structures on its basis. He proposed a few fundamentally new technological processes and routes and introduced them into practice; these processes were used to synthesize A^4B^6 semiconductor materials and their solid solutions with record physical parameters at the international level.

In 2006, he was elected as the head of Laboratory for physics of solid-state structures. He held this position until 2011. Under his leadership, the laboratory's researchers developed some processes for preparing PbTe/CdTe thin films and multilayer structures, InSb semiconductor microwires, and bismuth-based semimetal microwires. The electrophysical, thermoelectric, and photoelectric parameters of these materials were studied with a view to using them as advanced elements in microdevices. Andrei Nicorici designed and prepared a PbMnTe:Ga compound exhibiting high light sensitivity at temperatures above 77 K and thereby opened up the possibility of developing a new type of photoconverters in the middle and far infrared spectral regions. A. Nicorici prepared some models of these photoconverters. His attention to detail during the design and construction of devices was clear, yet frequently subtle.

For more than 30 years, he had a close collaboration with Prof Dmitrii Khokhlov from the Moscow State University. He was one of the promoters of different bilateral projects with colleagues from Moscow. Andrei Nicorici was involved in many international and national projects concerning the development of different types of infrared and terahertz photodetectors. We were all very proud when Prof. Dmitrii Khokhlov delivering speeches at different conferences emphasized that the IR and terahertz photodetectors designed on the basis of PbTe and PbSnTe semiconductors had the highest sensitivity in the world. Several of these detectors are planned to be used in the near future in a new spatial missions for IR and terahertz monitoring of the extraterrestrial space.

Andrei Nicorici was a very enthusiastic person. In the last period, he was involved in the nanomaterials physics and development of a technology for the preparation of thin films of A^4B^4 compounds doped with group III elements and the preparation of nanostructured layers of A^4B^4 compounds. In addition, he was engaged in the high-temperature aerosol-assisted and liquid-phase synthesis of PbTe nanoparticles to obtain nanocomposites based on PbTe nanoparticles and in the study of their physical properties.

In addition, he gave a course of lectures in technology of semiconductor materials at the University of the Academy of Sciences of Moldova. He has published over 200 scientific papers in peer-reviewed journals in the country and abroad. Recently, one of the last collaborative papers with colleagues from Moscow concerning the magnetic-field-induced terahertz photogeneration in PbTe(Ga) has been published in JETP Letters (2016, vol. 104, pp. 64–67).

Doctor in physics and mathematics Andrei Nicorici will be remembered by his disciples and colleagues as a recognized highly skilled specialist in the field of physics and technology of semiconductor materials and a pleasant person to communicate with. In the person of talented researcher and teacher Andrei Nicorici we lost a friend, a colleague, and one of the important figures in our physics research community. Dr. Andrei Nicorici had two passions during his life—his laboratory and his family.

We express our sincere condolences and profound compassion for his family, relatives, and friends.

Academician Valeriu Kantser
Dr. Sofia Donu

CONTENTS

Bulk Materials

Condensed Matter Theory

Nanostructures and Nanomaterials

Technologies and Device Physics

Miscellaneous and General Physics

Events and Personalia